Mold-filling Simulation of Resin Transfer Molding with Fluid-Structure Interaction

Zur Erlangung des akademischen Grades eines
Doktors der Ingenieurwissenschaften (Dr.-Ing.)
von der KIT-Fakultät für Maschinenbau des
Karlsruher Instituts für Technologie (KIT)

angenommene
Dissertation
von

M.Sc. Julian Seuffert

Tag der mündlichen Prüfung:	19. Januar 2022
Hauptreferent:	Prof. Dr.-Ing. Frank Henning
Korreferent:	Prof. Dr. Anthony Straatman
Korreferentin:	Dr.-Ing. Luise Kärger

Vorwort

Die vorliegende Arbeit entstand im Rahmen meiner Tätigkeit als wissenschaftlicher Mitarbeiter am Institut für Fahrzeugsystemtechnik (FAST) des Karlsruher Instituts für Technologie (KIT).
Mein besonderer Dank gilt Prof. Dr.-Ing. Frank Henning für die Möglichkeit der Promotion, für die vertrauensvolle Zusammenarbeit sowie für die kontinuierliche Unterstützung während meiner Zeit am FAST.
Des Weiteren gilt mein besonderer Dank Dr.-Ing. Luise Kärger für die vielen fruchtbaren Diskussionen, die stets sehr guten und konstruktiven Anregungen zu den Publikationen.
Zudem bedanke ich mich bei Prof. Dr. Anthony Straatman für die Übernahme des Koreferats und für die wertvollen Anmerkungen zur vorliegenden Arbeit, sowie für die Unterstützung während meines Auslandsaufenthaltes an der Western University, Kanada. Im Rahmen dessen bedanke ich mich außerdem beim Karlsruhe House of Young Scientists (KHYS) für die Förderung des Auslandsaufenthaltes im Rahmen des Research Travel Grant.
Zusätzlich gilt mein Dank Prof. Dr.-Ing. Jürgen Fleischer für die Übernahme des Prüfungsvorsitzes.
Besonderer Dank geht auch an alle ehemaligen und aktiven Kollegen am FAST für die stets positive Zusammenarbeit, die spannenden Diskussionen und die gelebte Hilfsbereitschaft. Außderdem geht mein Dank an die Kollegen des Fraunhofer Instituts für Chemische Technologie (ICT), des Instituts für Angewandte Materialien (IAM) und des Instituts für Produktionstechnik (wbk) für

die Unterstützung bei der Durchführung der experimentellen Arbeiten. Besonders hervorheben möchte ich hier Dr. Markus Muth, Dr. Philipp Rosenberg, Felix Behnisch sowie Jonas Nieschlag.
Des Weiteren möchte ich den von mir betreuten Abschlussarbeitern und Hilfswissenschaftlern für ihr Engagement und die gute Zusammenarbeit danken.
Die Inhalte dieser Arbeit wurden großteils im Rahmen der Projekte „SMiLE“ und "MerVaërarbeitet sowie im Rahmen der Young Investigator Group (YIG) "Green Mobility". Für die finanzielle Unterstützung möchte ich mich beim Bundesministerium für Bildung und Forschung (BMBF), bei der Deutschen Forschungsgemeinschaft (DFG) sowie bei der Vector Stiftung bedanken.
Nicht zuletzt bedanke ich mich von ganzem Herzen bei Zarah, meiner Familie und meinen Freunden für den kompromisslosen Rückhalt und die große Unterstützung während der letzten Jahre.

Karlsruhe, im Februar 2022 *Julian Seuffert*

Abstract

Resin Transfer Molding (RTM) is a promising process for high-volume manufacturing of high-performance continuous fiber-reinforced plastics (CoFRP).
To increase the specific stiffness of the structural components, additional polymer foam cores can be embedded between the reinforcement fabrics. RTM enables an intrinsic production of these sandwich components that exhibit very high specific mechanical properties. During the mold-filling process step, a liquid polymer resin is injected into a closed mold and infiltrates the porous fabric. However, the pressure inside the mold rises due to the drag force of the fibers on the resin flow. This leads to a compression of the embedded foam core material. Moreover, the foam core compression leads to an increasing mold volume and thus to a higher part weight and a lower fiber volume fraction. As the resin flow strongly depends on the fiber volume fraction, this, furthermore, results in an altered mold-filling pattern. In this thesis, a numerical mold-filling simulation method is developed that enables to analyze the interdependence between resin flow and foam core deformation.
The developments in this thesis are based on a finite volume (FV) discretization combined with a volume-of-fluid (VoF) method for two-phase flow of the liquid resin and air that is implemented in the open-source library OpenFOAM®. Initially, a one-sided coupling is developed to model the influence of a forced tool deformation on the mold filling process, where the changing cavity is captured by using a dynamic mesh. With this first step, it is possible to simulate Compression Resin Transfer Molding (C-RTM) and Pressure-Controlled Resin Transfer Molding (PC-RTM), where the cavity height is not constant during mold-filling.

In the next step, a porous solid mechanics method is developed to model the fabric deformation during infiltration. The approach is based on Terzaghi's principle of effective stress and uses a large-strain incremental FV formulation. The coupling between resin flow, fabric compaction and foam core compression is modeled with a partitioned fluid-structure interaction (FSI) approach that is realized with the generalized open-source interface preCICE.
The simulation methods are verified at different stages and always show very good agreement to analytical solutions. A numerical sensitivity study on part-scale shows the strong influence of an embedded foam core on the mold-filling pressures and on the flow front evolution, which is not possible to predict with conventional mold-filling simulations. This confirms the necessity of using coupled simulations for mold-filling in RTM with embedded foam cores.
To validate the FSI method, sandwich parts are manufactured in RTM. Therefore, experimental measurements are conducted to characterize the materials involved in the validation. The mechanical characterization of the polymer foam core is carried out for different foam densities and at different isothermal temperatures. The results show a strong decrease of the compression modulus with decreasing density and increasing temperature.
The validation simulations show a good agreement with the predicted pressure level. With the validated model, it is possible to predict the mold-filling time and further parameters like e.g. the pressing force more accurately. A further increase in accuracy is expected when the temperature inside the mold is modeled with a more sophisticated model for heat transfer inside and between the involved materials.

Kurzfassung

Das Resin Transfer Molding (RTM) Verfahren ist ein vielversprechender Prozess für die Großserienfertigung von endlosfaserverstärkten Kunststoffen.
Um die spezifische Steifigkeit der Strukturbauteile zu erhöhen, können zusätzliche Polymerschaumkerne zwischen den Verstärkungslagen eingebettet werden. Das RTM-Verfahren ermöglicht die intrinsische Herstellung dieser Sandwichbauteile, die sehr hohe spezifische mechanische Eigenschaften aufweisen. Beim Prozessschritt der Formfüllung wird ein flüssiges Polymerharz in eine geschlossene Form injiziert und infiltriert das poröse Halbzeug. Der Druck im Inneren der Form steigt jedoch aufgrund der Widerstandskraft der Fasern gegenüber dem Harzfluss an. Dies führt zu einer Kompression des eingebetteten Schaumkerns. Die Kompression des Schaumkerns führt außerdem zu einer Vergrößerung des Kavitätvolumens und damit zu einem höheren Bauteilgewicht und einem geringeren Faservolumengehalt. Da der Harzfluss stark vom Faservolumengehalt abhängt, führt dies außerdem zu einem veränderten Formfüllungsverhalten. In dieser Arbeit wird eine numerische Methode für die Formfüllung entwickelt, die es ermöglicht, die Wechselbeziehung zwischen Harzfluss und Schaumkernverformung zu analysieren.
Die Entwicklungen in dieser Arbeit basieren auf einer Finite-Volumen (FV)-Diskretisierung in Kombination mit einer Volume-of-Fluid (VoF)-Methode für die Zweiphasenströmung bestehend aus flüssigem Harz und Luft, die in der Open-Source-Bibliothek OpenFOAM® implementiert ist. Zunächst wird eine einseitige Kopplung entwickelt, um den Einfluss einer vorgegebenen Werkzeugverformung auf den Formfüllprozess zu modellieren, wobei die sich verändernde Kavität mit einem dynamischen Netz erfasst wird. Mit diesem ersten Schritt

ist es möglich, Compression Resin Transfer Molding (C-RTM) und Pressure-Controlled Resin Transfer Molding (PC-RTM) zu simulieren, bei denen die Höhe der Kavität während der Formfüllung nicht konstant ist.
Im nächsten Schritt wird eine Methode zur Beschreibung der porösen Strukturmechanik entwickelt, um die Verformung des Halbzeugs während der Infiltration zu modellieren. Der Ansatz basiert auf dem Terzaghi-Prinzip der effektiven Spannung und verwendet eine inkrementelle FV-Formulierung für große Dehnungen. Die Kopplung zwischen Harzfluss, Halbzeugkompaktierung und Schaumkernkompression wird mit einem partitionierten Fluid-Struktur-Interaktions-Ansatz (FSI) modelliert, der mit der generalisierten Open-Source-Schnittstelle preCICE realisiert wird.
Die Simulationsmethoden werden in mehreren Schritten verifiziert und zeigen stets eine sehr gute Übereinstimmung mit analytischen Lösungen. Eine numerische Sensitivitätsstudie auf Bauteilskala zeigt den starken Einfluss eines eingebetteten Schaumkerns auf den Formfülldruck und auf die Ausbreitung der Fließfront, was mit herkömmlichen Formfüllsimulationen nicht vorhergesagt werden kann. Dies bestätigt die Notwendigkeit der Verwendung gekoppelter Simulationen für die Formfüllung bei RTM mit eingebetteten Schaumkernen.
Zur Validierung der FSI-Methode werden Sandwichbauteile im RTM-Verfahren hergestellt. Dazu werden experimentelle Messungen durchgeführt, um die an der Validierung beteiligten Materialien zu charakterisieren. Die mechanische Charakterisierung des Polymerschaumkerns wird für verschiedene Schaumdichten und bei unterschiedlichen isothermen Temperaturen durchgeführt. Die Ergebnisse zeigen eine starke Abnahme des Kompressionsmoduls mit abnehmender Dichte und steigender Temperatur.
Die Validierungssimulationen zeigen eine gute Übereinstimmung mit dem vorhergesagten Druckniveau. Mit dem validierten Modell ist es möglich, die Formfüllzeit und weitere Parameter wie z.B. die Pressenkraft genauer vorherzusagen. Eine weitere Steigerung der Genauigkeit wird erwartet, wenn die Temperatur innerhalb der Form mit einer erweiterten Methode für den Wärmeübergang innerhalb und zwischen den beteiligten Materialien modelliert wird.

Contents

Nomenclature

Acronyms

C-RTM	Compression Resin Transfer Molding
CFD	Computational fluid dynamics
CoFRP	Continuous fiber-reinforced plastics
CV	Control volume
D-SCM	Direct Sandwich Composite Molding
DSC	Differential scanning calorimeter
FE	Finite element
FRC	Fiber-reinforced composites
FRP	Fiber-reinforced plastics
FSI	Fluid-structure interaction
FV	Finite volume
FVF	Fiber volume fraction
GMRES	Generalized minimal residual
HP-IRTM	High-pressure Injection Resin Transfer Molding
HP-RTM	High-pressure Resin Transfer Molding
HPC	High performance computing
IQN-ILS	Interface quasi-Newton inverse least-squares
LCM	Liquid Composite Molding
NCF	Non-crimp fabric
PC-RTM	Pressure-Controlled Resin Transfer Molding
PET	Polyethylene terephthalate
PID	Proportional-integral-derivative

PISO	Pressure Implicit with Splitting of Operators
PMI	Polymethacrylimid
PUR	Polyurethane
PVC	Polyvinylchloride
RBF	Radial basis function
RIFT	resin infusion under flexible tooling
RTM	Resin Transfer Molding
SCL	Space conservation law
SCRIMP	Seemann Composites Resin Infusion Molding Process
T-RTM	Thermoplastic Resin Transfer Molding
UD	Unidirectional
VA-RTM	Vacuum-assisted Resin Transfer Molding
VARI	Vacuum-assisted resin infusion
VoF	Volume of fluid
WCM	Wet Compression Molding

Greek Symbols

α	Fluid fill factor	-
$\boldsymbol{\omega}$	Fiber orientation	-
$\dot{\gamma}$	Cure rate	s^{-1}
Γ	Cell face	-
γ	Cure degree	-
γ_g	Cure degree at point of gelation	-
μ	Dynamic fluid viscosity	Pa s
μ_{L}	First Lamé coefficient	Pa
μ_{Φ}	General diffusion coefficient	-
ν	Poisson's ratio	-
Ω	Cell volume	-
ϕ	Porosity	-
ψ	General scalar material property	-
ρ	Density	$\mathrm{kg\,m}^{-3}$

σ	Engineering stress	Pa
ε	Engineering strain	-
ε_{V}	Volumetric strain	-
φ	Fiber volume fraction	-

Latin Symbols

$[]_{\mathrm{u}}$	Updated configuration	-
$[]_f$	Value on the CV face	-
$[]_p$	Value on the CV centerpoint	-
$\dot{m}_f$	Fluid flux	$\mathrm{m^3\,s^{-1}}$
$\dot{V}_f$	Volumetric face flux	$\mathrm{m^3\,s^{-1}}$
λ_{L}	Second Lamé coefficient	Pa
$\tilde{\mathbf{u}}$	Volume averaged or Darcy velocity	$\mathrm{m\,s^{-1}}$
$\mathbf{C}$	Stiffness tensor	Pa
$\mathbf{d}$	Displacement	m
$\mathbf{E}$	Green-Lagrange strain	-
$\mathbf{F}$	Deformation gradient	-
$\mathbf{K}$	Permeability tensor	$\mathrm{m^2}$
$\mathbf{n}$	Unit normal vector	-
$\mathbf{Q}$	Momentum source term	$\mathrm{Pa\,m^{-1}}$
$\mathbf{Q}_{\mathrm{Darcy}}$	Darcy momentum source term	$\mathrm{Pa\,m^{-1}}$
$\mathbf{Q}_{\mathrm{dev},p}$	Deviatoric part of the source term	$\mathrm{Pa\,m^{-1}}$
$\mathbf{Q}_{\mathrm{hyd},p}$	Hydrostatic part of the source term	$\mathrm{Pa\,m^{-2}\,s}$
$\mathbf{R}$	Local to global coordinate system rotation tensor	-
$\mathbf{S}$	Second Piola-Kirchhoff stress	Pa
$\mathbf{u}$	Velocity	$\mathrm{m\,s^{-1}}$
$\mathbf{u}_s$	Cell surface velocity	$\mathrm{m\,s^{-1}}$
A	Gebart permeability model parameter	$\mathrm{m^2}$
a_n	Matrix neighbor coefficients	-
a_p	Matrix diagonal coefficients	-
B_1, B_2	Cure reaction rate model parameters	$\mathrm{s^{-1}}$

$B_{2,\Delta T_g}$	Cure reaction kinetics model parameter	s^{-1}
$B_{2,\text{diff}}$	Cure diffusion controlled reaction rate model parameter	s^{-1}
B_{eff}	Effective cure reaction rate model parameter	s^{-1}
E	Young's modulus	Pa
$E_\perp$	Young's modulus in transverse direction	Pa
E_V	Effective volumetric Young's modulus	Pa
G	Shear modulus	Pa
J	Jacobian	-
K_{11}	Highest in-plane permeability	m^2
K_{22}	Lowest in-plane permeability	m^2
K_{33}	Through-thickness permeability	m^2
$K_\perp$	Permeability transverse to fiber direction	m^2
$K_\parallel$	Permeability parallel to fiber direction	m^2
p	Total pressure	Pa
q_Φ	General volume source coefficient	-
R	Universal gas constant	$J\,mol^{-1}\,K^{-1}$
T	Temperature	K
T_g	Glass transition temperature	K
$T_{g,0}$	Glass transition temperature in uncured state	K
$T_{g,\infty}$	Glass transition temperature in fully cured state	K
V	Volume	m^3

1 Introduction

How to prevent global climate change is maybe the most relevant question of this and the next generation. This issue will influence all parts of the society and economy, from the energy and food sectors towards mobility concepts. The collective goal has to be to decrease CO_2 emissions as fast as possible to a level as low as possible. In 2018, the transport and mobility sector was responsible for approximately 25% of the global CO_2 emissions, and the far majority of 18% is caused by road-based mobility [1]. The automotive sector plays therefore an important role to reduce CO_2 emissions. One possibility to achieve this is given by the transition of combustion-driven cars to electric cars. Of course, this only has a significant impact, when the electric energy originates from CO_2-free sources. As long as this is not guaranteed, the reduction of energy consumption of cars or trucks should be minimized, regardless of their drive-train concept.
One option is to reduce the accelerated mass of the vehicle, which leads to less energy consumption and, thus, to fewer CO_2 emissions for combustion-driven cars, trucks, or airplanes. Furthermore, electric cars benefit from a lower weight by having an increased range.
To construct light but stiff and strong components, fiber-reinforced composites (FRC) with carbon fibers as reinforcement material are the most promising material class. They have outstanding weight-specific mechanical properties, which makes them the preferred material when lightweight is mandatory [2]. Unfortunately, part design of FRC is a challenging task. The advantage of the material, to be customizable to specific needs, is also its weakness because it means that a complex development and part design process is necessary to really benefit from the potential of the material. To maximize the weight-specific

stiffness of a part, the best way is to include the stiff fiber reinforcements only in the required areas of a component. For a high flexural stiffness this concept leads to a "sandwich" design. In a sandwich component, the continuous fibers are only placed in thin face sheets, whereas between them a very light material is embedded. This construction concept ensures that the fibers are located in highly stressed areas and are mainly afflicted by tension or compression loads.
The main reason that prevents the use of FRC and especially continuous fiber-reinforced plastics (CoFRP) in the automotive industry are the high part costs. In the aerospace industry, the maximum cost-per-weight ratio is higher than in the automotive industry and, thus, leads to a significant increase of CoFRP used in structural parts of airplanes. Especially during the last decade this amount constantly increased and resulted e.g. in the Boeing 787 consisting of more than 50% of composites by weight [3]. However, in the automotive industry, CoFRP still plays a minor role due to the strict limitation in part costs that are composed of the material costs and the manufacturing costs. Besides decreasing material costs, it is also important to reduce the manufacturing costs, especially for high-volume production [4]. Therefore, new manufacturing processes were developed, like Pressure-Controlled Resin Transfer Molding (PC-RTM) [5] or Wet Compression Molding (WCM) [6]. To maximize the benefit from these processes, it is crucial to gain more knowledge of what happens during the processing. This is especially relevant, as due to the strong influence of process parameters and material parameters on the processing behavior, also the resulting part quality depends heavily on the chosen parameters. As a compromised part quality leads to more waste and consequently to higher costs, this is one further reason to optimize the manufacturing of CoFRP.

1.1 Motivation

To manufacture CoFRP parts, one possible option is to use manufacturing processes referred to as Resin Transfer Molding (RTM) that are characterized by

injecting a liquid resin into a closed mold containing a reinforcement fabric. This process has the advantage of a high automation potential and is, therefore, well-suited for automotive applications that require medium to high volume manufacturing. To utilize this advantage, it is necessary to understand the dependence of the process performance from the process and material parameters in detail.

By means of numerical process simulations, these dependencies can be analyzed. This holds true not only for RTM but in general for the manufacturing of CoFRP. With the help of numerical simulations, the process behavior is predicted and actions to improve the manufacturing process are taken, which can be for example the reduction of fiber waste or a decrease of the processing time. With these goals, process simulations are already frequently used [6, 7]. By combining several process simulation steps, a virtual process chain is generated that enables not only to optimize individual process steps but additionally to optimize the process in a holistic approach (Fig. 1.1).

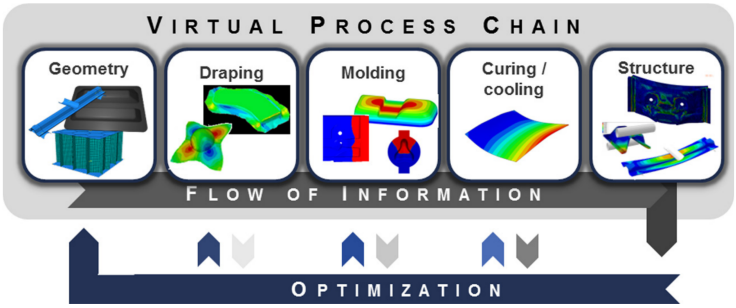

Figure 1.1: Virtual process chain for CoFRP consisting of design, process simulations, and structural mechanics [7]

In the RTM process, the reinforcement fibers and the liquid polymer resin are brought together during the mold-filling step, where the final part shape is created. The mold-filling simulations are, thus, one important part of the virtual RTM process chain. They are used to predict the occurrence of incomplete

infiltration or porosity, which would result in poor mechanical properties [8, 9]. Furthermore, the mold-filling simulations are used to predict the mold-filling time [10, 11] and can be used for process optimization [12]. One may argue that curing time is significantly higher than mold-filling time, but even if this is the case, a long mold-filling time has to be avoided because of the requirement of a low viscosity during the whole infiltration, which often prevents the use of fast-curing resin systems [13, 14].

The mold-filling in the RTM process is characterized by a complex flow-front advancement that can exhibit high cavity pressures, strong anisotropy with locally changing predominant directions, local runners, and high sensitivity to the reinforcement material parameters. Furthermore, new advanced RTM processes like PC-RTM use a non-constant cavity during the mold-filling, which leads to time-varying processing conditions [5].

To simulate the mold-filling in RTM processes that exhibit a non-constant cavity, the development of new simulation methods is necessary. The future use should not be prevented to only one specific RTM process type, but instead, it has to be the goal to develop a flexible simulation method that can be adjusted to newly developed and even to future RTM process variants.

The RTM process allows producing sandwich parts in only one process step without the need for later bonding of the fiber reinforcements and core material. Figure 1.2 shows a cut of a manufactured RTM sandwich part, where the carbon fiber top and bottom sheets are visible as black layers and the embedded foam core in between them is shown in white.

However, the manufacturing process is even more complex for CoFRP sandwich components, compared to monolithic parts. During the mold-filling process step, high pressures inside the RTM mold lead to deformed, shifted, or completely crushed core materials and to non-infiltrated areas [15]. These effects are known from experimental investigations, though not fully understood yet. Furthermore, the deformation of the embedded foam core strongly influences the infiltration and, thus, the processing behavior and the part quality [16, 17]. It is not possible to predict the RTM mold-filling of sandwich CoFRP using

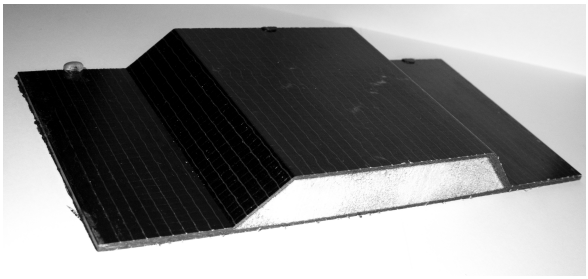

Figure 1.2: Manufactured RTM sandwich part; the cut shows the top and bottom sheet and the embedded polymer foam core

state-of-the-art simulation methods but instead, the development of new numerical simulation methods is necessary. Again, it is important that a mold-filling simulation method for sandwich parts is not only limited to this specific application but is a further development of the method involving non-constant cavities for PC-RTM.

1.2 Thesis Aim

The main goal of this thesis is to develop and validate a numerical method to simulate RTM mold-filling with embedded polymer foam cores. The developed method should be able to predict the infiltration quality as well as the deformation of the embedded foam core during mold-filling. To capture both, the resin flow and the foam core mechanics, a fluid-structure interaction (FSI) method is necessary to describe the coupled behavior.
The simulation method has to include several major parts: The resin flow inside the reinforcement material under varying conditions, the foam core deformation during the mold-filling, and suitable boundaries and models for processing conditions and material properties. The simulation models themselves should be

applicable to part-scale simulations while maintaining a reasonable numerical effort.
Several steps are necessary to achieve this. First, a numerical method to simulate mold-filling in a flexible cavity has to be developed. The second step is the development of a numerical method to model the porous solid mechanics of the fabric during the mold-filling. Based on these two methods, an FSI method is used to numerically couple the mold-filling and the porous fabric deformation with the embedded foam core.
The method development is furthermore carried out in a general approach to also enable simulating the mold-filling of several kinds of manufacturing processes that involve non-constant cavities, such as PC-RTM or Direct Sandwich Composite Molding (D-SCM) [18].
Finally, a validation of the developed method aims to show the possibility to realistically predict the mold-filling on part-scale with the newly developed method.

1.3 Thesis Outline

With the aim to give a more specific overview of the state-of-the-art of the involved subjects, related research is reviewed in each of the following chapters matching their respective content.
Chapter 2 follows after this introductory chapter with a presentation of the RTM process as well as details about the materials and relevant process variants.
Subsequently, Chapter 3 focuses on the mold-filling simulation method used in this work. The method concentrates on the resin flow inside a porous medium that is placed in a non-constant cavity. At this point, advanced RTM process variants like PC-RTM can be modeled. The chapter finishes with a verification of the mold-filling simulation method.
After the development of the simulation method for the resin flow, the solid mechanics' simulation method for the involved porous fabric is developed and

its coupling to mold-filling is presented in Chapter 4. Furthermore, the involved FSI method for coupling mold-filling and foam core deformation is developed in this chapter. Several verification examples are given to prove the correct behavior of the methods.

After the two chapters about the numerical methods that result in the FSI framework for RTM mold-filling simulations for sandwich parts, the material properties of the resin systems, the fabrics and the foam core material are characterized in Chapter 5. The characterization and material modeling are carried out regarding fabric permeability, fabric compaction as well as foam core deformation under compression loads.

Based on the numerical methods developed and with the characterized materials follows Chapter 6, in which two application examples and one experimental validation are presented. First, the developed simulation method is applied to two new processes. One application example is given for PC-RTM, which is a newly developed process using an active pressure control by changing the cavity height during mold-filling [5]. The second example shows the application to D-SCM, which is a process that uses the pressure of expanding foam material to infiltrate the face sheets of a sandwich [18]. Furthermore, a validation of the RTM mold-filling simulations for sandwich parts is carried out by comparing simulation results to experimental RTM trials.

Finally, Chapter 7 concludes the findings of this thesis and Chapter 8 gives an outlook on possible future research.

2 RTM Processes and Materials

FRC generally consist of matrix material and dispersed fibers as reinforcing material. The matrix is used to give the part its shape, to distribute the forces between the fibers, and to protect the fibers against the environment, whereas the fibers increase the stiffness and strength of the part. Nowadays, FRC is found in nearly every application domain from skyscrapers to ships or satellites. The major advantage is that their properties can be tailored to the application, which leads to large flexibility of their use [2]. On the other hand, the adjustment to the application needs special know-how of the material properties, the load case, and also processing technology.

As a sub-group of FRC, in fiber-reinforced plastics (FRP) the matrix material is made of thermoset or thermoplastic polymers. Polymers have the advantage of low cost and comparable low density while the relatively low stiffness allows a good distribution of the loads between the fibers. Furthermore, a developer can choose between many polymers to find the best one fitting the product requirements. Because of the vast number of materials and material variants used in FRP, no extensive review is given in this thesis, but instead, the focus lies on the process and materials that are considered and investigated here. For a more detailed review, the reader is referred to books and articles that give a good overview of FRC and FRP, their manufacturing processes, and their applications [6, 19–22].

RTM is a manufacturing process to produce CoFRP. It is well-suited to produce thin, shell-like structures, although the thickness can be up to several

centimeters e.g. in wind energy applications. The process is part of the Liquid Composite Molding (LCM) process family [23] that is defined by a liquid resin that infiltrates a reinforcement inside a mold that has the shape of the part. In the case of CoFRP, the dry fibers are placed beforehand into the mold, where they are infiltrated by the resin. In RTM, the materials involved are a liquid thermoset resin system and a textile fabric made of reinforcement fibers, although recently also thermoplastic RTM (T-RTM) is investigated as a potential alternative [24, 25]. The fabric can be made of any technical fiber type. However, glass fibers and carbon fibers play the most important role in applications.
Based on the basic RTM manufacturing principle, various process types exist that will be introduced in the next section. Furthermore, a short overview of the used matrix materials, the fiber reinforcements, and the core materials is given in the following sections.

2.1 RTM process types

The RTM process consists of several subsequent steps that are schematically shown in Fig. 2.1. The first process step is to cut the fabric into patches close to the final part dimensions.
Secondly, a stack of several cut patches is built to form the desired layup. The layup is aimed to be symmetrical to the mid-plane to avoid distortions or residual stresses in the final component. The main fiber orientations of the fabrics can be chosen to suit the load case of the structure. By allowing anisotropic layups and changing thicknesses in different parts of the component, it is possible to tailor the performance of the component to specific mechanical requirements, which is one of the main benefits when using FRP [2].
For complex shapes, the layup is then transferred to a draping tool, where a three-dimensional preform that is close to the final part dimensions is formed. This preforming step is needed to avoid high shearing angles, wrinkles, and fiber gaps inside the part, which negatively affects the infusion process and

the mechanical performance. Preforming (or draping) is a complicated process step that requires special methods to minimize the negative effects, like e.g. flexible gripping mechanisms. Furthermore, special methods are necessary to correctly predict the draping behavior by numerical simulations [6].
In the following step, this preform is transferred to a heated RTM tool that consists of an upper and a lower part that forms the mold (or cavity). After closing the tool, the liquid resin is injected. When flowing inside the mold, the resin infiltrates the fabric. During infiltration, hydrostatic pressure is built inside the mold due to the drag force of the fibers against the resin.
After injection, the thermoset resin cures inside the closed and heated mold to give the part the necessary stability. Finally, the part is demolded and finishing process steps like trimming or hole drilling follow.

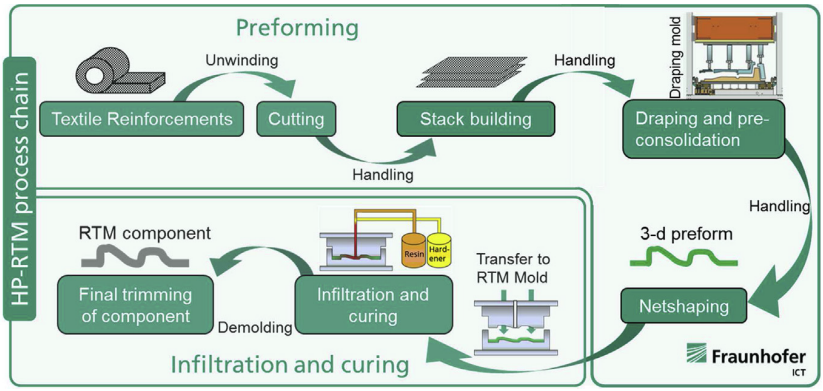

Figure 2.1: RTM process steps: from textile to final part showing the proces ssteps of cutting and stacking, draping, mold-filling, curing and demolding [6]

When a high flexural stiffness against bending is desired, a light core material is embedded between two layers of FRP to build a so-called "sandwich". To manufacture sandwich parts using RTM, two fabric stacks have to be created, namely the top and bottom sheets. They can be preformed separately before a common stack with the bottom sheet, the core material, and the top sheet is

created. This sandwich-preform is then transferred to the RTM mold, where the normal process route of RTM is continued that consists of injection, curing, and demolding of the part. The process route is visualized schematically in Fig. 2.2.

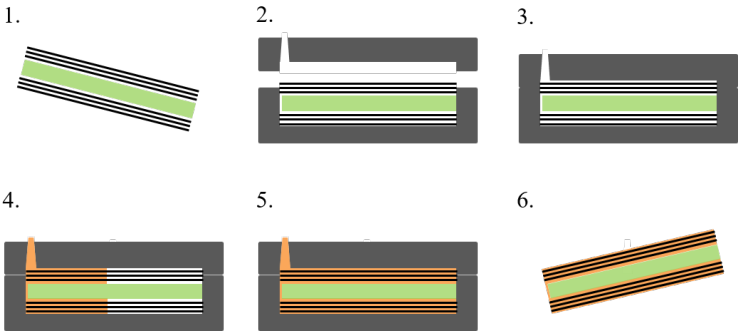

Figure 2.2: RTM process to manufacture sandwich parts with 6 steps; (1) Stacking of the preform; (2) Transfer to open mold; (3) Closing mold (and applying vacuum); (4) Injection; (5) Curing; (6) Demolding

This process has the advantage of in-situ curing and bonding of the top and bottom layers onto the core and, thus, reduces the process steps compared to a regular process route with infiltration, surface treatment, and bonding of the sheets onto the core material. Furthermore, also complex shapes can be manufactured in one RTM tool, whereas two tools are needed when the top and bottom layers are manufactured separately. On the other hand, this process route only allows using non-infiltrating core materials like closed-cell polymer foams, which limits the possible product variants.

A large number of RTM processing types were invented mainly with the goal to decrease production time. There is no naming convention that is used in research or industry, which leads to a difficult distinction of the processes described in the literature. A short overview of the most common variants is given here, focusing on the process types investigated in this thesis.

The standard (low pressure) RTM process uses resin injection pressures up to 20 bar [26]. Obviously, the industry tried to decrease the injection time by increasing the injection flow rate leading to high pressures as high as 100 bar or even more. Stiff, rigid steel molds and special high-pressure injection equipment characterize this process, which is commonly called high-pressure RTM (HP-RTM) or sometimes high-pressure injection RTM (HP-IRTM) [27].
Another idea to decrease injection time, especially for larger parts, is to shorten the flow path of the resin as a long flow path leads to longer mold-filling times or high pressures. The shortest possible flow path in an RTM mold is infiltration in the thickness direction, which led to the family of Compression-RTM (C-RTM) process types [28]. In C-RTM, a small gap above the preform is held open during the injection of the resin that fills this gap at very low pressure. After injection, the gap is closed so that the resin infiltrates the preform mostly in the thickness direction [29].
To lower the cavity pressure but also allow for very fast process times, the Ultra-RTM and PC-RTM process types were developed [5, 30, 31]. PC-RTM continues the investigations made of the Ultra-RTM process variant, where the pressure is controlled during the compression step [30]. In PC-RTM the pressure control is used throughout the injection, and additionally during the compression and the curing step. Figure 2.3 shows the eight process steps of PC-RTM. First, the layup is stacked with several fibrous layers with predefined fiber orientations. Secondly, the preform is put inside the open mold. Afterward, the mold is closed but instead of completely closing the mold to the final part thickness, a small mold gap is left open (step three). At this moment, also vacuum can be applied to the cavity to avoid dry spots in the component. In step four, the injection starts while the mold gap height is held constant. The fifth step starts when the predefined pressure control value is reached. The mold gap is actively increased, whereby the mold opening velocity is controlled by the hydraulic press. The mold opening velocity depends on the cavity pressure that is measured by an integrated sensor, which is located close to the inlet but can also be at any other location inside the cavity. The injection flow rate is

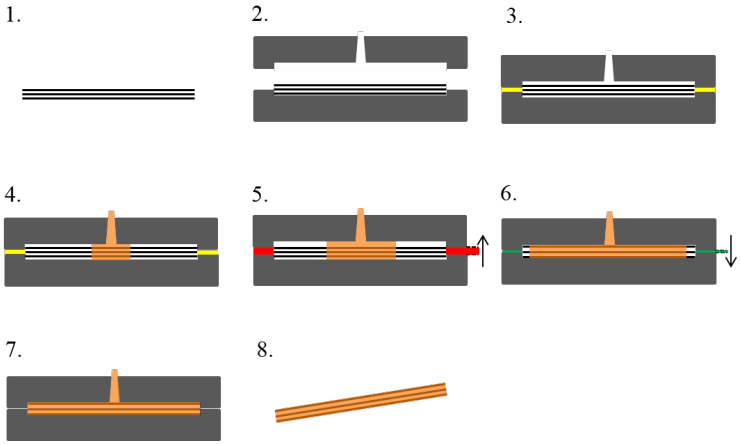

Figure 2.3: PC-RTM with 8 process steps; (1) Stacking of the preform; (2) Transfer to open mold; (3) Closing mold to initial gap height (and applying vacuum); (4) Injection with constant mold gap height; (5) Injection with opening mold and constant cavity pressure; (6) Compression with constant cavity pressure; (7) Curing; (8) Demolding [32]

kept at a constant value during the whole injection. When the desired amount of resin is injected, the inlet gate closes, and step six starts. In this step, the part is compressed to its final thickness while keeping the pressure constant at the same pressure value as before. Subsequently, the part is cured inside the mold while maintaining a clamping pressure, and finally, it is demolded.

The mold-filling takes place during steps four to six. The course of pressure and mold gap height in these steps are shown in Fig. 2.4. Further on, these three steps are referred to as Stages 1, 2, and 3. Figure 2.4 visualizes the increasing pressure in Stage 1, as well as the active pressure control in Stages 2 and 3 that is achieved by actively opening (Stage 2) and closing (Stage 3) the mold.

When realizing PC-RTM, besides the process temperature and the injection flow rate, only two important process parameters have to be set: the pressure-control value and the initial mold gap height. The pressure control value determines the maximum mold gap height, the mold-filling time, and the clamping force

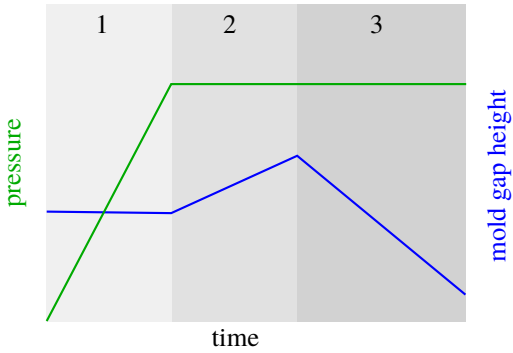

Figure 2.4: Schematic representation of cavity pressure and gap height of the three mold filling stages of PC-RTM (cf. steps 4 to 6 in Fig. 2.3) [32].

needed. By changing the initial gap height, the pressure increase rate during the injection step can be adjusted. When choosing a very low value, the pressure rises very fast in the first seconds, equal to HP-RTM. A fast increasing pressure is more difficult to control, as the mold gap has to be adjusted in a very short time. Hence, a small initial mold gap is needed for a robust process. The maximum mold gap height is thereby limited by the design of the mold sealing system. Furthermore, a very large initial mold gap height can lead to higher mold filling times because of the lower resin filling degree at the end of the injection which consequently leads to longer compression times. The pressure control is only realized by the mold opening and closing controlled by the hydraulic press. For high pressure values, a low mold gap height at the end of the injection and also a fast compression and, therefore, a low mold filling time is expected.

With the idea to have a more flexible and less expensive tool for the production of smaller batch sizes, several RTM types were developed to bridge the gap to vacuum-assisted resin infusion (VARI). In VARI, only a lower mold part exists. The fabric is placed on the lower mold and is sealed with a vacuum bag on the upper side. The resin is held at atmospheric pressure and infiltrates the preform

by applying a vacuum to the mold [33]. Several names for these processes are used in literature and industry: vacuum-assisted RTM (VA-RTM), Seemann Composites Resin Infusion Molding Process (SCRIMP^{TM}) or resin infusion under flexible tooling (RIFT) [34]. In the gap between the single-sided mold processes and RTM, it is also possible to use one rigid lower mold part and one more flexible upper mold part that is e.g. made of a plastic or composite material. This process type is often referred to as Light-RTM (L-RTM) [35].
Furthermore, the WCM process family exists, which is also used to manufacture CoFRP. WCM is characterized by a surface application of the resin onto the fabric when the mold is still open and a subsequent closing and compression, which leads to a combination of forming and infiltration at the same time [6, 36]. This process allows very fast cycle times, because, like in C-RTM, the main infiltration direction is in open gaps above the preform and in the thickness direction. Because of the promising properties, the modeling of combined fluid propagation and forming in WCM is recently also in the focus of research [37, 38].

2.2 Matrix materials

The choice of the matrix material used in RTM depends on the required mechanical properties of the cured part that have to be high enough to meet the performance demands of the product [39]. Thermoset matrices are most frequently used, whereas thermoplastic matrices play a minor role [25]. Of the thermoset matrices, the most important high-performance systems are epoxy-based resins besides unsaturated polyesters or polyurethanes. Epoxy resins are often the preferred matrix systems because of their robustness, low chemical shrinkage, and their adjustable curing behavior by using a certain curing agent. In the aerospace industry, only qualified resin systems can be used, and because certification is costly, still slow curing epoxy resin systems are state-of-the-art, like e.g. the RTM6 system by Hexcel® [40].

In the automotive industry, certification is not needed and the manufacturing focus lies more on high-volume manufacturing as well as short cycle-times and, thus, fast-curing non-epoxy resin systems are of interest. Especially for fast-curing systems, it is important to know the resin viscosity and the curing behavior during processing. On the one hand, the viscosity should be low to allow for good impregnation and low cavity pressures. On the other hand, the curing time should be as low as possible to minimize cycle-times, which however results in a rapid increase in viscosity. These opposed criteria requests to predict mold-filling times accurately, to guarantee a filled mold before curing while maintaining a minimum time between the end of mold-filling and reaching the gelation point. Therefore, special fast curing resin systems were recently developed for the automotive industry [41]. Furthermore, accurate curing models are necessary to optimize the combined mold-filling and curing correctly [42, 43].

2.3 Fiber reinforcements

The most important fiber reinforcement materials used in RTM are carbon fibers and glass fibers. However, it is possible to use many different technical fiber types in RTM, as long as they have good bonding to the matrix and fit to processing conditions. Carbon fibers have the highest specific mechanical properties, but they are also very expensive. Therefore, they are used mainly in aerospace applications or in sports cars and race cars, where lightweight is of prime importance. The main advantage of glass fibers is their low cost, which makes them the most used fiber type in the automotive industry. To optimize the part costs and mechanical performance, also a combination of glass fibers and local carbon fiber patches can be used in one RTM part [44].
The use of natural fibers like jute, sisal, or flax is increasing but still at a low level compared to technical fibers. A comprehensive review about natural fibers in RTM is given e.g. by Mittal et al. [45]. One of the drawbacks of natural

fibers is their higher variability of mechanical properties [46], though Torres et al. [47] reported variability in the same order of magnitude as for carbon fibers but at a significantly lower level.
Besides the fiber type, also the type of fabric influences the processing and mechanical properties. Individual fibers are normally combined to form a roving (or bundle), which is then used to create fabric materials. Unidirectional (UD) non-crimp fabrics (NCF) consist of several rovings parallel to each other that are stitched together to form a two-dimensional fabric. Furthermore, several stacks of UD-NCF in multiple directions can be stitched together to form e.g. biaxial or triaxial NCF fabrics, when a more isotropic mechanical behavior is desired.
The second important fabric types besides NCF are woven fabrics. Normal-oriented rovings are woven together with a specific weave pattern like plain weave, twill weave, or satin weave. The weaving of the rovings leads to an undulation of each of the rovings, which on the one hand decreases the resistance against infiltration and facilitates draping, but on the other hand, also leads to decreased mechanical performance [48].

2.4 Sandwich core materials

Sandwich parts are defined by embedding a significantly lighter core material between thin but very stiff outer layers. This leads to a strong increase in flexural stiffness by transferring the stiff layers further away from the neutral bending line. This principle is the main motivation for manufacturing sandwich parts. Further advantages of sandwich parts are the good thermal insulation and acoustic damping that can be achieved [49].
Two types of sandwich core materials are distinguished: Structured, and homogeneous cores [50]. Structured cores are e.g. honeycombs or corrugated cores, where the lightweight in the core part is generated by geometrical structures.

Especially honeycombs exhibit very good specific mechanical performance because of their low density [51]. However, because of their open cells, processing in RTM is not possible.

Homogeneous cores can have an impermeable surface, which allows using them in LCM processes. Early sandwich components were manufactured with a face material made of an FRP (mainly glass fiber) and with a balsa wood core [52]. Nowadays, wood-based core materials are mostly replaced by light polymer foams. Many polymers are suited for expansion to a foam material like e.g. polymethacrylimid (PMI), polyvinylchloride (PVC), polyurethane (PUR), or polyethylene terephthalate (PET).

PMI foams are already used in sandwich components, e.g. in the aerospace industry [53]. They provide very good mechanical properties and low densities but at comparable high costs. PVC foams have a lower pressure resistance than PMI foams [54, 55] but also at a lower cost. PUR foams were also already used in RTM [56, 57] for automotive applications because of their very low cost compared to PMI foams, and the possibility to directly manufacture three-dimensional geometries. PET foams have the lowest cost but also comparatively low mechanical properties [58]. They are manufactured by a continuous extrusion of liquid PET mixed with a blowing agent. After mixing under high pressure inside a nozzle, the foam expands as far as 50 times its volume, and thus densities lower than $100\,\mathrm{g\,L^{-1}}$ can be reached. One further advantage is that the density and strength of the foam core material can be adjusted with the expansion factor and, thus, an optimization for specific manufacturing processes or load cases is possible. After the extrusion of rectangular foam blocks, these are welded together to form large foam plates. Subsequently, the three-dimensional core geometry for a sandwich component is cut out of those plates.

The most obvious method to manufacture sandwich parts is to produce the sheet layers separately and bond them to the core material in a subsequent process step. However, this results in several process steps and thus may not always be the best option for high-volume applications and complex shaped parts. As was introduced before (cf. Fig. 2.2), one possibility to avoid this disadvantage

is to manufacture the sandwich part in one process step using RTM. Major requirements regarding the foam material, are the resistance of the foam against plastic deformation and against resin saturation during the injection stage. For this reason strong but light core materials with a closed surface are required that are also more expensive and, thus, still prevent this intrinsic sandwich manufacturing from gaining high industrial interest. Gerstenkorn showed that in combination with a PC-RTM process, also a light PUR foam material is suited to be used in RTM sandwich manufacturing [17] when the process parameters like temperature and pressure are adjusted according to the foam core density. For successful production of sandwich parts in RTM, it is, therefore, crucial to correctly predict the processing behavior by numerical simulations and to accurately adjust the process parameters to the materials involved.

3 Mold-filling Simulation Method for RTM with non-constant Cavities

The mold-filling step in RTM is the key process step, where fibers and resin are "married" to form a composite material. The mold-filling step affects the part quality as well as the process cycle time. With the main goal to achieve a robust and economically efficient process, two main issues are always in the center of optimizations. First, an incomplete mold-filling has to be avoided, and secondly, mold-filling and thus process cycle time should be minimized. As an experimental investigation of several geometries, materials, and process parameters can lead to a vast amount of experiments, numerical simulations are beneficial for a prediction of the mold-filling during the development process of a new component. Mold-filling simulations of RTM are already frequently used to optimize injection strategies and injection velocities or to analyze the infiltration behavior of complex parts [9, 12, 59–62].

The fundamentals of mold-filling simulation and the approach developed in this work are described in the first sections of this chapter. The approach focuses on RTM mold-filling simulation involving non-constant cavities. Therefore, a method to model mold-filling inside a dynamicly changing computational mesh is developed. Furthermore, Section 3.3 focuses on the material parameters of the fabric and the resin, respectively. The mold-filling method is then verified for PC-RTM (Section 3.5). Finally, the method is reviewed and discussed in Section 3.6.

3.1 Introduction and review of related work

During mold-filling, the liquid resin infiltrates the dry fabric starting from an inlet gate, where a constant pressure or a constant mass flow rate is set. At least one outlet gate is needed to let the air flow out of the cavity. The outlet has to be at the location, where the resin arrives the last, to prevent the formation of dry spots. If vacuum is applied before the infiltration, no outlet is needed, but normally a small resin overflow at the edges is allowed to make sure that the whole preform gets impregnated. A very good introduction to flow phenomena in composites manufacturing and especially to RTM mold-filling can be found in the book "Flow and rheology in polymer composites manufacturing" [63].
For an introduction to mold-filling, it is helpful to have a look at the different scales of the fibrous preform. Figure 3.1 shows a schematic overview of the three different scales present in RTM mold-filling.
The smallest scale of interest here is the micro-scale, which implies the flow around individual or multiple filaments inside a roving. On this scale, it is obvious that the numerous filaments form obstacles for the resin flow. Two more trivial but important observations can be made at micro-scale: More fibers in a certain volume lead to narrower gaps and thus to a larger resistance on the resin flow; Parallel to the filaments, the flow is eased compared to a flow perpendicular to the filaments. It should be noted that on micro-scale, the filaments and the fluid can still be treated as continua, where the continuum mechanic equations are valid. On meso-scale, several thousand fibers form one roving. To be able to simulate the resin flow, the fibers are homogenized to a porous medium, whereas the flow between the rovings is still captured as a free flow. This scale distinguishes CoFRP from other types of porous media, like soils or granular materials that only consist of micro-scale and macro-scale.
On the macro-scale, which is generally used when simulating mold-filling of RTM components, the individual fibers and the rovings are homogenized to one porous medium. The multi-scale behavior of the mold-filling complicates

the homogenization and is one of the main reasons for the difficult prediction of the flow during RTM mold-filling.

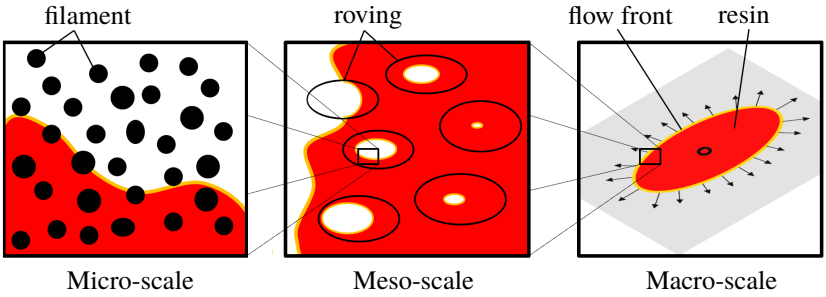

Figure 3.1: Multi-scale flow behavior during mold-filling in RTM consisting of micro-scale, meso-scale, and macro-scale [6]

The focus of this work is on macro-scale simulation using the theory of homogenized porous media. The review of literature given in this section is thus confined to macro-scale approaches. An overview of multi-scale methods not only for flow in porous media but also for heat transfer and solid mechanics is e.g. given by Ngo [64].

In soil mechanics and hydrogeology, the models of e.g. porous water flow inside sands or the groundwater flow inside soils are based on Darcy's law [65]. This law is also used to describe the RTM mold-filling on a macro-scale, where the porous medium assumption is used. Darcy's law is often stated in the form

$$\tilde{\mathbf{u}} = -\frac{\mathbf{K}}{\mu} \cdot \nabla p\,, \tag{3.1}$$

where $\tilde{\mathbf{u}} = (1 - \varphi) \cdot \mathbf{u}$ is the volume averaged velocity with the fiber volume fraction (FVF) φ and the resin velocity $\mathbf{u}$. ∇p is the pressure gradient in the cavity, μ is the dynamic resin viscosity and $\mathbf{K}$ is the permeability of the fabric. Darcy first determined the relation experimentally, only more than a century later it was shown to be a special solution of the Navier-Stokes equations [66].

Many different numerical models to solve the Darcy equation for RTM mold-filling have been developed and analyzed [67–69]. The finite element/control volume (FE/CV) approach with non-conforming finite elements [11, 69] is nowadays established as a standard for commercial software for RTM mold-filling simulations. It uses the Darcy equation and solves the pressure-velocity relationship at computational nodes using a control volume defined by the element centroids and mid sides. The Darcy equation is solved only in the infiltrated part of the geometry, defined by a fill factor $\alpha, 0 \leq \alpha \leq 1$. At the flow front, the pressure is fixed to be equal to the outlet pressure. After the calculation of the pressure field, the flow front is advanced using the calculated velocity and updating the fill factors. During this step, some elements can achieve a fill factor > 1, which has to be corrected in a subsequent step [69].
Mold-filling simulations of C-RTM were first established by Pham et al. [70, 71], who modeled one-dimensional and two-dimensional resin flow based on Darcy's law using the same FE/CV approach. Shojaei [72] developed a three-dimensional FE/CV method to simulate the resin flow of a C-RTM process in thick components, where a through-thickness impregnation cannot be neglected. Furthermore, Simacek et al. [73] simulated C-RTM also using a three-dimensional FE/CV method focusing on the implementation of an open gap between the fibrous preform and the mold, which is assumed to occur for wide mold openings. The gap is modeled by adding two-dimensional elements on top of the preform mesh. As they only solve the Darcy equation and not the Navier-Stokes equations, they have to set an effective permeability inside the gap, which is obtained by using the lubrication theory of a Stokes-flow in a narrow channel.
In contrast to the FE-based methods developed only for mold-filling stands a second approach, which is the simulation using a finite volume (FV) discretization implemented in computational fluid dynamics (CFD) simulation software. In this case, the Navier-Stokes equations are solved and the Darcy-flow inside the porous medium is computed by adding a momentum sink term in the governing equations. Here, both fluid phases (air and resin) can be modeled by a

"Volume of Fluid" (VoF) method [74], which uses a phase fraction equation and thus allows to later track the resin front in the mold-filling simulation. Further information on this method is found in the next section. Nearly every CFD software supports porous media though its implementation is limited to e.g. isotropic permeability, constant permeability in fixed domains, single-phase flows, or stationary simulations.

Magagnato et al. [75] developed an FV-based method to simulate mold-filling of RTM by modeling a two-phase flow through porous media considering local anisotropic permeability. The permeability tensor is evaluated at each cell using local fiber orientation and fiber volume fraction. This allows e.g. the use of mapped fiber orientation data from draping simulations or from CT-Scans [9]. Additionally, a compressible formulation of the air phase was implemented to predict the development, movement, and dispersion of air bubbles [76], which is not possible with finite-element-based commercial RTM mold-filling simulation software.

Seuffert et al. [77] developed a method to simulate C-RTM based on a three-dimensional FV discretization and using a deformable mesh to describe the current cavity thickness. By implementing a virtual controller to set the cavity thickness, it is also possible to simulate PC-RTM [78]. A further comparison of the PC-RTM simulations to experiments by the authors shows a good agreement in the predicted pressure and gap height characteristics [32].

C-RTM and PC-RTM have in common that the mold cavity height changes during the mold-filling. This leads to a non-constant geometry as well as varying FVF and consequently non-constant material parameters. The method used in this work to simulate the mold-filling in these non-constant cavities is explained in detail in the next section.

3.2 Numerical modeling for non-constant cavities

The simulation method presented in this thesis is based on the Navier-Stokes equations. In order to make the method as easy as possible, some flow assumptions are made in the equations for RTM mold-filling that are summarized here:

- Air and resin are immiscible phases.
- The fluids are assumed to be Newtonian. The air is assumed to be compressible, the resin to be incompressible. Resin viscosity changes only with temperature and time due to the specific thermoset resin properties and the curing reaction starting during mold-filling.
- The fibers are assumed to be incompressible and stationary. There is no in-plane movement of the fibers (no fiber-washing or fiber deformation) and during C-RTM, the velocity of the fibers in the thickness direction is not influencing the in-plane resin flow.
- Inertia of the resin flow inside the porous medium is negligible. All inertial forces are very small compared to the porous drag; the Reynolds number is very small (creeping flow): $Re < 1$.

With these assumptions, the fluid dynamics of the resin (and the air) inside the cavity can be modeled as a flow of compressible viscous fluids that is captured by the continuity equations of mass, momentum, and energy.

3.2.1 Governing equations

The resin flow inside the porous medium can be described using the continuity equations in an Eulerian framework. Starting with the mass continuity equation for a compressible fluid that is given as:

$$\frac{\partial \rho}{\partial t} + \nabla \cdot (\rho \, \mathbf{u}) = 0 \,, \tag{3.2}$$

and the conservation form of the momentum continuity equation for a Newtonian fluid:

$$\frac{\partial}{\partial t}(\rho\,\mathbf{u}) + \nabla\cdot(\rho\,\mathbf{u}\otimes\mathbf{u}) = -\nabla p + \mu\,\nabla^2\mathbf{u} + \tfrac{1}{3}\mu\,\nabla(\nabla\cdot\mathbf{u}) + \mathbf{Q}\,, \tag{3.3}$$

where $\otimes$ is the outer product and with the velocity $\mathbf{u}$, the density ρ, the pressure p, the dynamic viscosity μ, and a source term $\mathbf{Q}$. The source term is now used to add a porous drag term that accounts for the influence of fibers onto fluid flow. Therefore, the Darcy equation (3.1) is rewritten to:

$$\mathbf{Q}_{\text{Darcy}} = \nabla p_{\text{Darcy}} = -\mu\mathbf{K}^{-1}\,(1-\varphi)\,\mathbf{u}\,, \tag{3.4}$$

which is the form implemented in Eq. (3.3). The porous drag acts like an additional momentum sink, which increases the pressure gradient inside the porous fluid flow. For small fluid velocities and low permeabilities, all terms in Eq. (3.3) except the pressure gradient ∇p and the Darcy sink-term could be neglected, which again would lead to the Darcy equation.

To simulate the two-phase flow of resin and air by a VoF scheme, additionally the phase fraction equation

$$\frac{\delta\alpha}{\delta t} = \nabla\,(\alpha\mathbf{u}) \tag{3.5}$$

is solved, where α with $0 \le \alpha \le 1$ is the resin fill factor. In OpenFOAM, Eq. (3.5) is solved using the implemented MULES (Multidimensional Universal Limiter with Explicit Solution) solver, which is commonly used for different types of multi-phase flow and is explained in detail by Deshpande et al. [79]. However, it is also possible to use different sorts of VoF solvers, like e.g. the isoAdvector scheme [80].

In the two-phase VoF scheme, general scalar material properties ψ are calculated by a local averaging with the fill factor α:

$$\psi = \alpha\cdot\psi_{\text{resin}} + (1-\alpha)\cdot\psi_{\text{air}}\,. \tag{3.6}$$

This enables using only one set of equations for both fluid phases, where the different flow behavior is captured by the changing material properties.
The equations can be numerically solved by the FV method. Therefore, the solution domain is discretized into small control volumes (CV) where the computational point is located at the centroid of the cell. The shape of the CV can be any closed polyhedron with flat surfaces. The method uses the integral form of the differential equations and the Gauss' theorem to transpose the volume integrals of the spatial derivatives to surface integrals of the cell faces, which leads to several volume and surface integrals that have to be evaluated.
The models and equations are integrated into the open-source framework OpenFOAM®, which allows using the already implemented schemes to calculate e.g. temporal derivatives or local gradients. It also enables using fast solution algorithms like multi-grid approaches and, furthermore, allows using the parallelization methods embedded into the OpenFOAM framework [**?**]. The discretization procedure as implemented in OpenFOAM is described in detail by Jasak [81].
The basic method of using the Navier-Stokes equations with an additional drag term was developed and already successfully used for mold-filling simulations involving local anisotropic permeabilities [9, 75]. Based on this method, the RTM mold-filling simulation method for non-constant cavities is developed in the following.

3.2.2 Governing equations for moving meshes

The equations that are given in the following focus on the FV method discretized on a moving mesh, which is needed for advanced process variants such as C-RTM or PC-RTM and also for a coupled mold-filling with an embedded foam core.
To realize the movement, the capability of the existing RTM solver [75] is extended to the use of dynamic meshes with the available "dynamicMesh"

library of OpenFOAM that offers different types of mesh motion solvers. The method itself is independent of the mesh motion type used. It can be an artificial movement to preserve mesh quality like it is normally used in FSI. However, it can also be a motion that describes the mechanical behavior of the porous medium, which will be further explained in Chapter 4.

The approach uses a mixed Lagrangian-Eulerian form of the governing equations with the relative velocity of the fluid to the computational mesh. The general governing continuity equation for a tensorial property $\mathbf{\Phi}$ for a moving volume Ω with a closed surface Γ in integral form is:

$$\frac{\mathrm{d}}{\mathrm{d}t}\int_{\Omega}\rho\mathbf{\Phi}\,\mathrm{d}\Omega+\oint_{\Gamma}\rho\mathbf{n}\cdot(\mathbf{u}-\mathbf{u}_s)\mathbf{\Phi}\,\mathrm{d}\Gamma-\oint_{\Gamma}\rho\mu_{\Phi}\mathbf{n}\cdot\nabla\mathbf{\Phi}\,\mathrm{d}\Gamma=\int_{\Omega}q_{\Phi}\,\mathrm{d}\Omega, \quad (3.7)$$

where $\mathbf{n}$ is the unit normal vector on the boundary surface, $\mathbf{u}_s$ is the velocity of the cell boundary surface, μ_{Φ} is the diffusion coefficient and q_{Φ} is the volume source of $\mathbf{\Phi}$. The convection term $\oint_{\Gamma}\rho\mathbf{n}\cdot(\mathbf{u}-\mathbf{u}_s)\mathbf{\Phi}\,\mathrm{d}\Gamma$ uses the relative velocity $(\mathbf{u}-\mathbf{u}_s)$ of the fluid to the mesh surfaces. Consequently, this form is used for all equations that include a convection term.

The FV discretization of the convection term assuming linearity yields

$$\oint_{\Gamma}\rho\mathbf{n}\cdot(\mathbf{u}-\mathbf{u}_s)\mathbf{\Phi}\,\mathrm{d}\Gamma=\sum_{f}\rho_f\left(\dot{m}_f-\dot{V}_f\right)\Phi_f\,, \quad (3.8)$$

with the fluid flux $\dot{m}_f=\mathbf{n}_f\cdot\mathbf{u}_f\Gamma_f$ and the volumetric face flux $\dot{V}_f=\mathbf{n}_f\cdot\mathbf{u}_{s,f}\Gamma_f$ through the cell faces f with the face-interpolated fluid velocity $\mathbf{u}_f$ and the surface-interpolated mesh velocity $\mathbf{u}_{s,f}$.

After solving for the mesh motion, the velocity of the cell surfaces $\mathbf{u}_s$ is known and Eq. 3.7 can be solved using the same methods as for stationary meshes. Afterward, the absolute velocity is calculated again using $\mathbf{u}_s$. This approach satisfies the space conservation law (SCL) [82] and allows the calculation of the fluid flow on arbitrary moving meshes without adding any numerical error.

The fluxes themselves are constructed in a conservative way to assure the mass conservation of the fluid [83]. For a detailed explanation of the discretization of continuity and momentum equation on moving meshes, the reader is referred to the works of Ferziger and Peric or Jasak [84, 85].

3.2.3 Treatment of the porous fluid velocity [1]

When the fibrous preform is homogenized to a porous medium, the solid fibers are not explicitly dissolved, which leads to the difference in the real physical and the volume-averaged fluid velocity [63].
The original Darcy equation (3.1) is defined with the volume-averaged velocity $\tilde{\mathbf{u}}$, which is related to the homogenized physical fluid velocity inside the porous medium by the porosity $\phi = 1 - \varphi$. This is schematically illustrated in Fig. 3.2. To correctly capture the flow front in the porous domain, the homogenized physical fluid velocity has to be used. For a given volume flow rate, a porosity $\phi < 1$ accelerates the fluid. Consequently also the flow front needs to be accelerated to account for the already occupied volume by the fibers.

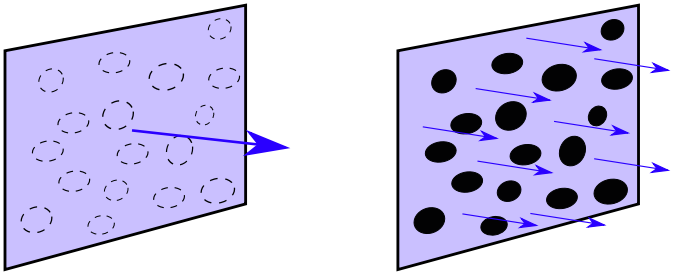

Figure 3.2: Schematic difference between homogenized volume-averaged flow velocity and physical flow velocity between individual filaments at micro-scale

[1] Parts of this section are based on [77]

Therefore, the discretized face fluxes $\dot{m}_f$ (Eq. (3.8)) are divided by the face porosity ϕ_f, which is interpolated from the adjacent cell centers:

$$\tilde{\dot{m}}_f = \mathbf{n}_f \cdot \frac{\mathbf{u}_f}{\phi_f} \Gamma_f. \tag{3.9}$$

For a porosity of $\phi_f = 1$, the approach yields the original fluid flux. To be consistent with Darcy's law that is given in terms of the volume-averaged velocity $\tilde{\mathbf{u}}$, the homogenized physical velocity is only used to advance the flow front.

Knowing the initial fiber volume fraction φ_0 and the initial volume V_0 of a CV in a deforming mesh, the current fiber volume fraction φ_u (or porosity ϕ_u) at each time-step can be calculated by using the mass continuity of the fibers in the simplified form:

$$\varphi_\mathrm{u} = (1 - \phi_\mathrm{u}) = \varphi_0 \cdot \frac{V_0}{V_\mathrm{u}}\,. \tag{3.10}$$

This is only strictly valid, when the mesh motion is equal to the motion of the fabric, as it assumes that no fibers leave or enter a CV. When the mesh motion is solved using a Lagrangian solid mechanics approach, this assumption is true. Furthermore, the fibers are assumed to be incompressible.

3.2.4 The Darcy momentum source term

The porous drag of the fibers on the resin flow is implemented into the discretized form of the momentum equation with the Darcy momentum source term (Eq. (3.4)). Therefore, the linearized volumetric Darcy source term is discretized in a CV by using the integral form:

$$\mathbf{Q}_{\mathrm{Darcy},p} = \int_\Omega -\left(\mu \mathbf{K}^{-1} \tilde{\mathbf{u}}\right) \mathrm{d}\Omega = -\left(\mu_p \mathbf{K}_p^{-1} \mathbf{u}_p\right) \cdot \Omega_p\,, \tag{3.11}$$

with the index p denoting value at the cell center point. Here, the fluid velocity $\mathbf{u}_p$ is given in the form of the volume-averaged Darcy velocity $\tilde{\mathbf{u}}$ to correctly

apply Darcy's law. The negative sign of this term implies that it is a momentum sink, which is correct for a drag term.
Instead of just adding this term to the source part, it is important to check the diagonal dominance of the system that is needed for convergence. To ensure diagonal dominance, the Darcy momentum source term is first split in a hydrostatic and a deviatoric part:

$$\mathbf{Q}_{\mathrm{Darcy},p} = \mathbf{Q}_{\mathrm{hyd},p}\,\mathbf{u}_p + \mathbf{Q}_{\mathrm{dev},p} \tag{3.12}$$

with

$$\mathbf{Q}_{\mathrm{hyd},p} = -\mathrm{tr}\left(\mu_p \mathbf{K}_p^{-1}\right) \cdot \Omega_p\,, \tag{3.13}$$

$$\mathbf{Q}_{\mathrm{dev},p} = -\left[\mu_p \mathbf{K}_p^{-1} - \mathbf{I} \cdot \mathrm{tr}\left(\mu_p \mathbf{K}_p^{-1}\right)\right] \cdot \Omega_p \cdot \mathbf{u}_p\,. \tag{3.14}$$

These two parts are integrated into the discretized momentum equation and an algebraic equation is created that can be numerically solved.

3.2.5 Solving the system of equations

The method implemented to solve the discretized equations in OpenFOAM uses a segregated approach ("PISO" - Pressure Implicit with Splitting of Operators) [86]. In this case, a special treatment for the pressure-velocity coupling is required, which is done by first assembling an implicit momentum predictor ("velocity equation") to get an approximated velocity field [81] that includes the source terms:

$$\left(a_p + Q_{\mathrm{hyd},p}\right)\mathbf{u}_p = \mathbf{H}(\mathbf{u}) - \nabla p\,, \tag{3.15}$$

which is a semi-discretized form of the momentum equation with:

$$\mathbf{H}(\mathbf{u}) = -\sum_n a_n \mathbf{u}_n + \frac{\mathbf{u}^0}{\Delta t} + Q_{\mathrm{dev},p}\,, \tag{3.16}$$

with a_p being the matrix coefficient at the CV centers and a_n the matrix coefficient corresponding to the cell neighbors indicated by index n. The term $\frac{\mathbf{u}^0}{\Delta t}$ is the source part of the transient term [81]. All values present at the cell faces are interpolated from the neighboring cell centers and, thus, are also included in a_p and a_n.

Assembling the momentum equations for all CVs gives a system of algebraic equations of the form:

$$[A][u] = [Q], \tag{3.17}$$

where [A] is a sparse matrix with the coefficients $(a_p + Q_{\mathrm{hyd},p})$ on the diagonal and a_n at off-diagonal entries. In this form, $Q_{\mathrm{hyd},p}$ is added explicitly to the diagonal coefficients a_p, because it ensures the diagonal dominance due to its negative value, whereas $Q_{\mathrm{dev},p}$ is added in the source term to the system of equations.

This system of equations is first solved with the pressure gradient and velocity of the old time-step. Afterward, the pressure equation is solved with the approximated velocities, which then are updated explicitly with the new pressure field. Because of the explicit correction, an iterative procedure is used that repeats this pressure/velocity correction procedure until convergence. More details on the solution algorithm for compressible flows are given by Demirdžić et al. [87].

3.3 Material properties

An important part of RTM mold-filling simulations are the material properties. The fabrics used in RTM have very low permeability and, thus, the Darcy drag term dominates the equations. Hence, the two most relevant parameters are the preform permeability and the resin viscosity. Both parameters influence strongly the infiltration behavior. Therefore, an overview of the different types of permeability and viscosity characterizations and models implemented into the simulation method is given in the next sections.

3.3.1 Permeability

Knowledge of the fabric's permeability is one of the most important aspects when trying to predict the resin flow in RTM. In general, permeability (as used in this context) is a homogenized parameter that describes the drag force of the fabric on the fluid flow. In nearly all of the work published, it is assumed that the permeability of a fabric is not depending on process conditions and thus only contains homogenized information of the geometry of the fabric and its rovings and filaments. In RTM, the permeability is very small (approximately 1×10^{-14} m^2 - 1×10^{-8} m^2), depends strongly on FVF and can be highly anisotropic. The permeability models, therefore, are always a function of the FVF and the anisotropic behavior is captured through the definition of permeability as a second-order tensor. The focus of this work is on the mold-filling simulation with NCF that either are quasi-isotropic (biaxial, triaxial fabrics) in terms of the permeability, and on UD-NCF that exhibit a strongly anisotropic permeability.

Until now, no standard method for the experimental determination of in-plane permeabilities [88, 89] exists, though recent benchmark studies suggest using transparent molds and visually track the flow front by applying a constant inlet pressure [90, 91], while another method uses pressure sensors in an RTM mold [92] to measure as close as possible to real RTM conditions. While

permeability is a material parameter of the porous fabric and, thus, only valid for flow inside the porous domain, mold-filling is also influenced by small resin channels outside the porous domain. This "race-tracking" phenomenon occurs e.g. when the fabric does not completely fill out the cavity at the borders of the part or at sharp edges inside the cavity [44, 93, 94]. In these areas, a free surface flow of the resin exists, which has the properties of a Stokes flow and can be modeled by using the method developed in this thesis by locally neglecting the Darcy momentum sink term. Another possibility is using Brinkman's equation, which couples a Darcy flow regime and a viscous flow regime [95].
Besides the experimental determination of the permeability, also analytical approaches exist. They are mostly based on the work of Gebart [96], who adapted the Kozeny-Carman equation [97, 98] for fibrous porous media:

$$K_{\parallel} = \frac{8r^2}{c} \cdot \frac{(1-\varphi)^3}{\varphi^2}, \tag{3.18}$$

$$K_{\perp} = C_1 r^2 \cdot \left(\sqrt{\frac{\varphi_{\max}}{\varphi}} - 1 \right)^{5/2}, \tag{3.19}$$

with the permeabilities $K_{\parallel}$ and $K_{\perp}$ for flow parallel and transverse to the fibers, and the effective filament radius r. C_1 and c are variables depending on the fiber array type (quadratic or hexagonal) and $\varphi_{\max}$ is the maximum FVF also depending on the type of fiber array. The Gebart equation for $K_{\parallel}$ can be written as

$$K_{\parallel} = A \cdot \frac{(1-\varphi)^3}{\varphi^2}, \tag{3.20}$$

with $A = \frac{8r^2}{c}$. To use the Gebart model in combination with experimental permeability measurements, the value of A can be used as a fitting parameter. Although this equation is purely based on the assumption of a regular fiber array on micro-scale, it can be used to describe the flow inside of rovings or as a simplified model in verification examples. A better result for micro-scale permeabilities is obtained by using statistical volume elements to represent

the irregular fiber array [99, 100] though the real fiber distribution cannot be captured perfectly by statistical models [101]. To homogenize the permeability from micro-scale to macro-scale, virtual approaches to capture the meso-scale were developed, especially for woven fabrics [102–104].

The anisotropic permeability is implemented using local fiber orientations, where first a local cartesian coordinate system $x'y'z'$ is defined that is oriented in the fiber direction. In this local system, only entries on the main diagonal of the permeability tensor exist:

$$\mathbf{K}' = \begin{bmatrix} K_{11} & 0 & 0 \\ 0 & K_{22} & 0 \\ 0 & 0 & K_{33} \end{bmatrix}, \tag{3.21}$$

K_{11} represents the permeability value in the direction of the highest in-plane permeability (for UD fabrics equal to fiber orientation), whereas K_{22} is the lowest in-plane permeability (perpendicular to fiber direction). The influence of the through-thickness permeability K_{33} can usually be neglected because of the small thicknesses of composite parts [90]. In thick parts, K_{33} is usually smaller than K_{22} because of the higher tortuosity of the fabrics in the thickness direction.

In the local fiber coordinate system, the permeability in two dimensions can be visualized as an ellipse with the Values of K_{11} and K_{22} as the two principal semi-axes. In three dimensions, the value of K_{33} leads to a tri-axial ellipsoid. This visualization is especially helpful, as it also can be interpreted as a resin flow front advancement for a central injection point. A visualization is given schematically in Fig. 3.3.

The implementation of the permeability models in the simulation method uses a cell-based evaluation to capture local effects. Based on experimental data points for permeability at a certain FVF, first, the principal permeabilities at each cell are calculated with the local FVF. For FVF values in the given data points range, a linear, exponential, or spline interpolation of the neighboring

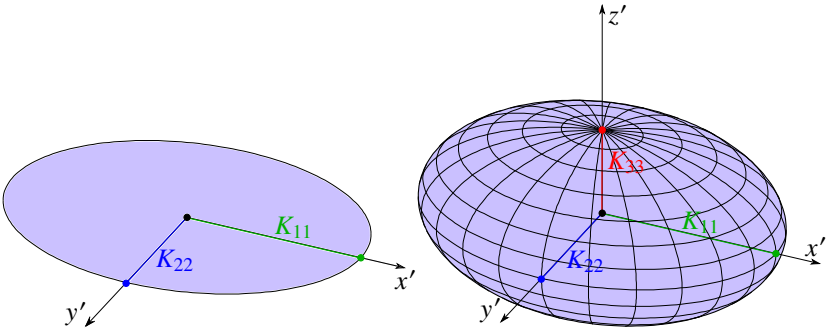

2D permeability ellipse 3D permeability ellipsoid

Figure 3.3: Visualization of the anisotropic permeability in two dimensions and three dimensions in the local principal axis system

values is calculated. In the next step, a rotation tensor $\mathbf{R}$ using Euler angles is determined in each cell to rotate the principal permeability tensor in the local coordinate system to the global cartesian coordinate system xyz. The rotation tensor is calculated by rotating the local coordinate system given by the fiber orientation vector $\boldsymbol{\omega}$ and the thickness direction to the global coordinate system. Hence, the rotation of the permeabilities to the global system is given by:

$$\mathbf{K} = \mathbf{R} \cdot \mathbf{K}' \cdot \mathbf{R}^T \,. \tag{3.22}$$

This approach allows defining the principal permeabilities and local orientations rather than local permeability tensors. The three principal permeabilities can be determined experimentally or by using permeability models.

3.3.2 Viscosity

Besides the modeling of the preform permeability, it is also very important to model the time- and temperature-dependent resin viscosity accurately to predict the mold-filling pattern and the fluid pressure inside the cavity. Especially when using fast curing resin systems, the viscosity can change significantly during the injection and thus influence the cavity pressure. To model the resin viscosity during curing, a kinetic model and a rheology model are required. Kinetic models describe the dependency of the resin cure degree on temperature and time, whereas rheology models describe the viscosity depending on temperature and cure degree. Various models were published to describe the curing behavior of thermoset resins, as e.g. by Kamal and Sourour [105] or Grindling [106]. Often, the rheological behavior is captured with the rheological model by Castro and Macosko [107]. The model parameters for kinetic and rheological model are identified by performing differential scanning calorimeter (DSC) and rheology measurements at different isothermal or non-isothermal conditions. Especially for fast curing resins, this can be a challenging task, as the reaction directly starts after mixing [42, 108], but a preparation time to start the characterization tests is needed.

As pointed out, the resin viscosity μ is a local and time-dependent value. The dynamic viscosity itself is calculated in the VoF approach by local averaging with the fill factor α. The cure degree of the resin is a value inherent to a fluid particle and, thus, is convecting with the resin flow. Therefore, after the solution of the pressure equation and updating the velocity, a scalar transport equation for the cure degree γ is solved:

$$\frac{\partial \rho\gamma}{\partial t} + \nabla \cdot (\rho \mathbf{u}\gamma) = 0\,. \tag{3.23}$$

Subsequently, the cure value at each cell is updated by calculating the cure rate $\dot{\gamma}$ with the chosen kinetic model. The implementation of the cure and viscosity models into the OpenFOAM framework is described by Bernath [43]. This

section, therefore, only contains a short description of the implemented kinetic and rheology models.
The Kamal kinetic model is given by [105]:

$$\dot{\gamma}_{\text{Kamal}}(\gamma, T) = (B_1 + B_2 \cdot \gamma^m) \cdot (1 - \gamma)^n \,, \tag{3.24}$$

$$\begin{aligned} B_1 &= A_1 \cdot e^{-\frac{E_1}{R \cdot T}} \,, \\ B_2 &= A_2 \cdot e^{-\frac{E_2}{R \cdot T}} \,, \end{aligned} \tag{3.25}$$

with the temperature T, the universal gas constant R and the model parameters A_1, A_2, E_1, E_2, m, n that can be calculated for example by curve fitting of the response rates from DSC measurements. The model does not include the glass transition temperature and, therefore, cannot represent premature vitrification [42]. A more sophisticated model that includes the glass transition temperature is the Grindling kinetic model [106]:

$$\begin{aligned} \dot{\gamma}_{\text{Grindling}}(\gamma, T) &= B_1 \cdot (1 - \gamma)^{n_1} + B_{\text{eff}} \cdot \gamma^m \cdot (1 - \gamma)^{n_2} \,, \\ \frac{1}{B_{\text{eff}}} &= \frac{1}{B_{2,\text{diff}}} + \frac{1}{B_2} \,, \end{aligned} \tag{3.26}$$

where B_1 and B_2 are reaction speed functions constrained only by the chemistry and are calculated equal to the model by Kamal. $B_{2,\text{diff}}$ is a reaction speed function, which is limited by diffusion and thus also represents the reaction below glass transition temperature. The fit-function can be an exponential function like:

$$B_{2,\text{diff}} = B_{2,\Delta T_g} \cdot e^{c_1 \cdot \frac{T - T_g}{c_2 + T - T_g}} \,, \tag{3.27}$$

with the fitting parameters $B_{2,\Delta T_g}, c_1, c_2$. To fit $B_{2,\text{diff}}$ to the experimental data, furthermore the relationship between T_g and γ must be modeled, which is normally achieved using the DiBenedetto function:

$$T_g(\gamma) = \frac{\lambda \cdot \gamma}{1 - (1 - \lambda) \cdot \gamma} \cdot (T_{g,\infty} - T_{g,0}) + T_{g,0}\,, \tag{3.28}$$

where $T_{g,0}$ is the glass transition temperature of the uncured polymer (usually < 0 °C), $T_{g,\infty}$ is the glass transition temperature of the fully cured polymer and λ is the fitting parameter. Because of the numerous fitting parameters, the Grindling kinetic model is best parameterized using e.g. genetic optimization algorithms to minimize the model error.

After calculating the cure rate and updating the cure degree, the rheology model updates the viscosity in each cell considering temperature and cure degree. The Castro-Macosko viscosity model [107] is implemented, which is given by:

$$\mu(\gamma, T) = \mu_0 \cdot \left[\frac{\gamma_g}{\gamma_g - \gamma}\right]^{C_1 + C_2 \cdot \gamma}\,, \tag{3.29}$$

$$\mu_0 = D \cdot e^{\frac{T_b}{R \cdot T}}\,, \tag{3.30}$$

with the cure degree at the point of gelation γ_g and the model parameters D, C_1, C_2 and T_b. This model is a combination of a power-law function and an Arrhenius function, which are both very common for modeling the viscosity of polymers [109]. γ_g is defined by the point when the resin can build any stresses and has to be measured experimentally using e.g. parallel-plate rheometry and measuring the first occurrence of normal forces [43].

For simplified isothermal simulations, instead of using the combination of kinetic and rheology model, a simple time-dependent viscosity model can be

used. In that case, the viscosity increase over time due to the beginning curing reaction can be described e.g. by a polynomial function of the form:

$$\mu(t_{\text{resin}}) = \sum_{i=0} D_i \cdot t_{\text{resin}}^i \,, \tag{3.31}$$

where D_i are fitting parameters and t_{resin} is the resin age. By using this simplified model, only one isothermal rheological measurement is necessary to describe the viscosity evolution over time. In this model, the resin age is calculated like the cure degree by solving a scalar transport equation and updating the value at each time-step.
The shear-thinning behavior that is present in polymer flows is not taken into account in this thesis. The effect may be present and can be accounted for by using an effective viscosity [110], though the real shear rate results from the heterogeneous microscopic fiber distribution, which is normally not known [111]. The research regarding the flow of non-Newtonian fluids through porous media is a very complex issue and is, therefore, still an ongoing task.

3.4 Solution procedure for non-constant cavities [2]

During mold-filling of RTM variants like C-RTM or PC-RTM, the cavity geometry is not constant but changes throughout the process. This behavior is captured in the simulation method by using a moving mesh and updating the permeability of the fabric depending on the current FVF.
The solution algorithm for C-RTM is shown in Fig. 3.4. It consists of the motion of the mesh, which is followed by the update of the permeability based on the new cell geometry. With the calculated FVF and given fiber orientation, the

[2] Parts of this section are based on [32] and [77]

local permeability at every cell is evaluated in each time-step using analytical models or experimental data, like explained in Section 3.3.1.
After updating the permeability, the segregated pressure-velocity coupling is used to solve the resin flow with an iterative repetition until convergence. During this step, the phase fraction equation, the momentum equation, and the pressure equation are solved. For non-isothermal flows, furthermore, the temperature equation and the cure degree equation are added. The temperature-based form of the energy equation is solved using the OpenFOAM implementation, described e.g. by Bernath [43].
The PC-RTM solution algorithm consists of the C-RTM algorithm and is extended by a control algorithm that sets the compression velocity in each time-step based on the result of the pressure solution of the old time-step. Therefore, a virtual PID (proportional-integral-derivative) controller is set as a boundary condition to calculate the current closing speed of the mold based on the pressure at a fixed position in the simulation domain. This represents the control behavior of the real PC-RTM process that uses an integrated pressure sensor in the cavity [31].
When a termination criterium is reached, the simulation stops. Possible criteria are e.g. a maximum simulation time, a completely filled mold, or a maximum cure degree reached.
This method is the basis for the following derived methods containing a non-constant geometry. The numerical method and the processes as investigated in this work are limited to a mold gap height that still ensures that the preform is in touch with the mold wall and no open gap above the preform exists. For large mold openings, a method to describe the formation of gaps based on the local cavity height is needed. A more accurate but also more sophisticated possibility is the volume-coupling of a porous solid mechanics method for the preform deformation with the mold-filling in a partitioned approach like shown in the outlook of this thesis (Chapter 8, Fig. 8.1).

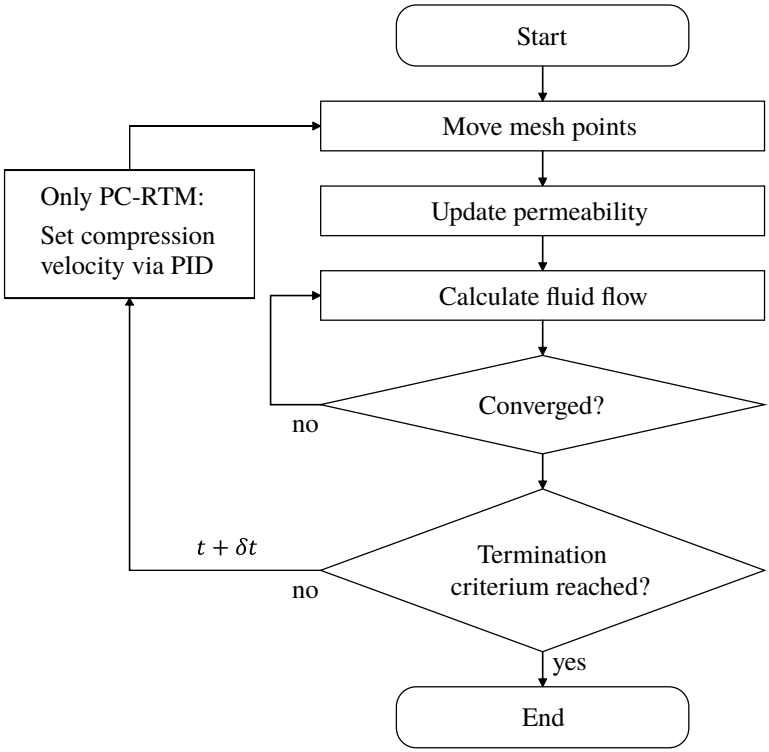

Figure 3.4: Solution algorithm for C-RTM and PC-RTM based on a resin flow inside a non-constant cavity

3.5 Verification

The verification of the developed method for non-constant cavities is carried out with the simulation of a one-dimensional mold-filling of a rectangular plate using PC-RTM. The simulation starts with an initial fiber volume fraction of 33.3% at a mold height of 3 mm and aims to reach a final mold height of 2 mm, which leads to a final fiber volume fraction of 50%. The resin is injected with a constant mass flow rate and after the pressure-control value is reached the first

Table 3.1: Process and material parameters for the PC-RTM verification case

Parameter	**Value**
Mold width	0.2 m
Injection flow rate	$4000\,\mathrm{mm^3\,s^{-1}}$
Injection time	10 s
Initial fiber volume fraction	0.333
Initial mold height	3 mm
Final mold height	2 mm
Pressure-control value	4 bar
Gebart parameter A	$5.44 \times 10^{-11}\,\mathrm{m^2}$

time, the PID controller starts to control the mold height with the aim to hold a constant pressure of 4 bar.

In the verification case, the dependency of the permeability on the FVF is implemented based on the Gebart equation (3.20). The value of A is calculated based on permeability measurements of a non-crimp unidirectional carbon fiber reinforcement that is presented in Section 5.4. The measured permeability at a FVF of 50% is $K_{\parallel,exp} = 2.72 \cdot 10^{-11}\,\mathrm{m^2}$. The verification model geometry, material, and process parameters are summarized in Table 3.1.

The analytical solution of PC-RTM mold-filling for a one-dimensional Darcy-flow is given in Appendix A. Figure 3.5 shows the verification results of the PC-RTM mold filling simulation. Two important process values are compared; the inlet pressure and the mold gap height, which is defined as the gap referenced to the final cavity height. Both results show the same behavior during mold-filling. First, the pressure increases linearly at a constant mold gap height. When the pressure-control value is reached, the mold gap height increases and the pressure stays at a constant level. After approximately 10 s, the mold filling stops, which is indicated by the start of the decreasing mold gap height.

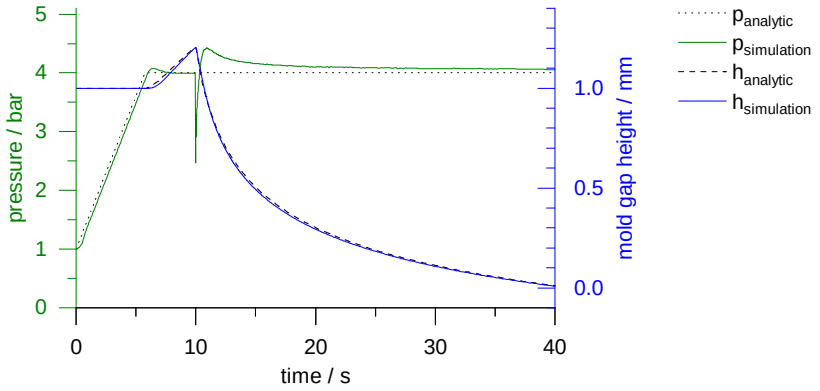

Figure 3.5: Result of the one-dimensional PC-RTM verification case; pressure at the inlet and mold gap height is compared for simulation and analytical solution

The three stages of PC-RTM (cf. Fig. 2.4) are clearly visible in the simulation result as well as in the analytical solution.

The simulation shows a very good agreement with the analytical Darcy solution for both of the values. Only a slight pressure overshoot in the simulation can be observed. First, when reaching the pressure limit in Stage 1, and secondly, when changing the boundary conditions from injection to compression. This overshoot is explained by the behavior of the integrated PID controller. Typically, such an overshooting behavior is caused by system disturbances. In PC-RTM, this is induced by the change of the boundary conditions from Stage 1 to Stage 2 and from Stage 2 to Stage 3.

3.6 Discussion

The method presented in this chapter focuses on the numerical description of the resin and air flowing inside a porous medium inside a non-constant cavity. The previously available method was limited to RTM with a constant cavity and static fabric properties throughout the mold-filling. By enhancing the method for moving meshes with an updating of the material parameters (fiber volume fraction, permeability), it is possible to simulate the mold-filling of C-RTM and PC-RTM, which was already shown by the author [77, 78] and is, in this work, furthermore verified for PC-RTM. The verification shows a very good agreement of the mold-filling simulation with the analytical solution. An even better result and diminishing the influence of the PID-controller could be obtained by iterating over each time-step during the pressure-controlled stages until an exact solution is found.

The developed method can be flexibly used for RTM mold-filling using constant or cure-dependent viscosity, for isothermal or non-isothermal mold-filling, for simplified two-dimensional as well as complex three-dimensional components. In general, the method presented for modeling a porous fluid flow inside a changing cavity is the basis for modeling various manufacturing processes of CoFRP that have a non-constant cavity throughout the mold-filling.

For example it is possible to simulate the infiltration in rotational molding by adding a centrifugal body force to the resin, which was shown recently by Nieschlag et al. [112]. Furthermore, the implementation of the permeability utilizing local information of the FVF and fiber orientation enables to add local effects on mold-filling like race-tracking at sub-preform overlaps or near embedded metal inserts to the simulation model [9, 78, 113].

By using one of the implemented rheology models or a time-depending viscosity for a constant temperature, it is possible to consider a viscosity change during the mold-filling. This not only allows to better simulate filling time and cavity pressure, which is important for PC-RTM [32], but also enables to use of

information of the local cure degree to predict curing time or as an initial condition for distortion or residual stress analyses [43, 114].
By modeling the mold-filling with a two-phase flow, a better prediction of air entrapment is possible, which was already shown in previous studies using this method [9**?**]. Furthermore, by solving the complete Navier-Stokes equations with porous drag term, it is possible to model fluid flow in porous media but also a two-phase free flow, where the momentum sink term vanishes. This will be an important feature in future studies, where open gaps do not have to be modeled by using artificial effective permeability values.
A validation of PC-RTM mold-filling simulations for a plate geometry showed good comparability to experimental results [32]. However, the experiments showed a difference in the initial pressure at the beginning of the injection and during the compression stage. This is a result of the compaction force of the fabric inside the mold, which adds a force to the fluid pressure that is measured by the integrated pressure sensor. This influences the pressure-control, as the value measured is in fact not the fluid pressure, but the total stress of the porous fabric. To capture this in the simulations, a coupled poro-elasticity and mold-filling method needs to be developed, which is part of the following chapter.

4 Mold-filling Simulation Method for RTM with FSI

This chapter focuses on the development of an FV-based method for the RTM mold-filling coupled with fabric and foam core deformation. The method developed consists of three parts. First, the "fluid" part describes the flow of the liquid resin inside the fabric, which is described in the previous chapter. Secondly, the "internal porous solid" part, which is the fabric that behaves like a deformable porous medium, where the deformation is depending on external forces and the resin flowing inside of it. And finally, the "external solid", which can be any kind of flexible or compressible structure embedded into the layup (like polymer foam cores) or a boundary of the cavity (like non-rigid tools). This chapter focuses on the development of the method to model the internal porous solid, the internal coupling between fluid flow and porous solid as well as the FSI coupling to an external solid. After an introduction and a review of the related work in the first section, the method to model the fabric deformation is explained in Section 4.2. Subsequently, the internal coupling method between fabric deformation and mold-filling is verified (Section 4.3). Afterward, the solution procedure for the coupling to an external structure is shown and verified in Section 4.4. Finally, the developments are discussed in Section 4.5.

4.1 Introduction and review of related work

The description of a porous medium in terms of solid mechanics is based on Terzaghi's law [115], as long as the continuous solid material inside the porous medium is incompressible compared to the homogenized porous medium. In terms of fiber-reinforced composites, this is a valid assumption, as the compressibility of the fabric is orders of magnitude higher than that of the fibers themselves. Terzaghi defined the "effective" stress inside the porous medium to decouple the solid stress from the fluid stress:

$$\begin{aligned} \sigma_{\text{total}} &= \sigma_{\text{eff}} + \sigma_{\text{fluid}} \\ &= \sigma_{\text{eff}} - p\mathbf{I}, \end{aligned} \tag{4.1}$$

where p is the fluid pressure inside the porous medium, which acts as additional normal stress inside the solid. The effective stress approach is a state-of-the-art in geomechanics since many years and is especially used in combination with groundwater flow to predict the deformation of fluid saturated soils [116]. Based on this stress definition, the equilibrium equations and material models can be described in terms of effective stresses. The solid mechanics' convention of tension resulting in positive stresses and compression resulting in negative stresses is used in this work, whereas the fluid pressure is always positive.
In RTM, Binetruy and Advani [16] modeled and analyzed mold-filling with embedded foam cores. They developed an analytical model that couples the mold-filling and foam core deformation for a simplified one-dimensional flow. They also compared the model to an experimental test case and reported a good agreement but highlighted the need for more sophisticated material models to describe the foam core. Deleglise et al. [117] modeled the mold-filling for C-RTM and for RTM with embedded foam cores. They coupled a two-dimensional model for resin flow with a linear-elastic one-dimensional spring model for the closed-cell foam core. They reported the same mold-filling behavior as Binetruy

and Advani [16] and additionally state that the coupling can be modeled quasi-statically because the preform deformation rate is much lower than the fluid flow deformation rate in most of the parts. Both publications do not model the porous fabric deformation during the mold filling. Furthermore, they assume a one-dimensional linear-elastic compression of the foam core.

Besides these few publications, the coupled RTM mold-filling including deformation of an embedded foam core has not been studied. The approaches are limited to two-dimensional solutions, which limits the methods developed to specific applications and simple plate geometries. To the author's knowledge, there is no holistic and three-dimensional approach investigating the RTM mold-filling with embedded foam cores including fabric deformation.

However, the coupling of fluid flow and fabric deformation is of interest in the area of VARI infiltration. Here, the fabric compression behavior directly influences the local thickness and, thus, the mold-filling time and the achievable FVF. Several authors modeled the infiltration in VARI, starting from analytical models [118, 119] to numerical simulation of the mold-filling with fabric deformation, [33, 120–122]. In recent publications by Simacek and Advani [121] and Wu et al. [122], a simplified 2D model for mold-filling in VARI with the focus on fast convergence and reasonable accuracy is used. Dereims et al. [123] couple a non-linear solid mechanics model for the fabric compression to a Darcy and a Stokes flow regime by using a three-dimensional FE approach for application in C-RTM mold-filling. Their FE-based method shows a very good agreement to analytical solutions. However, in their approach, they need to implement an artificial viscosity to stabilize the Stokes flow and a second non-physical parameter to control the interface velocity between the Darcy and Stokes flow. By solving the full Navier-Stokes equations with a momentum sink term active in the porous domain, as proposed in this work, this can be avoided.

In WCM, especially the deformation characteristics inside a layer and the friction between fabric layers at very large deformations have to be modeled [6].

The simultaneous forming and infiltration lead to a further increase in complexity because it affects the shear and friction behavior of the fabric [124, 125]. To model the concurrent draping and infiltration, Poppe et al. [37, 38] proposed a two-dimensional and a three-dimensional FE formulation that uses the analogy of the heat transfer equation to the Darcy equation. They verify this approach and show that it is well-suited to capture the flow in a porous medium undergoing large deformations (including compression) with a focus on predicting the formation of wrinkles in WCM.

If a foam core is embedded between the fabrics, it has to withstand compression loads of two types during RTM mold-filling. First, the closing of the tool compresses the fiber reinforcement in the top sheets and clamps the foam core between them. Secondly, hydrostatic pressure builds inside the cavity that acts as an additional compression load on the foam core material during the injection of the liquid resin. Those compression loads lead to several possible defects. Al-Hamdan et al. [15] classified five defects of RTM sandwich parts that are: incomplete filling, delamination, core shift, core deformation, and core-collapse. Those defects can further be divided into resulting defects of the part that are incomplete filling (dry spots) and delamination and on the other hand defects of the core material itself (core shift, deformation, and collapse). The authors did not further focus on the incomplete filling but on the comparison of different core materials regarding delamination and resin absorption. The authors also show experimentally that core shift plays a minor role compared to core deformation and core-collapse when manufacturing sandwich parts with high FVF [126].

Mold-filling in RTM with an embedded deformable foam core can be defined as an FSI problem involving three participants: resin flow, fabric deformation, and foam core deformation. In general, two different approaches exist to solve FSI problems. The monolithic approach uses one solution domain and one numerical method for all components. This has the advantage that only one mesh has to be generated and that no mapping methods and no special solution procedures are needed as all parts are solved simultaneously. The

main disadvantage of this approach is that in most cases the physics are very different in the components and consequently also the nature of the equations that have to be solved differs considerably. When only one numerical method is used for all components this can lead to slow convergence as it is not possible to use always the best method or time-step size for each component individually. On the contrary, this is the big advantage of the partitioned approach, where each part can use its best-suited method. Also, the partitioned approach allows to add or change components more flexibly compared to a monolithic approach. The disadvantages of the partitioned approach are, that normally the meshes do not coincide and special solution procedures are needed to find the common solution for all components. This makes mapping methods necessary and, furthermore, means that additional iterations in each time-step are required. As both approaches have their advantages and drawbacks, it is important to choose the right approach. A good overview of FSI problems and approaches is given by Hou et al. [127]. In the literature, the coupling of resin flow and fabric deformation and also the coupling between resin flow and foam core deformation is always conducted using monolithic approaches. To date, an FSI coupling containing the three participants is not existing to the author's knowledge.

As the internal fluid-solid coupling of mold-filling inside a porous medium uses the same simulation domain for both partners, a monolithic approach is favored in that case, whereas the coupling to the deforming foam core happens on a defined surface and, thus, a partitioned approach is better suited here.

Based on the review of the related work, the requirements on a coupled RTM mold-filling and foam core deformation method are derived:

1. Use a three-dimensional approach to enable modeling complex parts.
2. Couple the preform compression and the fluid pressure using Terzaghi's law in a monolithic approach.
3. Include the most relevant constitutive models for fabric compression.

4. Allow to couple the mold-filling to external codes/models for partitioned FSI.
5. Embed the RTM mold-filling method described in Chapter 3.

With these requirements, the coupled method is developed and verified, which is exemplified in the next sections.

4.2 The finite volume method for porous solid mechanics

The commercially available solid mechanics software is normally based on FE formulations. Modeling solid mechanics based on FV discretization is a rather unconventional approach, but nevertheless worth investigating. The first efforts for a cell-centered finite volume approach were made already 30 years ago by Demirdžić [83]. It was later used and further developed in some academic research codes and applications, e.g. for thermal stresses in crystal growth or crack propagation in multi-phase materials [128–131]. An extensive overview of the work done is given by Cardiff and Demirdžić [132].

In the last decade, the main work to implement an FV formulation for solid mechanic problems was done by Cardiff [133], who also published the code under an open-source license ("solids4foam" [134]). He further developed the method by Demirdžić and also implemented advanced methods for large strains, anisotropic material, or contact boundaries [135–137].

Based on the implementation into the open-source framework of OpenFOAM, Tang et al. [138] developed a method for small strain poro-elasticity. They use Terzaghi's law for effective stress in an elastic-plastic porous medium and couple it to a seepage equation to simulate the consolidation and the load-bearing of saturated soil. They also showed a very good computational efficiency compared to an implicit FE method. The method in this work combines both

developments: The large strain method [135] and the poro-elasticity method [138].

4.2.1 Governing equations

The solid mechanics of the porous fiber reinforcement is defined in a similar manner to fluid mechanics. To be able to model large deformations, especially for the thickness direction of the fabric, the method uses a updated Lagrangian formulation. For this approach and without any thermo-mechanic coupling, only the momentum equation is required. The equation used is closely related to Eq. (3.7) but in the Lagrangian formulation, the material velocity $\mathbf{u}$ is equal to the velocity of the mesh $\mathbf{u}_s$ and, thus, the convection term is zero. Furthermore, Eq. (3.7) is given with the constitutive model of a Newtonian fluid, where the stresses in the fluid are incorporated in the viscous term.
Without this constitutive model, the conservation of linear momentum for a general control volume Ω with a surface Γ and unit normal $\mathbf{n}$ in integral form can be written as:

$$\frac{\delta}{\delta t}\int_{\Omega}\rho\,\mathbf{u}\,\mathrm{d}\Omega = \oint_{\Gamma}\mathbf{n}\cdot\sigma\,\mathrm{d}\Gamma + \int_{\Omega}\rho\,\mathbf{b}\,\mathrm{d}\Omega\,, \tag{4.2}$$

with the solid velocity $\mathbf{u}$, the stress tensor σ, the body forces $\mathbf{b}$ and the solid density ρ.
While only the viscosity is used to close the equations for a Newtonian fluid, a constitutive relation that correlates the stresses to strains is needed in case of elastic solid mechanics. To capture large strains and rotations, the St. Venant-Kirchhoff hyper-elastic constitutive relation is used that is described in terms of the effective stress:

$$\mathbf{S}_{\mathrm{eff}} = 2\mu_{\mathrm{L}}\,\mathbf{E} + \lambda_{\mathrm{L}}\,\mathrm{tr}(\mathbf{E})\mathbf{I} = \mathbf{C} : \mathbf{E}\,, \tag{4.3}$$

with the second Piola-Kirchhoff stress tensor $\mathbf{S}$, the first and second Lamé coefficients μ_L and λ_L, the stiffness tensor $\mathbf{C}$ and the Green-Lagrange strain tensor $\mathbf{E}$ that is given by:

$$\mathbf{E} = \frac{1}{2}(\nabla\mathbf{d} + \nabla\mathbf{d}^\top + \nabla\mathbf{d} \cdot \nabla\mathbf{d}^\top), \tag{4.4}$$

with the displacement vector $\mathbf{d}$. When using an incremental approach, the following form applies for the incremental strain $\delta\mathbf{E}$:

$$\delta\mathbf{E} = \frac{1}{2}(\nabla\delta\mathbf{d} + \nabla\delta\mathbf{d}^\top + \nabla\delta\mathbf{d} \cdot \nabla\mathbf{d}^\top + \nabla\mathbf{d} \cdot \nabla\delta\mathbf{d}^\top + \nabla\delta\mathbf{d} \cdot \nabla\delta\mathbf{d}^\top). \tag{4.5}$$

The large strain method is implemented in an updated incremental Lagrangian form. In each time-step the geometry and the configuration is updated and set as the new reference configuration. The stresses and strains have to be corrected to refer to the current configuration with the deformation gradient $\mathbf{F} = \mathbf{I} + \nabla\mathbf{d}$ and the Jacobian $J = \det(\mathbf{F})$:

$$\mathbf{E}_\mathrm{u} = \mathbf{F}^{-1} \cdot \mathbf{E} \cdot \mathbf{F}^{-\top}, \tag{4.6}$$

$$\mathbf{S}_\mathrm{eff,u} = J^{-1}\mathbf{F}^\top \cdot \mathbf{S}_\mathrm{eff} \cdot \mathbf{F}. \tag{4.7}$$

One advantage of this method is that the initial displacement at a time increment is zero and thus simplifies a lot of the equations. For the updated state, the Green strain tensor in incremental form is:

$$\delta\mathbf{E}_\mathrm{u} = \frac{1}{2}(\nabla\delta\mathbf{d} + \nabla\delta\mathbf{d}^\top + \nabla\delta\mathbf{d} \cdot \nabla\delta\mathbf{d}^\top). \tag{4.8}$$

For a rigorously correct implementation equal to a total Lagrangian approach, the stiffness tensor **C** should also be updated, but to use the advantages of the updated formulation, it is assumed that the stiffness tensor is not changing:

$$\delta \mathbf{S}_{\mathrm{eff,u}} = (\mathrm{C})_{\mathrm{u}} : \delta \mathbf{E}_{\mathrm{u}} \approx (\mathrm{C}) : \delta \mathbf{E}_{\mathrm{u}} \,, \tag{4.9}$$

$$\delta \mathbf{S}_{\mathrm{eff,u}} \approx 2\mu_{\mathrm{L}}\, \delta \mathbf{E} + \lambda_{\mathrm{L}}\, \mathrm{tr}(\delta \mathbf{E})\mathbf{I} \,, \tag{4.10}$$

where the index u denotes the updated state. The formulation is valid for large incremental displacements and rotations but small incremental strains [139]. However, non-linear elastic material models can be included by updating the Lamé coefficients μ_{L} and λ_{L} in each of the explicit loops (cf. Section 4.2.4).

4.2.2 Extension with Terzaghi's effective stress [1]

The updated Lagrangian formulation for small incremental strains was extended to be used for poro-elasticity by Tang et al. [138], which is based on the work by Cardiff [133]. Based on this approach, a non-linear incremental poro-elasticity method is developed, which allows larger incremental deformations and following larger time-steps to be used in the solution procedure. This is especially important when coupling the porous solid mechanics to the fluid flow. Here, the time-step is defined by the flow velocity of the resin and should not be further decreased by requirements of the poro-elasticity method.
Equation (4.2) can be written using the second Piola-Kirchhoff total stress tensor in the updated configuration:

$$\frac{\delta}{\delta t} \int_{\Omega} \rho\, \mathbf{u}\, \mathrm{d}\Omega = \oint_{\Gamma_{\mathrm{u}}} \mathbf{n}_{\mathrm{u}} \cdot (\mathbf{S} \cdot \mathbf{F})\, \mathrm{d}\Gamma_{\mathrm{u}} + \int_{\Omega_{\mathrm{u}}} \rho\, \mathbf{b}\, \mathrm{d}\Omega_{\mathrm{u}} \,. \tag{4.11}$$

[1] Parts of this section are based on [140]

Without body forces, using the incremental formulation and the simplification of the updated state $\mathbf{F}_\mathrm{u} = \nabla\mathbf{d} = 0$ gives:

$$\frac{\delta}{\delta t}\int_\Omega \rho\,\mathbf{u}\,\mathrm{d}\Omega = \oint_{\Gamma_\mathrm{u}} \mathbf{n}_\mathrm{u}\cdot(\delta\mathbf{S} + \mathbf{S}\cdot\delta\mathbf{F} + \delta\mathbf{S}\cdot\delta\mathbf{F})\,\mathrm{d}\Gamma_\mathrm{u}\,. \tag{4.12}$$

To apply Terzaghi's law (Eq. (4.1)), the stress $\mathbf{S}$ tensor is then split with the effective stress $\mathbf{S}_\mathrm{eff}$ by using the fluid pressure p:

$$\mathbf{S} = \mathbf{S}_\mathrm{eff} - p\mathbf{I}\,, \tag{4.13}$$

and in incremental form:

$$\delta\mathbf{S} = \delta\mathbf{S}_\mathrm{eff} - \delta p\mathbf{I}\,. \tag{4.14}$$

Implementing Eq. (4.13) and Eq. (4.14) into Eq. (4.12) and separating the linear and non-linear parts leads to:

$$\begin{aligned}\frac{\delta}{\delta t}\int_\Omega \rho_\mathrm{u}\,\frac{\delta(\delta\mathbf{d})}{\delta t}\,\mathrm{d}\Omega = &\oint_{\Gamma_\mathrm{u}} \mathbf{n}_\mathrm{u}\cdot\delta\mathbf{S}_\mathrm{eff}\,\mathrm{d}\Gamma_\mathrm{u}\\ &- \oint_{\Gamma_\mathrm{u}} \mathbf{n}_\mathrm{u}\cdot(\delta p\mathbf{I})\,\mathrm{d}\Gamma_\mathrm{u}\\ &+ \oint_{\Gamma_\mathrm{u}} \mathbf{n}_\mathrm{u}\cdot[(\mathbf{S}_\mathrm{eff} - p\mathbf{I} + \delta\mathbf{S}_\mathrm{eff} - \delta p\mathbf{I})\cdot\delta\mathbf{F}]\,\mathrm{d}\Gamma_\mathrm{u}\,.\end{aligned} \tag{4.15}$$

With $\delta\mathbf{F}_\mathrm{u} = \nabla\delta\mathbf{d}$ and inserting Eq. (4.10) for the linear incremental effective stress $\delta\mathbf{S}_\mathrm{eff}$, the finalized form is obtained:

$$\begin{aligned}\frac{\delta}{\delta t}\int_\Omega \rho_\mathrm{u}\,\frac{\delta(\delta\mathbf{d})}{\delta t}\,\mathrm{d}\Omega = &\oint_{\Gamma_\mathrm{u}} \mathbf{n}_\mathrm{u}\cdot\left[2\mu_\mathrm{L}\delta\mathbf{E}_\mathrm{u} + \lambda_\mathrm{L}\,\mathrm{tr}(\delta\mathbf{E}_\mathrm{u})\mathbf{I}\right]\,\mathrm{d}\Gamma_\mathrm{u}\\ &- \oint_{\Gamma_\mathrm{u}} \mathbf{n}_\mathrm{u}\cdot(\delta p\mathbf{I})\,\mathrm{d}\Gamma_\mathrm{u}\\ &+ \oint_{\Gamma_\mathrm{u}} \mathbf{n}_\mathrm{u}\cdot\left[(\mathbf{S}_\mathrm{eff,u} - p\mathbf{I} + \delta\mathbf{S}_\mathrm{eff,u} - \delta p\mathbf{I})\cdot\nabla\delta\mathbf{d}\right]\,\mathrm{d}\Gamma_\mathrm{u}\,.\end{aligned} \tag{4.16}$$

The second and third terms on the right-hand side have an additional dependency on the fluid pressure when compared to the equation for solid mechanics without Terzaghi's effective stress. This form, thus, enables a strong poro-elasticity coupling between the resin flow and the fabric deformation.
For an incremental, linear approach, Eq. (4.16) reduces to:

$$\begin{aligned}\frac{\delta}{\delta t}\int_\Omega \rho_\mathrm{u}\,\frac{\delta(\delta\mathbf{d})}{\delta t}\,\mathrm{d}\Omega = &\oint_{\Gamma_\mathrm{u}} \mathbf{n}_\mathrm{u}\cdot\left[2\mu_\mathrm{L}\delta\mathbf{E}_\mathrm{u} + \lambda_\mathrm{L}\,\mathrm{tr}(\delta\mathbf{E}_\mathrm{u})\mathbf{I}\right]\,\mathrm{d}\Gamma_\mathrm{u}\\ &- \oint_{\Gamma_\mathrm{u}} \mathbf{n}_\mathrm{u}\cdot(\delta p\mathbf{I})\,\mathrm{d}\Gamma_\mathrm{u}\,,\end{aligned} \tag{4.17}$$

with the linear incremental strain:

$$\delta\mathbf{E}_\mathrm{u} = \frac{1}{2}(\nabla\delta\mathbf{d} + \nabla\delta\mathbf{d}^\top)\,, \tag{4.18}$$

which is the form used by Tang et al. [138].

4.2.3 Constitutive model

To close the equations, a constitutive model is needed that assigns the material strains to stresses. The method is given in terms of the second Piola-Kirchhoff stresses and the Lamé parameters μ_L and λ_L (cf. Eq. (4.3)). For an isotropic elastic material, they are defined as:

$$\begin{aligned} \mu_L &= \frac{\nu}{1-2\nu} \cdot \frac{1}{1+\nu} \cdot E\,, \\ \lambda_L &= G = \frac{1}{2} \cdot \frac{1}{1+\nu} \cdot E\,, \end{aligned} \tag{4.19}$$

with the Young's modulus E, the Poisson's ratio ν and the shear modulus G. Besides an isotropic linear-elastic material with a constant Young's modulus and Poisson's ratio, it is also possible to implement e.g. elastic-plastic or orthotropic constitutive models [136, 137].
In this work, the focus of the application lies on the modeling of the compaction behavior of carbon fiber or glass fiber fabrics. Early experimental work showed that the compaction behavior of reinforcement fabrics is highly non-linear with a strongly increasing bulk modulus [141, 142]. They showed that the compaction stress σ_{fabric} can be modeled using a power-law function of the form:

$$\sigma_{\text{fabric}} = C_1 \cdot \varphi^n\,, \tag{4.20}$$

with the fitting parameters C_1 and n.
For this purpose, a hyper-elastic constitutive model is implemented in the poro-elasticity method that uses a local definition of Young's modulus at each cell depending on a scalar strain value $\varepsilon_{\text{equivalent}}$ that can be e.g. the FVF. This implementation results in the linearization of the stiffness around the updated deformation state. The function $E(\varepsilon_{\text{equivalent}})$ can be specified by user-defined

functions like e.g. piecewise linear functions or polynomial functions of the form:

$$E(\varepsilon_{\text{equivalent}}) = \sum_{i=0} B_i \cdot \varphi^i \,, \tag{4.21}$$

with the fitting parameters B_i.

4.2.4 Solution procedure

To solve the equations derived in the last sections, an implicit-explicit solution algorithm proposed by Cardiff [133] is used. Therefore, Eq. (4.16) is rearranged and combined with Eq. (4.8) to an equation of the form:

$$\begin{aligned} \frac{\delta}{\delta t} \int_\Omega \rho \, \frac{\delta(\delta \mathbf{d})}{\delta t} \, \mathrm{d}\Omega = \oint_\Gamma (2\mu_\mathrm{L} + \lambda_\mathrm{L}) \mathbf{n} \cdot \nabla \delta \mathbf{d} \, \mathrm{d}\Gamma \\ + \oint_\Gamma \mathbf{n} \cdot \mathbf{Q}_\Gamma \, \mathrm{d}\Gamma \,. \end{aligned} \tag{4.22}$$

In this form, the right-hand side is split into an implicit and an explicit part. The first term on the right-hand side is solved implicitly while the second term is solved explicitly:

$$\oint_\Gamma \mathbf{n} \cdot \mathbf{Q}_\Gamma \, \mathrm{d}\Gamma \approx \sum_f \Gamma_f \cdot \mathbf{Q}_\Gamma \,, \tag{4.23}$$

with the explicit surface source term $\Gamma_f \cdot \mathbf{Q}_\Gamma$ given by:

$$\begin{aligned}\Gamma_f \cdot \mathbf{Q}_\Gamma =& \mu_{\mathrm{L},f}\Gamma_f \cdot (\nabla\delta\mathbf{d})_f^\top \\ &+ \lambda_{\mathrm{L},f}\Gamma_f \,\mathrm{tr}[(\nabla\delta\mathbf{d})_f] \\ &- (\mu_{\mathrm{L},f} + \lambda_{\mathrm{L},f})[\Gamma_f \cdot (\nabla\delta\mathbf{d})_f] \\ &+ \mu_{\mathrm{L},f}\Gamma_f \cdot [(\nabla\delta\mathbf{d})_f \cdot (\nabla\delta\mathbf{d})_f^\top] \\ &+ \frac{1}{2}\lambda_{\mathrm{L},f}\Gamma_f \,\mathrm{tr}[(\nabla\delta\mathbf{d})_f \cdot (\nabla\delta\mathbf{d})_f^\top] \\ &+ \Gamma_f \cdot [\delta p \cdot \mathbf{I}] \\ &+ \Gamma_f \cdot [(\mathbf{S}_{\mathrm{eff,u}} + \delta\mathbf{S}_{\mathrm{eff,u}}) \cdot \nabla\delta\mathbf{d}]\,.\end{aligned} \tag{4.24}$$

The explicit term contains the coupling to the fluid pressure and the material stresses. It is, therefore, highly non-linear, which is accounted for by iterating over the explicit solutions in a staggered approach until convergence. Especially for large incremental strains this still assures a robust solution procedure.
Furthermore, the material properties of the textile preform that are important for the modeling of the resin flow - FVF φ and fiber orientation $\boldsymbol{\omega}$ - can be updated with the Jacobian and the incremental deformation tensor in each iteration:

$$\varphi_\mathrm{u} = \delta J^{-1}\varphi\,, \tag{4.25}$$

$$\boldsymbol{\omega}_\mathrm{u} = \delta\mathbf{F}^{-1} \cdot \boldsymbol{\omega} \cdot \delta\mathbf{F}^{-\top}\,. \tag{4.26}$$

Because the values are updated in each time increment, the incremental deformation gradient and Jacobian are used here. With the new fabric properties, the Lamé parameters and the permeability are updated in each iteration with user-defined functions. After convergence, the total stress is calculated by adding the stress increment to the total stress of the previous time step:

$$\mathbf{S}^{(t+\mathrm{d}t)} = \delta\mathbf{S}^{(t+\mathrm{d}t)} + \mathbf{S}^{(t)}\,. \tag{4.27}$$

The same procedure is used to calculate the total Green-Lagrange strain $\mathbf{E}$ and the total displacement field $\mathbf{d}$.
The total accumulated stress and strain tensors are then calculated by transforming the second Piola-Kirchhoff stress $\mathbf{S}$ and the Green-Lagrange Strain $\mathbf{E}$ from the reference configuration to the new deformed configuration:

$$\mathbf{S}_{\mathrm{u}} = \delta J^{-1} \left(\delta \mathbf{F}^{\top} \cdot \mathbf{S} \cdot \delta \mathbf{F} \right) , \tag{4.28}$$

$$\mathbf{E}_{\mathrm{u}} = \delta \mathbf{F}^{-1} \cdot \mathbf{E} \cdot \left(\delta \mathbf{F}^{-1} \right)^{\top} . \tag{4.29}$$

In the next time-step, this updated configuration becomes the new reference configuration.
The solution algorithm for the updated Lagrangian incremental poro-elasticity based on Terzaghi's law is summarized in the scheme shown in Fig. 4.1.
In contrast to FE-based methods, the implementation of traction boundaries is not that straightforward in FV solid mechanics. Instead of directly applying forces onto nodes like in FE, a Neumann-type boundary is used, where the incremental displacement gradient on the boundary is evaluated [133].

4.2.5 Verification

To verify the implemented FV poro-elasticity algorithm, a verification case by Dereims et al. [123] is used. The case consists of a two-dimensional plate with two types of loads applied. A pressure acts as an external vertical load onto the porous solid, which leads to a unidirectional compression. This is superimposed by an internal pressure field containing a constant pressure gradient acting against the external pressure, which leads to a bending of the plate. The verification setup is shown in Fig. 4.2 and the geometric, material and boundary parameters are summarized in Tab. 4.1. The mesh consists of 200 and 100 cells in horizontal and vertical direction, respectively. The analytical

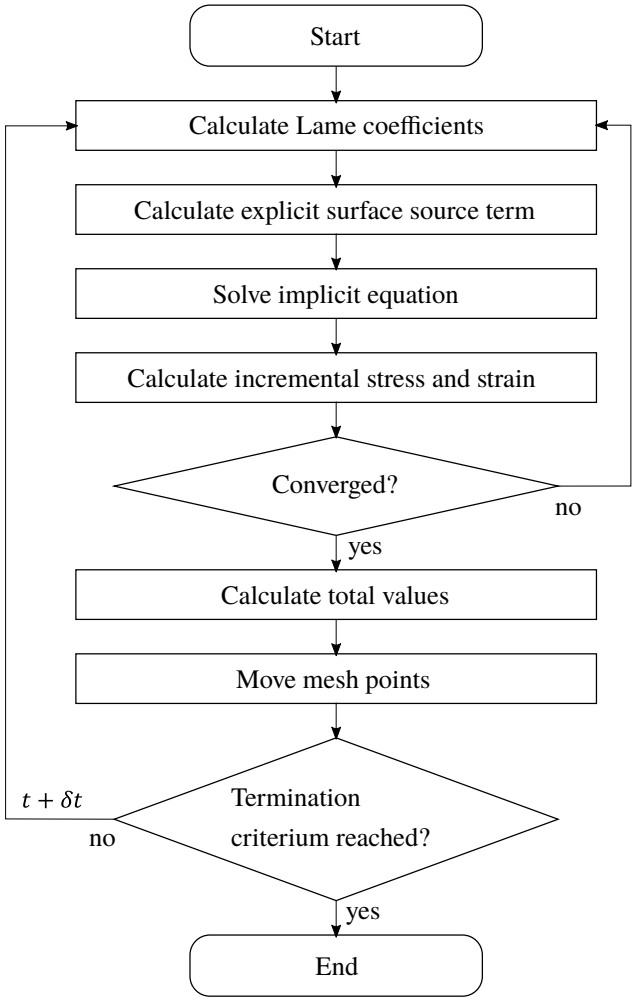

Figure 4.1: Non-linear poro-elasticity solution algorithm for a deformable porous medium using an incremental Lagrangian approach

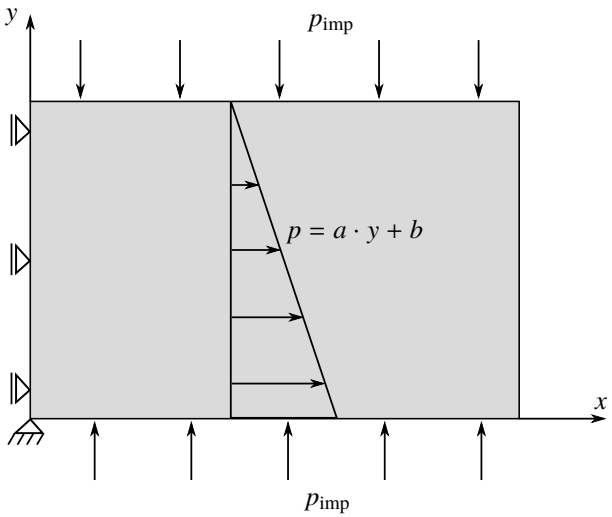

Figure 4.2: Schematic model of the poro-elasticity verification case defined by Dereims et al. [123]

solution of this case is derived in detail in [123] by using Airy functions. The resulting analytical displacement field **d** is given by:

$$
\begin{aligned}
d_x(x,y) &= \frac{1+\nu}{E}\left[(1-2\nu)\,(ay+b)\,x + \nu G x\right] \\
d_y(x,y) &= \frac{1+\nu}{E}\left[(1-2\nu)\left(\frac{a}{2}y+b\right)y + (\nu-1)\,Gy - \frac{1-2\nu}{2}ax^2\right] \\
G &= aH + b + p_{\text{imp}}\,.
\end{aligned}
\tag{4.30}
$$

With this displacement field, the outline of the deformed rectangle is calculated and compared to the FV solution using the method described in the previous section.

Fig. 4.3 shows the magnitude of the displacement field of the FV simulation. The outline of the deformed rectangle shows a very good agreement to the

Table 4.1: Boundary and material parameters for the poro-elasticity verification case

Parameter	Value	Description
H	0.02 m	initial height
L	0.04 m	initial length
p_{imp}	0.1 bar	surface pressure
a	$-5\,\text{bar}\,\text{m}^{-1}$	pressure function parameter
b	0.1 bar	pressure function parameter
E	266 kPa	Young's modulus
ν	0.3	Poisson's ratio

analytical solution whose outline is indicated by pink dots. Furthermore, the tip displacement of the simulation is compared to the analytical value by calculating the relative error components:

$$\begin{aligned} e_x &= \frac{d_{x,\text{simulation}} - d_{x,\text{analytical}}}{d_{x,\text{analytical}}}, \\ e_y &= \frac{d_{y,\text{simulation}} - d_{y,\text{analytical}}}{d_{y,\text{analytical}}}. \end{aligned} \tag{4.31}$$

Figure 4.4 shows both error values over the explicit iterations. Both error components decrease to zero and both values are below 1% at the end of the simulation that is stopped after 452 iterations when a residuum below $1 \cdot 10^{-6}$ is reached.

The agreement of the solutions verifies the poro-elasticity simulation method and the solution algorithm. Both, external and internal loads are used in this verification example to verify the correct implementation of the equations, the boundaries, and the effective stress split using Terzaghi's law.

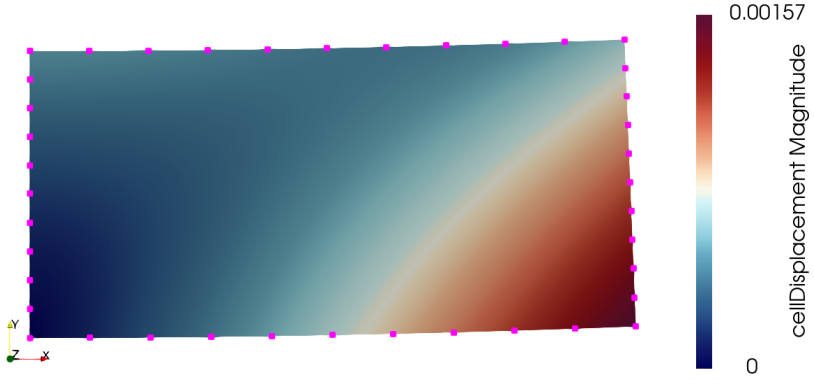

Figure 4.3: Total displacement magnitude field of the poro-elasticity algorithm verification case simulated using the developed method; pink dots indicate the outline of the analytical solution

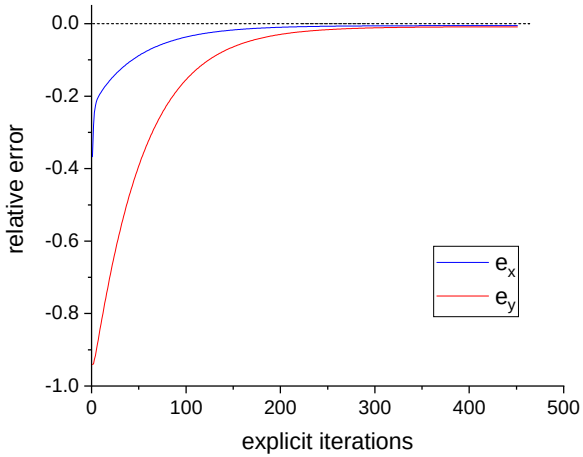

Figure 4.4: Simulation error of the lower right tip displacement compared to the analytical value over the explicit iterations

4.3 Internal coupling of fluid flow and porous solid mechanics

Before the injection of the liquid resin starts the mold-filling step in RTM, the preform is placed inside the cavity and gets compressed to its final thickness. This compression step can be modeled as a conventional solid mechanics problem on a macro-scale. When mold-filling starts, the fluid pressure inside the fabric increases and thus changes the total stress inside the fabric. When additionally a foam core is put between the layers to manufacture a sandwich component, the compacted fabric, as well as the fluid pressure, induce a force onto the foam core. This force is, thus, dependent on the stress inside the farbic and also on the fluid pressure, which both depend on the deformation state of the fabric. The compaction reaction force of the fabric directly depends on the compaction strain, the fluid pressure in turn depends on the permeability and hence on FVF, which is proportional to the volumetric strain. To model these dependencies, a coupled solution algorithm is necessary. Therefore, the porous solid mechanics' solution algorithm introduced in Section 4.2 is coupled inside the FV approach to the RTM mold-filling algorithm explained in Section 3.2. This coupling is referred to as "internal coupling" as it happens inside the cavity and, furthermore, it is implemented inside one solution environment using a monolithic approach.

4.3.1 Solution procedure

To couple mold-filling to poro-elasticity mechanics, the solution algorithms of C-RTM (Fig. 3.4) and of the porous solid mechanics (Fig. 4.1) are combined using one simulation domain. In a monolithic approach, no mapping is necessary as both parts use the same discretized simulation domain. In a partitioned approach, the coupling would lead to a volumetric exchange and mapping of the pressure and the displacement inside the whole cavity. This is avoided in

this method because a high numerical effort for a volumetric mapping step is expected. The combined, monolithic solution algorithm scheme is shown in Fig. 4.5.

First, the poro-elasticity part is solved using the iteration loop shown in Fig. 4.1. When the poro-elasticity part is converged, the total stress and strain values are updated with the incremental values and the mesh is moved using the displacement field. After the mesh motion, the fluid part is solved for pressure and velocity with the updated local permeability in each cell. As a strong coupling is present between the poro-elasticity and the fluid flow, a further outer loop is implemented over both parts until a common solution is found.

4.3.2 Verification

The solution algorithm is verified using a steady-state one-dimensional case suggested by MacMinn et al. [143]. The focus of this verification is on the non-linear large strain solutions and their comparison to a linear small strain assumption. In the verification case, a porous solid is compressed due to a fluid flowing through it. Figure 4.6 shows this verification case for a flow-induced compression. There are three non-linearities combined in this case that influence the solution: geometric non-linearity, a non-constant permeability, and a non-constant Young's modulus of the porous material. The geometric non-linearity is treated as explained in Section 4.2.2, whereas the material non-linearities depend on the FVF φ. The Young's modulus of the porous solid is given by a linear function of the FVF, interpolated from two moduli $E_{\varphi=0.5}$ and $E_{\varphi=1}$. The non-constant permeability in flow direction is given by a Gebart-type equation (Eq. (3.20)) also depending on the FVF. For the linear cases, Young's modulus and permeability are held constant at the initial values belonging to $\varphi = 0.5$. The length L of the porous medium before compression is 1 m and the mesh consists of 200 cells in the flow direction. The geometric, material and flow parameters are summarized in Tab. 4.2.

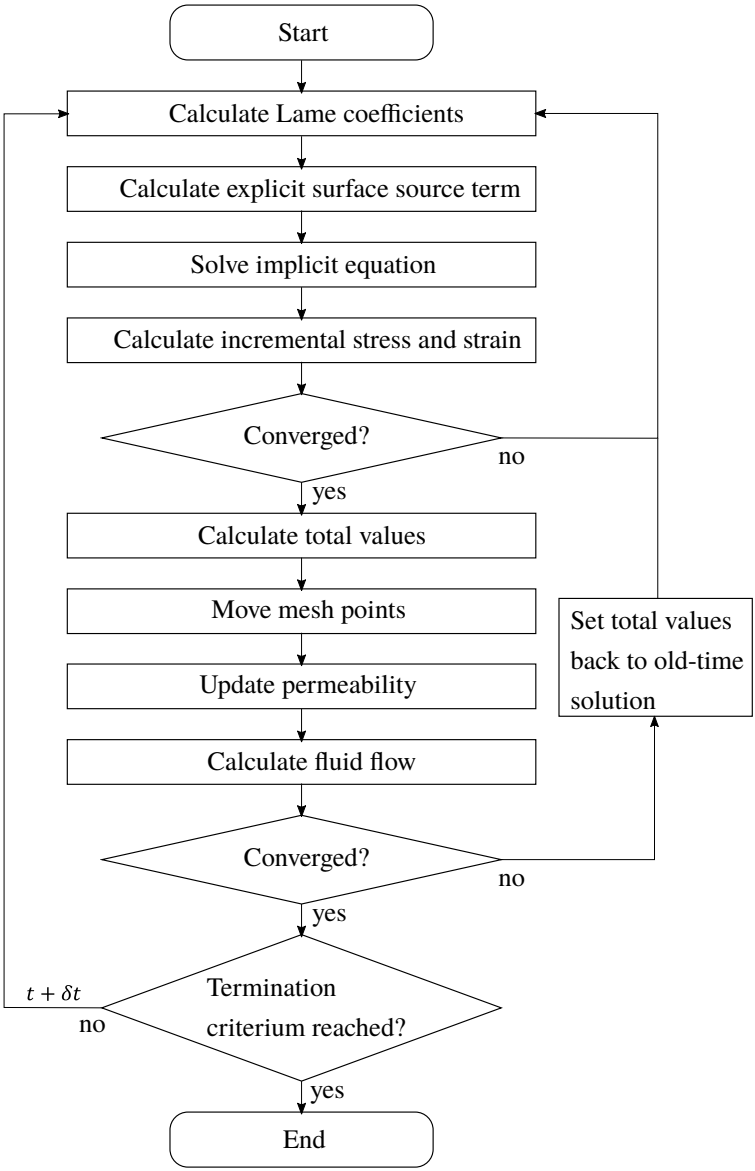

Figure 4.5: Internal coupling solution algorithm to model fluid flow within a deformable porous medium; the algorithm is a combination of the fluid flow in a non-constant cavity (Fig. 3.4) and the poro-elasticity algorithm (Fig. 4.1)

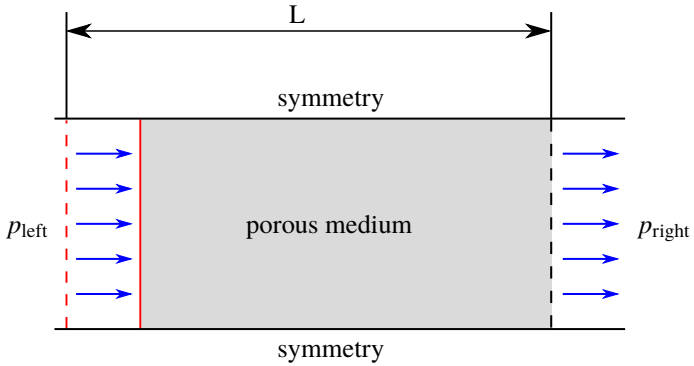

Figure 4.6: Schematic model of the internal coupling verification case defined by MacMinn et al. [143] for large-strain porous medium deformation induced by a fluid flow

Table 4.2: Process and material parameters of the internal coupling verification case

Parameter	Value	Description
L	1 m	initial length
p_{left}	6 bar	inlet fluid pressure
p_{right}	1 bar	outlet fluid pressure
$E_{\varphi=0.5}$	1 MPa	(initial) Young's modulus
$E_{\varphi=1}$	10 MPa	Young's modulus at $\varphi = 1$ (non-linear case)
ν	0.0	Poisson's ratio
φ_0	0.5	initial FVF
K_0	1×10^{-10} m^2	(initial) permeability
A_{Gebart}	2×10^{-10} m^2	Gebart model parameter

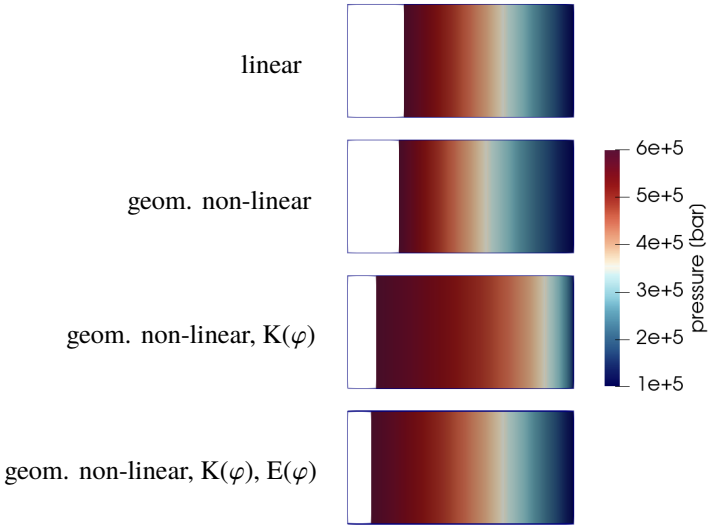

Figure 4.7: Simulation results of the deformed geometry of the internal coupling verification case showing one linear and three non-linear models; the color scale shows the fluid pressure inside the porous medium

Figure 4.7 shows the deformed state of the porous medium and the colors indicate the fluid pressure field inside of it. Four different cases are compared in this verification study. The first case is the purely linear case, the second is the case with only geometric non-linearity. In the third case, a non-constant permeability is added and the fourth case includes all three non-linearities by furthermore adding the non-constant Young's modulus. Obviously, the non-linearities influence strongly the displacement as well as the pressure field. The linear model results in the highest displacement, whereas the model including all non-linearities shows the lowest displacement.

This behavior is explained by further analyzing the distribution of displacement, strain, pressure and FVF along the deformed porous medium. For a better comparison, the values are normalized as follows:

$$\begin{aligned} x^* &= \frac{x - d}{L}, \\ \mathbf{S}^* &= \frac{\mathbf{S}}{E_{\varphi=0.5}}, \\ d^* &= \frac{d}{L}, \\ p^* &= \frac{p}{E_{\varphi=0.5}}. \end{aligned} \tag{4.32}$$

Figure 4.8 compares the normalized values. As expected in the linear case, the pressure shows a linear distribution on the deformed coordinates, whereas it is non-linear for all other cases. It should be noted here, that the strain plotted in the linear case is the Green-Lagrange strain to better compare it to the non-linear cases, whereas the calculation of the FVF and the resin pressure is carried out using the linear strain. A very strong influence on the results is seen when adding the non-constant permeability function. It changes drastically the pressure gradient and in the following the pressure distribution, which results in a strong non-linear FVF and strain along the flow direction. Finally, when adding the non-constant Young's modulus, again a significant change especially for strain, pressure, and FVF is observed. Due to the higher stiffness, the strain magnitude and the overall non-linearity of the solution decrease. The increasing Young's modulus acts against the non-linearity of the permeability and thus results in a decreasing non-linear FVF and pressure.

Figure 4.9 shows the stress distributions for the verification cases. The stresses are divided into Terzaghi's effective stress supported by the porous solid and the fluid stress that has the magnitude of the negative fluid pressure. They add up to the total stress inside the porous medium that is constant in this verification case. At the right edge, the load is fully supported by the solid skeleton, whereas on the left edge only the fluid pressure supports the load.

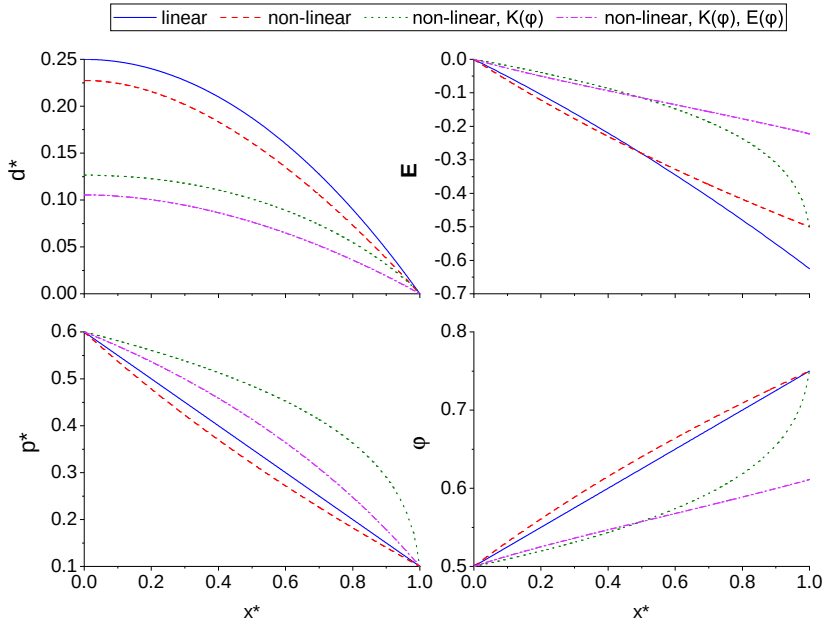

Figure 4.8: Displacement, Green-Lagrange strain, pressure, and FVF (from top left to bottom right) along the deformed state of the porous solid showing the results of the four analyzed internal coupling verification cases

The solutions show an exact agreement with the results by MacMinn et al. [143]. Furthermore, it is shown here that the material non-linearity of the porous solid also strongly influences the result, which was not investigated by the authors. However, this is important for the modeling of the compression of a fabric, which has a strongly non-linear compaction stiffness (cf. Section 5.5). With this method derived here, the mold-filling inside a deformable porous medium can be modeled, which is shown in an application example in Section 6.2.

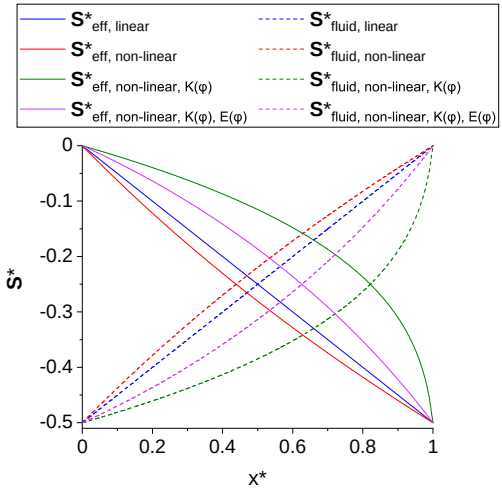

Figure 4.9: Normalized second Piola-Kirchhoff stresses along the deformed state of the porous solid showing the results of the four analyzed internal coupling verification cases

4.4 External coupling for FSI

To model the RTM mold-filling with an embedded foam core, additionally to the method for modeling the flow-induced deformation of a porous medium given in the previous section, a method to capture the interaction between the poro-elasticity with internal fluid flow and the foam core mechanics is needed. A partitioned approach is used to solve this FSI problem, which needs special algorithms and solution procedures that are explained in this section. The partitioned approach is chosen because of the clearly defined interface between the components on the surface of the foam core. This is a very common case for FSI and thus various mapping and solution procedure algorithms exist to minimize the numerical error and effort.

The partitioned approach is implemented using the FSI interface library preCICE [144]. PreCICE was developed to enable a black-box coupling of multiple

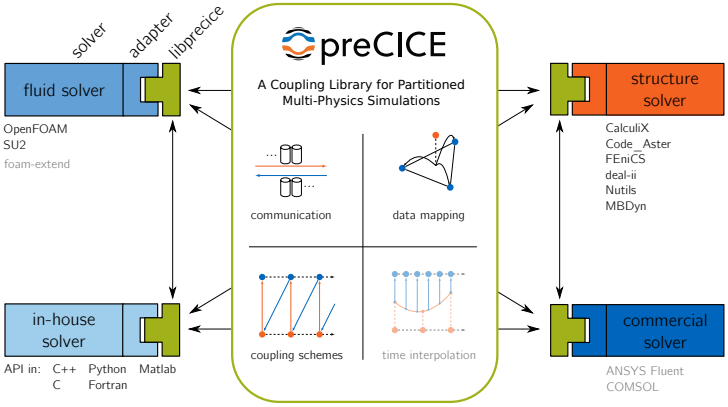

Figure 4.10: Schematic overview of the preCICE coupling library for FSI [145]

partners and to guarantee high parallel scalability up to computations on high-performance clusters (HPC). The main idea is that it uses a library approach instead of a framework approach, which means that the coupling partners call the preCICE interface. PreCICE itself manages the whole coupling environment, which includes mapping, data exchange, time-stepping, and solution control. The preCICE scheme is visualized in Fig. 4.10. To couple a partner to the interface, specific adapters for each software are needed. Inside the adapters, the data that is exchanged is collected from the coupling partner, formatted to conform to the preCICE data standard, and sent to or received from the preCICE interface, respectively.

PreCICE allows the user to choose an implicit or explicit coupling scheme. In explicit coupling, the data at the interface is exchanged at defined time-steps, but no common solution of the participants is searched. In contrary to that, in the implicit coupling scheme iterations over one time-step for all participants are carried out until a common solution is found. Implicit coupling is necessary for strongly coupled problems, where an explicit coupling might not find a converging solution.

4.4.1 FSI model for mold-filling in RTM with embedded foam core[2]

The coupling data in FSI consists usually of forces and displacements. The fluid partner exerts a force onto the solid partner, which consists of tangential forces due to viscous shearing of the fluid at the interface and normal forces consisting of the total pressure acting on the solid. These forces are used as a boundary condition for the solid partner that calculates the solid stresses, strains and displacements resulting from these external forces. Subsequently, the solid displacements are sent back to the fluid part and is then used as a boundary condition for a mesh motion solver in the domain of the fluid partner.
In RTM mold-filling with sandwich core, the forces onto the embedded foam core (the solid part) contain the reaction force of the compressed fabric additional to the fluid pressure (the fluid part). This coupling scheme during RTM mold-filling is shown in Fig. 4.11. In the dry part of the cavity, only the force of the fabric F_{fabric} is present at the fluid-solid interface. In the infiltrated part, the force of the resin F_{resin} increases the total force acting on the foam core [140, 146].
The compression of the foam core leads to a decreasing FVF and following to a higher permeability. Because of the strong dependency of permeability on FVF and thus on the fluid pressure and the foam core deformation inside the cavity, the model has the properties of a strongly coupled problem. For this reason, an implicit coupling between the participants is used. Each time-step is repeated until a common solution is found. PreCICE allows to use several implicit coupling acceleration schemes and to set the desired coupling residuals individually for each exchanged data [144]. Furthermore, several mapping methods for the coupled data exist like e.g. nearest neighbor, nearest projection, or radial basis function (RBF) mapping types. The preCICE coupling scheme

[2] Parts of this section are based on [140]

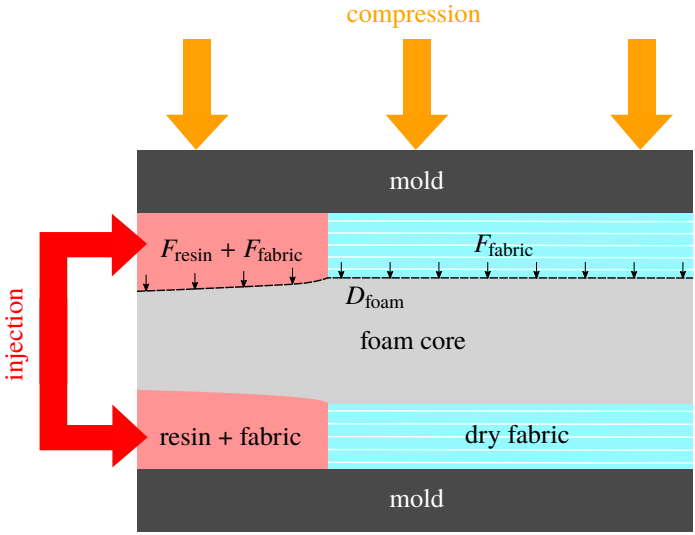

Figure 4.11: Simulation scheme for RTM mold-filling with embedded foam core coupling forces F and displacements D between the resin flow with preform compaction and the foam core

for RTM with a deformable sandwich core involving the mold-filling and fabric deformation part (blue) and the foam core part (orange) is shown in Fig. 4.12. The force at the interface for an element face f is calculated using the total stress definition of Eq. (4.1):

$$F_f = \sigma_{\text{total},f} \cdot \mathbf{n}_f A_f, \tag{4.33}$$

with the face normal vector $\mathbf{n}_f$ and the face area A_f. The total stress already contains the fluid pressure as well as the effective fabric stress. The fabric deformation is solved in an incremental fashion (see Section 4.2), hence the best way is to also exchange incremental displacements at the interface from the solid to the fluid part. The foam core part is simulated using the open-source FE software CalculiX [147], where already a preCICE-CalculiX adapter

Figure 4.12: FSI coupling scheme to model sandwich manufacturing in RTM; the scheme consists of the internal coupling algorithm (Fig. 4.5) as the fluid part (blue) and the foam core solid mechanics (orange)

exists [148]. In the adapter, it is also possible to communicate incremental displacements to the interface so that it can be used with the incremental displacements formulation of the poro-elasticity algorithm.

4.4.2 Verification

A simplified verification case is used to test the FSI method. It is designed to be comparable to real RTM mold-filling of a sandwich part and thus consists of the coupling partners introduced in the section before. To compare it to an analytical solution, it uses a one-dimensional flow and a simple linear elastic foam core material model. Material non-linearities are included in the material model and the permeability model of the fabric. For the permeability, a Gebart-type equation (Eq. (3.20)) with the parameters K_0 and A is used. The fabric compression modulus is a linear interpolation between two values at $\varphi = 0.25$ and $\varphi = 0.5$. Figure 4.13 shows the schematic model of the verification case. It consists of two steps. The first step is the compression of the dry fabric and the foam core. The second step is the injection of the resin with a constant velocity. The mold is assumed to be rigid and, therefore, is only modeled as a boundary condition with zero displacements. The geometry and process parameters of the verification case are summarized in Table 4.3.
The mesh of the FSI simulation consists of 101 cells in the flow direction and two cells in the vertical direction for the cavity and fabric, which is sufficient for this simplified case, as only the in-plane flow without wall drag is modeled.

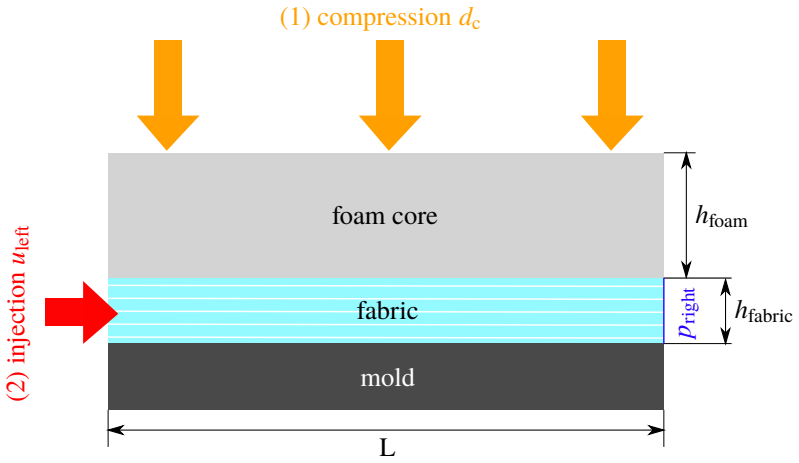

Figure 4.13: External coupling verification case with two simulation steps: (1) compression of the foam core and the fabric; (2) resin injection with a constant flow rate

The elastic foam part consists of 100 cells in the flow direction and 5 cells in the vertical direction, respectively. Due to the different element numbers in the flow direction, a mapping between non-conforming meshes has to be carried out, which is carried out by using RBF.

To accelerate the implicit coupling, a quasi-Newton scheme is used that was developed by Degroote et al. [149] (interface quasi-Newton inverse least-squares (IQN-ILS)), which showed faster convergence of the implicit iterations compared to other schemes like Aitken under-relaxation [150] or generalized minimal residual (GMRES) methods [151, 152]. The FSI coupling parameters are summarized in Tab. 4.4.

In Fig. 4.14, the simulation results at four different time-steps are visualized. The solid is shown in grey color, whereas the dry fabric is in blue and the resin is shown in red color. The first time-step at $t = 0\,s$ shows the initial (undeformed) state of the solid and fabric. At $t = 0.5\,s$, the fabric is already compressed because of the initial displacement of the top face of the foam core $d_{c,0}$ that models step (1) of Fig. 4.13. The third time-step shown at $t = 6\,s$, shows the

Table 4.3: Process, geometry and material parameters for the external coupling verification case

Parameter	Value	Description
L	0.2 m	flow length
$d_{c,0}$	0.002 m	initial compression displacement
u_{left}	0.01 m s^{-1}	inlet flow velocity
p_{right}	1 bar	outlet pressure
μ_{resin}	1 Pas	dynamic resin viscosity
$E_{fabric,\varphi=0.25}$	1 MPa	initial Young's modulus at $\varphi = 0.25$
$E_{fabric,\varphi=0.5}$	10 MPa	Young's modulus at $\varphi = 0.5$
$h_{fabric,0}$	0.004 m	initial fabric height
$\varphi_{fabric,0}$	0.25	initial FVF
K_0	1×10^{-10} m^2	Gebart model parameter
A	2×10^{-10} m^2	Gebart model parameter
E_{foam}	10 MPa	Young's modulus of the foam core
$\nu_{fabric,foam}$	0.0	Poisson's ratio of fabric and foam core
$h_{foam,0}$	0.02 m	initial foam height

mold-filling at a half-filled cavity. The resin infiltrates the fabric from left to right, which results in increased pressure and thus leads to decompression of the fabric and further compression of the foam core. At $t = 13\,s$, the cavity is fully filled. As long as the fluid is flowing, the cavity height is not constant along the flow path but depends on the pressure inside the cavity and thus is larger at the inlet than at the outlet.

The case is analytically solved for the stationary case when the cavity is fully filled with resin. The analytical solution of Darcy's law in the cavity combined with the elastic behavior of the fabric and the foam core with linearized strain is given in Appendix B.

Figure 4.15 shows the result of the pressure and the FVF for the analytical solution as well as the FSI simulation at the time when the cavity is fully filled.

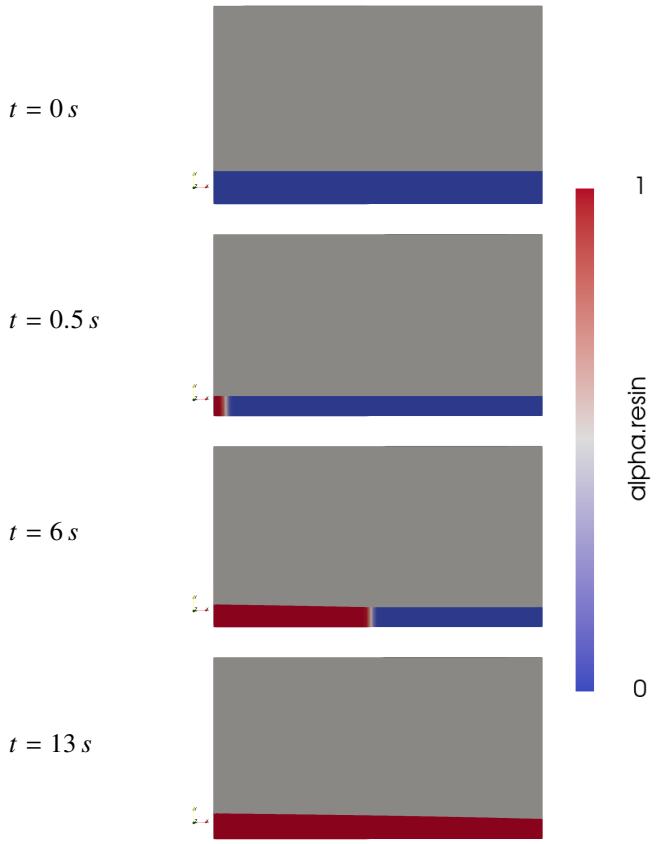

Figure 4.14: Mold-filling simulation results of the external coupling verification case at four time-steps showing the fabric compression and the subsequent mold-filling; the length is scaled with a factor of 0.2

Table 4.4: Coupling methods and parameters of the FSI verification case; details of the methods are given in [144]

Parameter	Method / Value
time-step	0.05 s
mapping method	RBF thin plate splines
coupling scheme	serial implicit
maximum iterations	50
implicit acceleration scheme	IQN-ILS
initial relaxation	0.01
preconditioner	residual-sum, QR1 filter, 1×10^{-7}
time-steps reused	5
displacement convergence residuum	1×10^{-7} m (abs.)
force convergence residuum	1×10^{-5} (rel.)

In the simulation, a pressure of 5.4 bar is reached at the inlet position, where the FVF is approximately 32%. The pressure decreases non-linearly with the flow to the outlet pressure of 1 bar. The FVF increases to a maximum value of 40.8% at the outlet. The analytical solution shows the same characteristic of non-linearly increasing FVF and decreasing pressure. The maximum and minimum values differ slightly compared to the simulations. This difference can be explained by the assumption of the solids to behave like linear one-dimensional springs in the analytical solution and the geometrical non-linearity of the solid and the porous medium mechanics in the simulation. Furthermore, the force is acting on the foam material in the normal and tangential direction, whereas in the analytical model, the force is limited to a vertical component.
Figure 4.16 shows the results of the FSI verification case compared to a mold-filling simulation assuming a rigid foam. The graph compares the pressure distribution along the flow path. Two states are visualized: 50% and 100% fill degree. As can be seen from the comparison of the pressure distribution, the

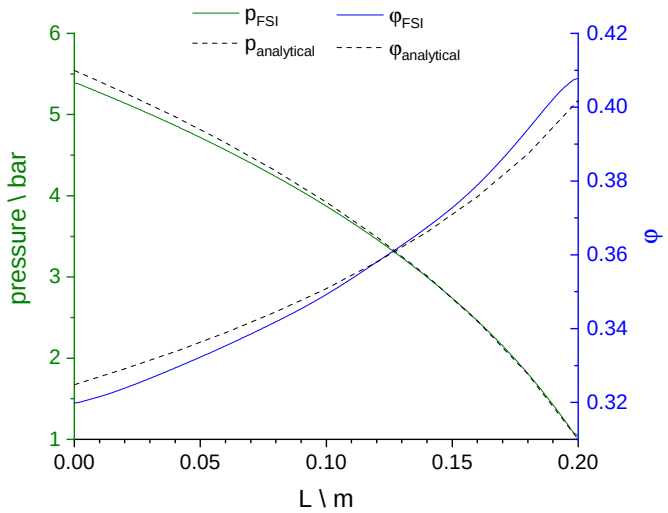

Figure 4.15: Results of the FSI verification case; comparison of pressure and FVF along the flow path for the simulation and the analytical solution

presence of a deformable material strongly influences the mold filling. When a constant flow rate at the injection gate is set, the pressure inside the cavity reaches higher values for an assumed rigid mold.

At the end of the mold-filling, the pressure reaches 21 bar compared to 5.4 bar for the FSI simulation. Furthermore, the deformation influences the mold filling time even at the same pressure because of the larger volume that has to be filled by the resin. In the verification case here, the mold-filling time is 10 s for the rigid case compared to 13 s for the FSI case.

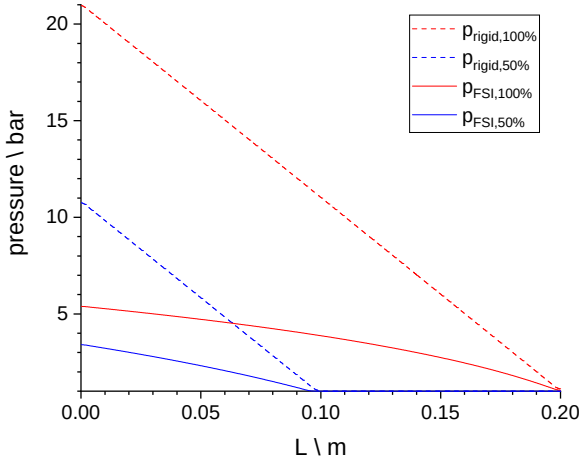

Figure 4.16: Results of the external FSI verification case; comparison of pressure along the flow path for the FSI simulation and the simulation with a rigid foam core at a half-filled and a fully filled cavity

4.5 Discussion

In this chapter, a poro-elasticity solid mechanics method using FV discretization for large strains is presented. The aim of this method is to model the fabric deformation behavior during mold-filling. The approach, therefore, uses an incremental, updated formulation to account for large strains that can occur. Combining the RTM mold-filling algorithm for non-constant cavities presented in Chapter 3 with the poro-elasticity algorithm presented in this chapter enables a simulation of mold-filling inside a deformable porous medium. The method is verified by two verification cases and shows for both cases an excellent agreement to analytical solutions.

The modeling of resin flow inside a compressible porous medium is necessary for many applications in the context of composites manufacturing, like VARI with including preform compression, rotational molding with compression due to fluid pressure and centrifugal forces, or PC-RTM considering the initial

preform compression, which is also shown as an application example in Section 6.1.

Furthermore, an FSI model to simulate mold-filling of a sandwich part is presented and verified. The simulation result shows a very good agreement to the analytical solution for a simplified one-dimensional case. The influence of the foam core onto the pressure level is significant in the verification case. This behavior was also reported by Gerstenkorn [56] and is also expected when simulating the mold-filling of RTM sandwich parts, where furthermore the mold-filling is expected to become inhomogeneous because of local deformation of the foam material. In Section 6.3, the influence of an embedded foam core on mold-filling is analyzed by simulations, and furthermore, the method is validated by experiments.

Regarding the fabric material, only the compression behavior is of interest for the RTM applications analyzed in this work. The in-plane behavior can be added to the model to enable the prediction of the formation of resin channels at edges having a small radius or at the edges between two areas with different part thicknesses. At these edges, tensile stress inside the fabric leads to further compression of the preform and, thus, resin-rich areas are created along the edges that influence the mold-filling. For modeling the in-plane behavior of the fabric, an anisotropic constitutive model is needed. This can be added to the method by combining it with the orthotropic FV solver proposed by Cardiff [136]. Furthermore, adding contact boundary conditions [135] to model the friction between fabric and mold or foam core surface enables e.g. the modeling of fabric shifting or fiber washing in the flow direction, which can occur for low FVF and high injection flow rates.

5 Material Characterization and Modeling

The characterization and modeling of the material properties is an important part of process simulations. The materials not only influence the process but also set the boundaries by defining the process limits. For accurate simulations, it is crucial to have valid material data. However, the experimental characterization can be an exhaustive task, when different materials or a large range of processing conditions is simulated. The characterization, therefore, has to match the process conditions that the simulations should cover. Yet, those conditions are not always known beforehand (e.g. cavity pressure), which makes it difficult to decide in which range or in which detail the materials need to be characterized.

After a short introduction and a review of the related work, the setups and results of experimental characterizations of the resins systems, the fabrics and the polymer foams that are also used in the application examples and validations (Chapter 6) are presented. The results of the resin viscosity characterization, carried out in recent studies [18, 43], are presented for three different epoxy resin systems. The permeability and the compression behavior of three fabrics are characterized using state-of-the-art methods and used to fit non-linear material models to the experimental results. The characterization of the polymer foam core stiffness under compression loads is carried out using a combination of uniaxial and hydrostatic tests at elevated temperatures and for three foam core

densities. The results are used to model the anisotropic behavior and, furthermore, to reveal the dependency of the material parameters on the processing temperature and density.

5.1 Introduction and review of related work

All experimental permeability measurement setups use the same principle for evaluating the in-plane permeability. A fluid that has a constant viscosity is injected into a cavity with a preplaced fabric. During the infiltration of the fabric, either the flow front progression or the injection pressure is measured, while the other parameter is held constant. By assuming that Darcy's law is valid within the cavity, the permeability can be calculated with the known pressure gradient, the resin velocity, and the resin viscosity using Eq. (3.1).
Although a lot of research was made to develop measurement methods for various kinds of fabrics, it is still difficult to obtain reproducible and robust permeability data. In the last decade, a lot of effort was put into benchmarking present measurement methods and setups to make the high amount of data more comparable. Three benchmark studies were published to compare the published methods. In the first study by Arbter et al. [89], the aim was to formulate "good practice" guidelines, as the results showed a scatter of the permeability values for equal fabrics of up to one order of magnitude. The second benchmark focused on getting comparable results by strict measurement guidelines [90] and the scatter indeed decreased to 25% in the third study [91]. While this was a promising result, it also showed the strong influence of the measurement conditions and parameters on the measured permeability.
Because of this influence of processing conditions onto the measured permeability, which is not understood in detail yet, Magagnato et al. [153] use a measurement method that is as close as possible to the real RTM process. While the benchmark participants focused on using transparent molds and optically measuring the flow front velocity for a given pressure, Magagnato et al. use

a rigid steel tool with embedded pressure sensors to measure the pressure and flow front progression inside the cavity. In contrast to optical measurements, where a deformation of the transparent tool can be present during measurement, the rigid steel tool ensures that the FVF is constant inside the entire mold. This setup is also used for permeability characterization in this work.

In most of the RTM applications, the thickness of the parts is very small compared to its other length scales. This leads to a common assumption that the resin flow in the thickness direction of the fabric can be neglected. However, when manufacturing thick parts like wind turbine blades or laminated springs, it can be important to model the through-thickness flow, which then signifies that the permeability in the thickness direction is relevant. Because it is hardly possible to track a flow front in the thickness direction, for permeability characterization a saturated measurement device is used, where a constant mass flow is set and the pressure drop in the thickness direction is measured [154].

Before resin injection starts, the mold is closed and the dry fabric is compressed to achieve a high FVF. The fabric compaction force is one part influencing the necessary press force besides the fluid pressure and the sealing compaction force [31]. Furthermore, knowledge of the fabric compaction behavior is necessary to predict the FVF in VARI [155, 156]. Additional to the strong non-linear compaction behavior present in all fabrics, the number of layers, the binder type, and fluid saturation influences the compaction, as was observed in the literature [157–160]. This leads to visco-elastic and elastic-plastic descriptions of the compaction that is especially important when using the data for VARI process simulations, where the mold-filling is rather slow. In this work, the fabric compaction is modeled focusing on the strong non-linearity using a function of Young's modulus depending on the FVF (cf. Section 4.2.3).

The dynamic viscosity of the polymer resin is also directly influencing the mold-filing (cf. Section 3.3.2). In previous applications, it was assumed that during infiltration, the resin does not start to cure, as the time for mold-filling is relatively small compared to the curing time. This changes, when the aim is to minimize cycle time. For faster curing, the temperature needs to be

higher, which also signifies an earlier increase in viscosity, which can affect mold-filling. To measure the viscosity depending on temperature and cure degree, two techniques are used. First, DSC measurements (non-isothermal and isothermal) to define the cure degree depending on temperature and time, and secondly, rheological measurements to define the viscosity depending on temperature and cure degree. With these measurements, kinetic and rheological models are fitted. The fitting and the model choice can affect the accuracy of the viscosity characterization significantly, which was shown by Bernath [42, 43]. Furthermore, it is difficult to measure viscosity at high temperatures, because the curing starts directly at the moment when the resin is mixed but the measurement normally needs a small preparation time to be started. For this reason, Bernath developed a measurement method to increase the accuracy of viscosity characterization for fast resin systems and high temperatures [108]. In this work, the resin systems used in the application examples were already characterized [18, 43] and the available rheological and kinetic model data of the three epoxy systems is presented.

In general, the deformation behavior of polymer foam materials under compression loads can be divided into three major stages that are visualized in Fig. 5.1 [161]. Stage I is characterized as a linear-elastic behavior, which is followed by a large range of elastic-plastic behavior at nearly constant stress (elastic-plastic plateau, Stage II). Stage III is the following densification of the foam material, which shows a non-linear behavior with increasing modulus. Many researchers focused on the mechanical modeling of these hyper-elastic materials and proposed different material models like Mooney, Rivlin, or Ogden [162–164].

Starting from the contact of the heated tool to the fiber reinforcement, the temperature in the foam core rises from ambient temperature to mold temperature. Like its polymer base material, also the foamed polymer's mechanical material parameters depend on the temperature. Al-Hamdan et al. [15] and Gerstenkorn et al. [17, 56] showed in their work the strong temperature-dependency for different foam materials like PUR, PVC, and PMI.

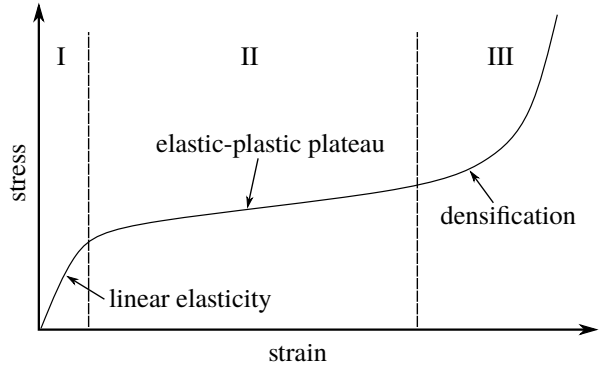

Figure 5.1: Idealized stress-strain-relationship of polymer foams under compression load

Furthermore, an anisotropic behavior of the polymer foam originates from the manufacturing process. When a foam extrusion process is used, the foam cells have a preferred direction, which results in an orthotropic or transverse isotropic material behavior with a higher stiffness in the thickness direction of the produced foam plates.
In this thesis, the characterizations of the fabrics are carried out using state-of-the-art methods, whereas the polymer foam core is characterized by combining uniaxial compression tests with hydrostatic tests in a pressure chamber.

5.2 Characterized Materials

Three epoxy resin systems that were designed specifically for LCM are used in the application examples. The systems are referred to as "R1", "R2", and "R3". R1 is a fast curing resin system (the system name cannot be published due to a non-disclosure agreement). The second resin system R2 is a slower resin (Sika® Biresin® CR170/CH150-3). The third resin system (R3) used in the application examples is the fast resin system Araldite® LY 3031 by Huntsman.

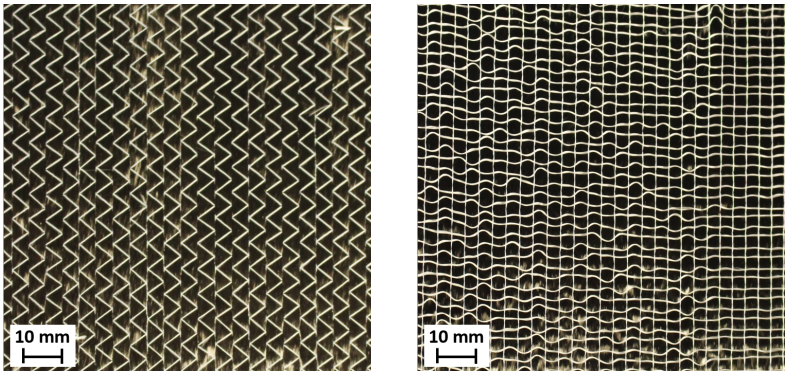

a) b)

Figure 5.2: a) Top view and b) bottom view of the UD carbon fiber fabric

Three fabric materials are characterized regarding permeability and compaction. The first is a UD glass fiber fabric (Saertex, 1200 g m^{-2}) with a layup of (0° | 90° |0°). Furthermore, two carbon fiber fabrics, one bidirectional fabric (Zoltek, 300 g m^{-2}) with a quasi-symmetrical layup of (0° | 90° | 0° | 90°)$_{sym}$, and one UD fabric (Zoltek, 333 g m^{-2} [165]), with uniaxial layup are characterized. The fiber orientation angles refer to the flow direction, which signifies that a 0° orientation is parallel and a 90° orientation is transverse to the main resin flow during processing or measurement.

The UD carbon fiber fabric is shown in Fig. 5.2. Besides the carbon fiber rovings, it also consists of glass and polymer stitching yarns to form the fabric. In the top view, the characteristic zig-zag stitching pattern is visible.

A polymer foam core material that has relevant deformations at pressures of up to 10 bar is required for the validation of the FSI method. Therefore, the PET foam material Airex® T92 by 3AComposites is chosen [58]. Three different densities of the material are characterized regarding their compression behavior: 80 g L^{-1}, 100 g L^{-1} and 130 g L^{-1}.

Table 5.1: Parameters of the Castro-Macosko rheology model and the Grindling kinetic model for R1 [43]

Castro-Macosko		Grindling	
Parameter	Value	Parameter	Value
C_1	1.276	R	8.3145
C_2	6.187	A_1	$3.2088 \cdot 10^6$
D	$7.54 \cdot 10^{-4}$	A_2	$8.3155 \cdot 10^5$
T_b	$7.17 \cdot 10^3$	E_1	$6.1458 \cdot 10^4$
γ_g	0.799	E_2	$5.3438 \cdot 10^4$
		n_1	4.24525
		n_2	1.72672
		m	1.1431
		$B_{2,\Delta T_g}$	19.2722
		c_1	$3.5369 \cdot 10^3$
		c_2	$5.9439 \cdot 10^3$

5.3 Resin viscosity modeling

R1 was characterized using DSC and rheological measurements with a new method developed for fast curing resin systems [43, 108]. The material parameters and models for the resin viscosity are taken from Bernath [43] and are summarized in Tab. 5.1. The resin viscosity is modeled with the Castro-Macosko rheology model in combination with the Grindling kinetic model (cf. Section 3.3.2). The characterization with rheology and kinetic model enables modeling of the non-isothermal time- and temperature-dependent viscosity.
Figure 5.3 shows the viscosity over time for R1 based on the rheology and kinetic model for two isothermal temperatures. The two curves show the expected behavior of lower initial viscosity and a faster increase in viscosity at a higher temperature. For a temperature of 393 K, the viscosity rapidly

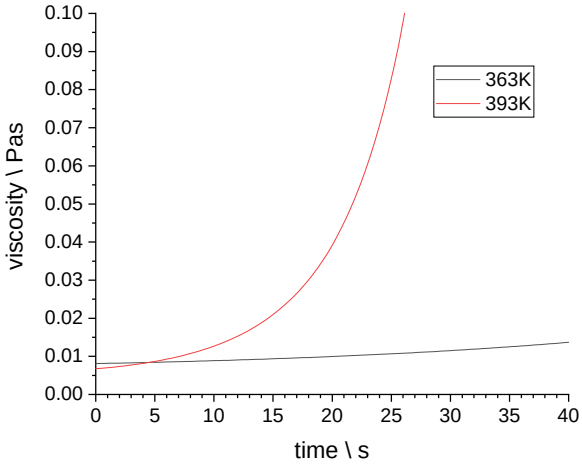

Figure 5.3: Modeled viscosity over time of R1 for two isothermal temperatures: 363 K and 393 K; the viscosities are calculated with a kinetic and a rheology model

increases to a value of over 0.1 Pa s before 30 s, which signifies a fast curing, but also a small mold-filling window during processing. The initial viscosity only differs slightly for the two temperatures shown here and is for both cases below 0.01 Pa s, which is a very low viscosity for RTM applications that eases infiltration.

R2 is again modeled using the Grindling kinetic model combined with the Castro-Macosko rheology model. The parameters for the resin system were characterized before by Bernath et al. [42, 43] and are summarized in Tab. 5.2. Figure 5.4 shows the viscosity evolution over time for the three isothermal temperatures 50 °C, 75 °C and 100 °C up to 5 min based on the viscosity model. The initial viscosity, as well as the increase rate, are clearly temperature-dependent. The three curves show the expected behavior: The higher the temperature, the lower the initial viscosity, and the faster increases the viscosity. The viscosity at 323 K is always above 0.2 Pa s, which implies a difficult infiltration at that temperature. For both higher temperatures, the initial viscosity is low enough,

Table 5.2: Parameters of the Castro-Macosko rheology model and the Grindling kinetic model for R2 [43]

Castro-Macosko		Grindling	
Parameter	Value	Parameter	Value
C_1	3.659	R	8.3145
C_2	$9.32 \cdot 10^{-4}$	A_1	$1.6117 \cdot 10^{7}$
D	$1.50 \cdot 10^{-12}$	A_2	$6.8176 \cdot 10^{4}$
T_b	$6.88 \cdot 10^{4}$	E_1	$6.7632 \cdot 10^{4}$
γ_g	0.72	E_2	$4.8852 \cdot 10^{4}$
		n_1	3.9227
		n_2	1.5940
		m	0.8518
		$B_{2,\Delta T_g}$	$8.3407 \cdot 10^{-2}$
		c_1	$2.1388 \cdot 10^{3}$
		c_2	$7.4994 \cdot 10^{3}$

while the viscosity at 373 K has a significantly lower mold-filling process window of less than 150 s.

R3 was characterized at one constant temperature of 80 °C using a plate/plate rheometer [18]. The average results were fitted to a polynomial function (Eq. (3.31)) and the resulting viscosity over time is shown in Fig. 5.5. The fitting parameters are given in Tab. 5.3. The resin has a viscosity of approximately 0.1 Pa s at the beginning and increases due to the starting curing reaction to 0.5 Pa s after 120 s.

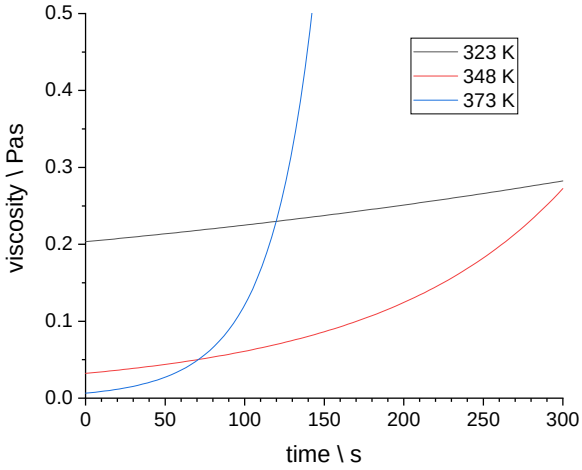

Figure 5.4: Modeled viscosity over time of R2 for three isothermal temperatures: 323 K, 348 K and 373 K; the viscosities are calculated with a kinetic and a rheology model

Table 5.3: Polynomial fitting parameters for the viscosity of R3 at 80 °C

Parameter	Value
D_0	$9.6450 \cdot 10^{-2}$
D_1	$6.4671 \cdot 10^{-4}$
D_2	$-6.1668 \cdot 10^{-5}$
D_3	$1.9900 \cdot 10^{-6}$
D_4	$-1.9492 \cdot 10^{-8}$
D_5	$7.3546 \cdot 10^{-11}$

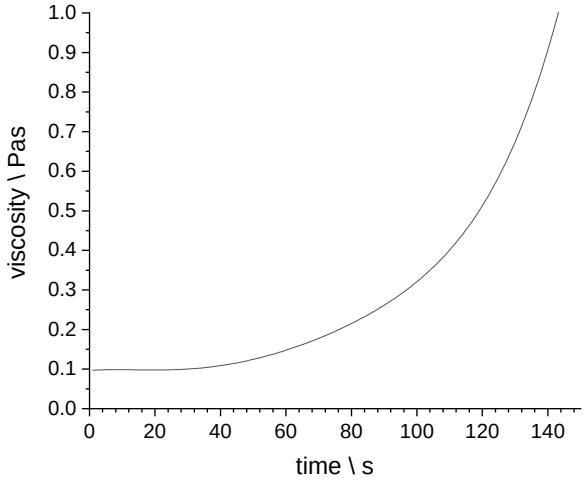

Figure 5.5: Modeled resin viscosity of R3 over time for one isothermal temperature of 80 °C; the viscosity over time is measured at 80 °C and fitted to a polynomial function

5.4 Permeability characterization and modeling[1]

The investigations in this work are based on the macro-scale resin flow. To characterize the macro-scale permeability, experiments with process parameters similar to the RTM process are best suited for accurate quantitative permeability values. The two parameters that mostly affect the permeability are the fiber orientation (resulting in anisotropic permeability) and the FVF. The test setup as well as the results are presented in the next sections.

[1] Parts of this section are based on [9] and [32]

5.4.1 Permeability test setup

The permeability is measured in a linear RTM mold-filling experiment. The RTM mold geometry is a rectangular plate with a linear injection gate that distributes the resin over the whole width of the plate to realize a one-dimensional flow. A non-reacting fluid (Mesamol®) is used for the experiments to avoid any influence of a non-constant viscosity. The experimental setup is schematically shown in Fig. 5.6. A constant injection pressure is used and the pressure is measured at several points in the cavity. By using Darcy's law, it is possible to calculate the permeability in the flow direction between the pressure sensors [92]. Thin spacer plates allow to change the cavity height and, thus, different FVF can be analyzed without changing the fabric layup.
This approach facilitates the calculation of the permeability and ensures comparability to the RTM process used afterward when manufacturing parts. On the other hand, it has the drawback of a higher experimental effort compared to transparent molds with a central pointwise injection gate, which permits the measurement of the anisotropic in-plane permeability directly in one experiment.

5.4.2 Permeability characterization results and modeling

Figure 5.7 compares the bidirectional carbon fiber fabric with the glass fiber fabric. Both fabrics show an exponential dependency of the permeability on the FVF, which is the usual behavior expected for these fabrics. The glass fiber fabric has a higher permeability than the bidirectional carbon fiber fabric over the whole measured FVF range. This result is explained by the anisotropic layup of the glass fiber fabric, which eases resin flow in the measured direction.

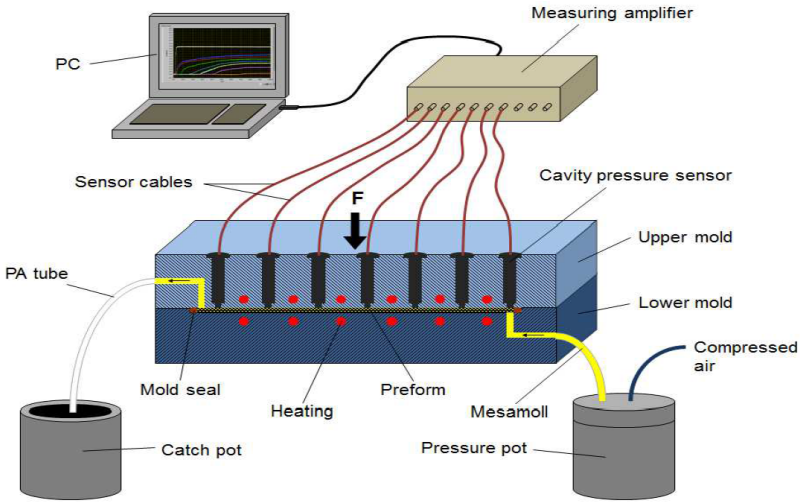

Figure 5.6: Schematic setup for experimental permeability characterization using a linear setup consisting of an RTM mold and aligned pressure sensors [92]

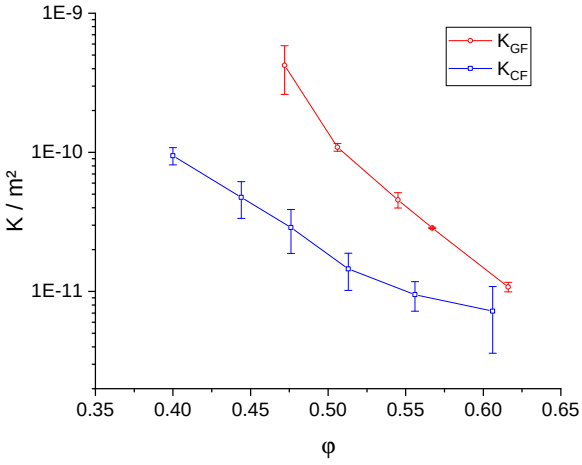

Figure 5.7: Permeability over FVF of the bidirectional carbon fiber fabric and the glass fiber fabric; adjusted from [31]

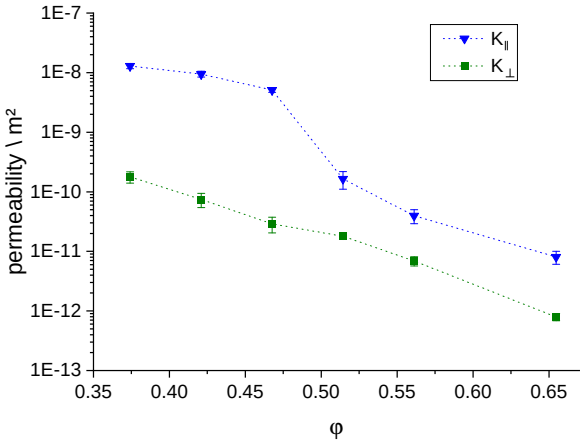

Figure 5.8: Permeability over FVF of the UD carbon fiber fabric for flow parallel and transverse to the main fiber orientation; adjusted from [9]

In Fig. 5.8, the measurement results of the UD carbon fiber fabric are shown. Again, the results show an exponential decrease of the permeability with increasing FVF. The permeability transverse to the fiber orientation is approximately one to two orders of magnitude smaller than the permeability parallel to the fibers.

The permeability measurement data points are directly implemented into the RTM mold-filling simulation model. Therefore, the data is interpolated between the measurement points with an interpolation type that can be chosen in each model like e.g. linear, exponential, or spline interpolation. Because the permeability shows an exponential dependence on the FVF, in this work always an exponential interpolation is chosen. The interpolated values are indicated in Fig. 5.7 and Fig. 5.8 as straight lines between the data points. When a layup consists of several UD fabrics that do not have the same orientation, the effective permeability is calculated by volume averaging of the principal permeabilities [63].

5.5 Fabric compaction characterization and modeling

Additionally to the fabric permeability, also the compaction stiffness of the fabrics is measured experimentally. The three fabrics characterized are the same as in the experimental permeability characterization.

5.5.1 Fabric compaction test setup

A uniaxial compaction test setup is used to characterize the compression stiffness of the UD carbon fiber fabric. Two different layups are characterized: 4 layers in $(0° \mid 90° \mid 90° \mid 0°)$ and 8 layers with $(0° \mid 90° \mid 90° \mid 0°)_{\mathrm{sym}}$.
The uniaxial compression is measured in a test bench that includes a pivoted head to minimize in-plane stresses. The compression speed is set to 1 mm min^{-1} and the compression distance is set to a value depending on the layup to reach 60% FVF. The force is measured by a measuring box and the evaluation of the results is based on the force-displacement relationship. Figure 5.9 shows the setup with a piece of compressed fabric. The size of the compaction die is 150 mm to 160 mm, which is chosen to be large enough to minimize meso-scale effects.

5.5.2 Fabric compaction results and modeling

The force-displacement relationship and the geometrical and material parameters are used to calculate a pressure-FVF function. In the material modeling, the Poisson ratio is assumed to be zero so that the Young's modulus used in the material model is equal to the measured bulk modulus.
The results of the compaction measurements of the UD carbon fiber fabric are shown in Fig. 5.10. The compaction pressure is non-linearly increasing from nearly zero to a value of about 1.0 bar at 60% FVF. The layup with 8 layers

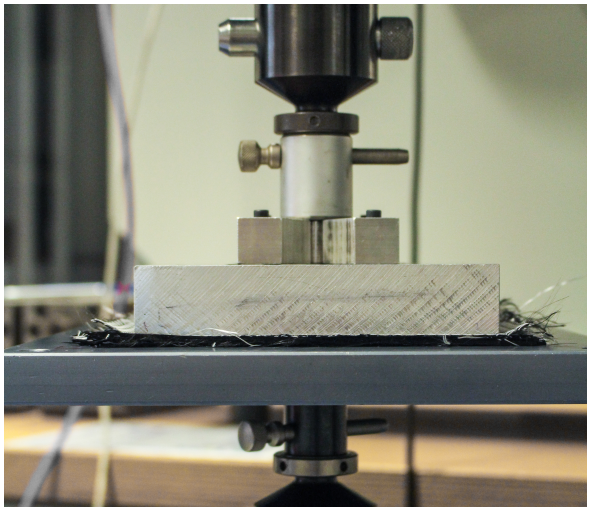

Figure 5.9: Dry fabric placed inside the UD test setup to measure the compaction behavior

shows a slightly faster increase between 45% and 60% FVF, which signifies a stiffer behavior in that configuration. This behavior was also observed in literature, though no explanation was given [142].
However, the difference between the two setups is small and all measurements are included in the calculation of the average modulus. The Young's modulus is calculated by deviating the compaction pressure after the (linear) compaction strain, which is done for each individual measurement. Afterward, the average is taken and used as the resulting modulus. The result is shown in Fig. 5.11. The Young's modulus shows a non-linear increase from nearly zero at 30% FVF to a value of about 1.5 MPa at 60% FVF.
A non-linear material model is needed to describe this behavior. The non-linear model is defined by a piece-wise linear function for $E(\varphi)$. Outside of the parameter range, the modulus is held constant at the lowest/highest value. The Poisson's ratio is set to be constant for all strains.

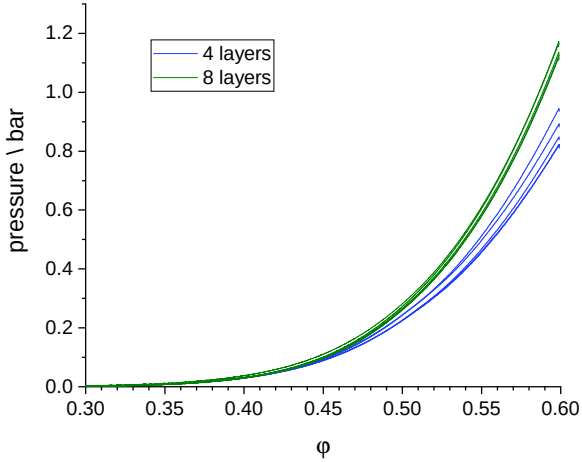

Figure 5.10: Compaction pressure over FVF of the UD carbon fiber fabric for 4 layers and 8 layers

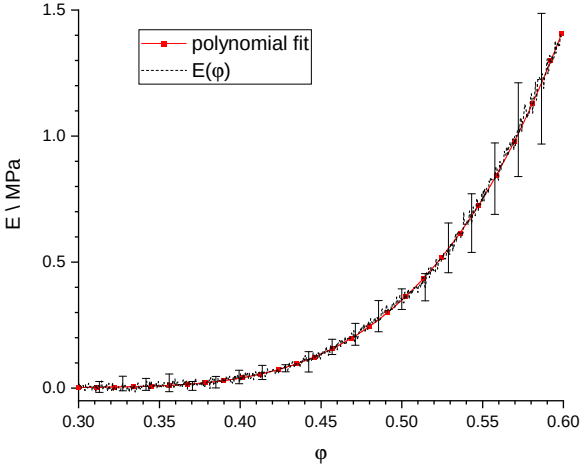

Figure 5.11: Young's modulus over FVF of the UD carbon fiber fabric; average value of the measurements and polynomial fit

Table 5.4: Polynomial fitting parameters for the Young's modulus of UD carbon fiber fabric

Parameter	Value in MPa
B_0	0.00
B_1	−29.18
B_2	277.92
B_3	−886.17
B_4	950.03

To implement the non-linear behavior into the simulation model, the Young's modulus is fitted to a polynomial function (Eq. (4.21)). The polynomial fitting parameters (Tab. 5.4) can be implemented directly into the constitutive model of the poro-elasticity FV method (cf. Section 4.2.3).
The compaction behavior of the carbon fiber bidirectional fabric was also measured experimentally using the same test setup [18]. Again, the Young's modulus is calculated based on the pressure-FVF function. Based on the average value of the measurements, the modulus over FVF is calculated by deviating the curve after the (linear) compaction strain. Figure 5.14 shows the resulting modulus over the FVF.
As expected, the modulus also depends strongly on FVF and shows an increasing compaction stiffness for high FVF. To fit the data to a model, here a piecewise linear function for $E(\varphi)$ is used to approximate the modulus-FVF function, which is also visualized in Fig. 5.12.
Additionally to the carbon fiber fabrics, the Young's modulus of the glass fiber fabric was characterized by Rosenberg [31]. He used a test setup, where he could also measure the compaction forces of fiber clampings and sealings. The average result and the standard deviation regarding the fabric compaction pressure are shown in Fig. 5.13. Equal to the compaction of the carbon fiber fabrics, the compaction pressure is non-linearly increasing. The pressure

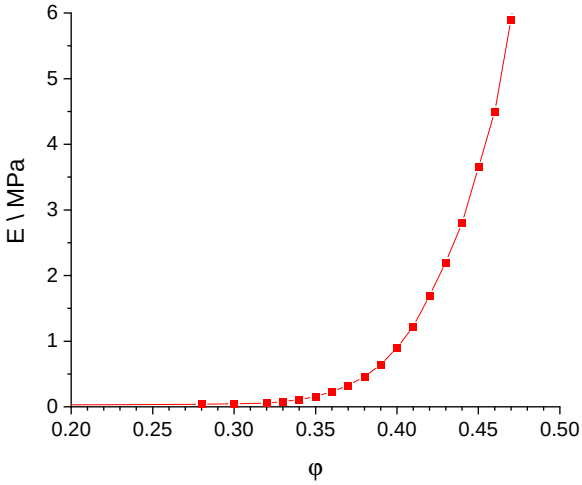

Figure 5.12: Modeled Young's modulus over FVF of the bidirectional carbon fiber fabric; the data points for a piecewise linear fit are indicated by the rectangles; the measurement was carried out by Behnisch et al. [18]

reaches a value of about 1.8 bar at 60% FVF. The Young's modulus is calculated with the same method as for the carbon fiber fabrics. Also for the glass fiber fabric, the modulus is non-linearly increasing between 40% FVF and 55% FVF, whereas for higher FVF it shows a linear increase.
To fit the data to a model, again a piecewise linear function is used to approximate $E(\varphi)$. The resulting function is shown in Fig. 5.14.

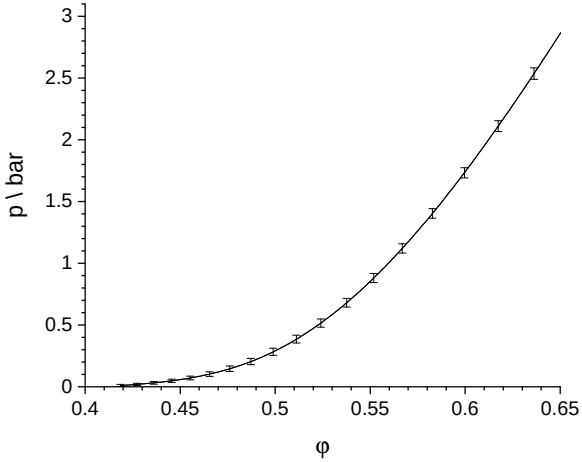

Figure 5.13: Compaction pressure over FVF of the glass fiber fabric; adjusted from [31]

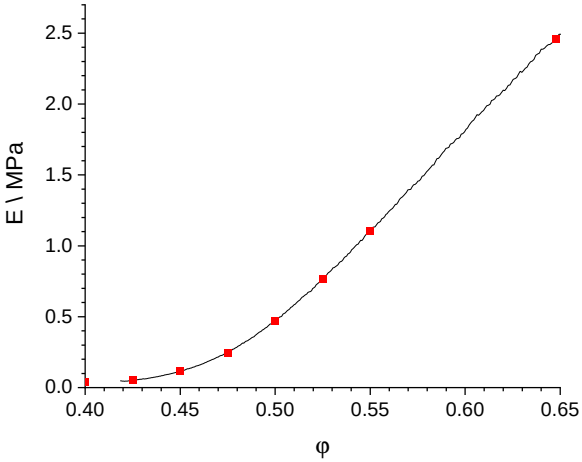

Figure 5.14: Average Young's modulus over FVF of the glass fiber fabric; the data points for a piecewise linear fit are indicated as red rectangles

5.6 Polymer foam core compression characterization and modeling

Additional to the fabric parameters, it is crucial to know the deformation behavior of the foam core material to realistically predict mold-filling in RTM with embedded polymer foam cores. The focus of this section is, thus, on the characterization of polymer foam cores under RTM-specific loads. As extruded PET foam shows an anisotropic behavior for compression loads, two types of experiments are used to characterize the material. The first tests use a hydrostatic test setup to measure the volumetric compression, the second test setup is a uniaxial compression in the thickness direction.

5.6.1 Hydrostatic characterization

To characterize the compression behavior in a test environment close to RTM mold-filling, a hydrostatic test setup is used that was initially developed by Gerstenkorn [166] and further extended at Fraunhofer ICT.

Hydrostatic test setup

The schematic setup of the hydrostatic tests is shown in Fig. 5.15. It consists of a heated reservoir with silicone oil that can be heated up to 100 °C. The test cylinder, as well as all hydraulic hoses, are isolated to help reach a homogeneous temperature in all components of the test setup. A high flow rate hydraulic pump fills and empties the reservoir, while the high-pressure pump is active during the testing and allows to increase the pressure at a controlled small flow rate. The test cylinder is made of steel to minimize elastic deformation and contains a temperature and a pressure sensor. Additionally, a small glass window allows observing the foam specimen during characterization.
Figure 5.16 shows the pictures of the test cylinder and one exemplary polymer foam test specimen. The specimens have a size of 45 mm x 45 mm x 15 mm.

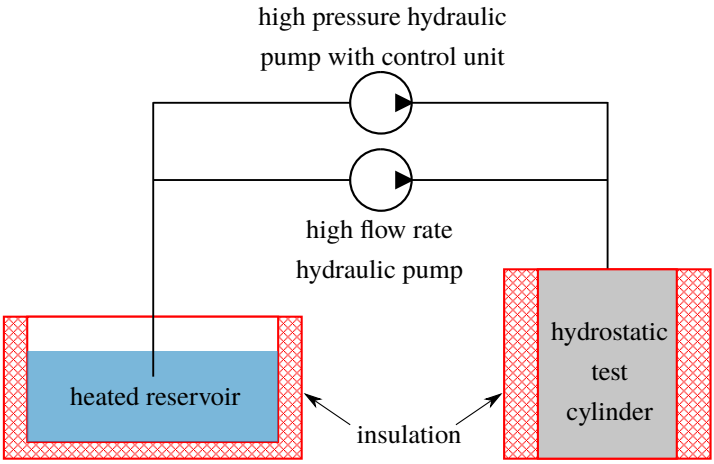

Figure 5.15: Schematic setup for the hydrostatic compression tests using a pressurized cylinder with heated silicone oil

The size is chosen big enough to measure the macroscopic behavior of the foam. The experiments are carried out at three different temperatures, 50 °C, 75 °C and 100 °C to analyze the influence on the mechanical behavior in a temperature range equal to a typical RTM process.

For characterization, the test specimens are inserted into the empty test cylinder, which is subsequently filled with the heated oil. To allow the foam specimen to heat up, the foam is left for 5 min in the non-pressurized chamber until the measurement starts.

A special procedure is needed to calculate the volumetric strain of the foam core because several factors influence the measurement results. The flow rate of the high-pressure pump and the pressure inside the test cylinder are directly measured and lead to a pressure-volume change relationship that at this point

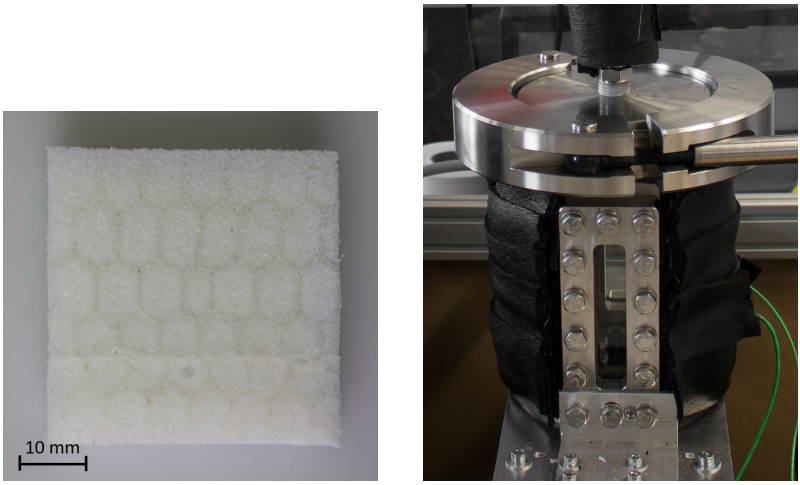

a) b)

Figure 5.16: a) Test specimen of the PET foam; b) hydrostatic test cylinder with thermal insulation

still includes the influence of the test setup. The volume change of the foam material is therefore calculated by subtracting all influencing errors:

$$\Delta V_{\text{foam}} = \Delta V_{\text{test}} - \Delta V_{\text{setup}} \tag{5.1}$$

$$= \Delta V_{\text{test}} - \left(\Delta V_{\text{deformation,elastic}} + \Delta V_{\text{leakage}} + \Delta V_0\right). \tag{5.2}$$

Three error factors were identified in the experiments: An elastic deformation of the test cylinder and hydraulic hoses $\Delta V_{\text{deformation,elastic}}$, a small leakage through the valves $\Delta V_{\text{leakage}}$ and a constant initial volume ΔV_0 that is caused by minimal air entrapment inside the hydraulic system.

Table 5.5: Hydrostatic test setup correction parameters

Temperature	50 °C	75 °C	100 °C
A	0.93	0.96	1.16
n	0.75	0.76	0.72
B	1.5	3.4	3.9
C	0.3	0.4	0.5

The elastic deformation of the test setup is represented by a power law function, whereas leakage and air entrapment correction are a characterized as a function of time and a scalar value, respectively:

$$\Delta V_{\text{deformation,elastic}} = A \cdot p^n, \tag{5.3}$$

$$\Delta V_{\text{leakage}} = B \cdot t, \tag{5.4}$$

$$\Delta V_0 = C, \tag{5.5}$$

with pressure p and time t. The correction parameters A, B, n, and C are fitted using tests with a cavity that is purely filled with silicone oil at different temperatures. In the calibration tests, the cavity is first pressurized at a constant flow rate. Subsequently, the pressure is held constant for 2 min to measure the leakage over a longer time period. The resulting correction parameters are shown in Tab. 5.5.

Figure 5.17 shows one example of the correction of a foam experiment. The measured p-ΔV curve is corrected with the correction functions to get the pure foam deformation.

Analyzing the foam material at three densities and three different temperatures leads to nine test sets in total. In the hydrostatic setup, each set is repeated six times. The test parameters are summarized in Table 5.6.

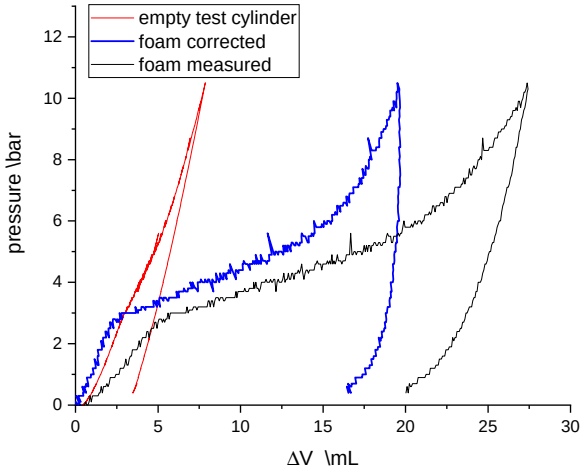

Figure 5.17: Exemplary curves of measured pressure over volume difference for the test chamber containing only fluid (red) and with embedded foam specimen (black). The corrected volume difference of the foam (blue) is calculated by Eq. (5.2)

Table 5.6: Hydrostatic test parameters for the PET foam characterization

Foam core density	$80\,\mathrm{g\,L^{-1}}$, $100\,\mathrm{g\,L^{-1}}$, $130\,\mathrm{g\,L^{-1}}$
Temperature	50 °C, 75 °C, 100 °C
Pressure	10 bar, 15 bar
Flow rate	$20\,\mathrm{mL\,min^{-1}}$

Hydrostatic test results

To give a better comparison of the experiments and to further on fit them to a suitable mechanical model, the linear volumetric strain ε_V is calculated with the uncompressed specimen volume $V_{specimen} = 30\,375\,mm^3$:

$$\varepsilon_V = \frac{\Delta V_{foam}}{V_{specimen}} \tag{5.6}$$

Figure 5.18 shows the test results of the pressure plotted over the volumetric strain for all nine parameter sets. The first row shows the results with a foam core temperature of 50 °C and with decreasing foam density from left to right. Rows two and three show the results with 75 °C and 100 °C, respectively. All of the plots show the three stages of the typical foam compression behavior (cf. Fig. 5.1). First, they exhibit a steep pressure increase, which indicates the linear-elastic region. The steep increase is followed by a wide plateau that corresponds to the elastic-plastic region. The first occurring strong decrease in the stiffness is used to define the maximum pressure that the foam can withstand without plastic deformation. It ranges from 6 bar for a foam core density of $130\,g\,L^{-1}$ at 50 °C to approximately 0.5 bar for $80\,g\,L^{-1}$ at 100 °C. After the elastic-plastic plateau, a fast increase of the pressure - the foam densification - is again visible until the flow rate stops at reaching 10 bar or 15 bar.
The expected dependency of the density and temperature on the mechanical behavior is obvious in the experiments. Both for higher temperatures (from top to bottom) and for lower densities (from left to right), the mechanical properties decrease. Especially between 75 °C and 100 °C a strong decrease is visible, which is explained by exceeding the glass transition temperature of PET that is approximately 80 °C.

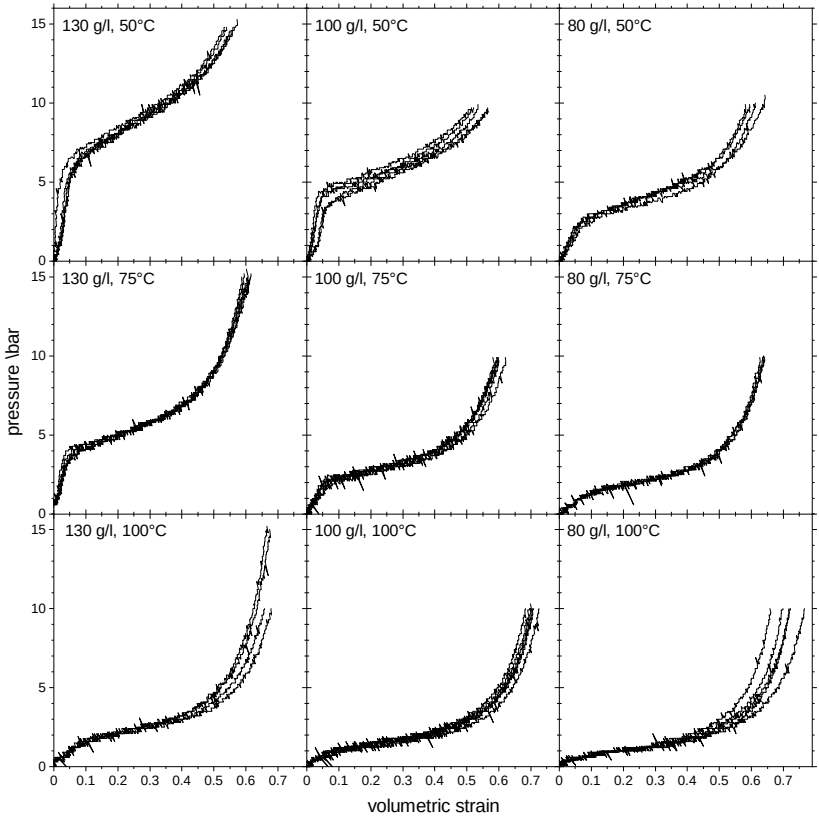

Figure 5.18: Hydrostatic test data of pressure over volumetric strain for all tested specimen; the foam densities are $80\,\mathrm{g\,L^{-1}}$, $100\,\mathrm{g\,L^{-1}}$ and $130\,\mathrm{g\,L^{-1}}$ with temperatures of 50 °C, 75 °C and 100 °C

Table 5.7: Uniaxial test parameters for the PET foam characterization

Foam core density	80 g L^{-1}, 100 g L^{-1}, 130 g L^{-1}
Temperature	20 °C, 50 °C, 75 °C, 100 °C
Compression speed	2 mm min^{-1}
Maximum displacement	4 mm

5.6.2 Uniaxial characterization

The PET foam material is made in an extrusion process, which leads to significantly higher mechanical stiffness in the thickness direction. Hence, an uniaxial compression test setup is used to determine the foam properties in thickness direction besides the volumetric hydrostatic tests presented in the previous section.

Uniaxial test setup

A universal test unit (Zwick&Roell, ZMART.PRO) is used in combination with an industrial oven to realize the uniaxial tests at the same elevated temperature levels as in the hydrostatic setup. Figure 5.19 shows exemplarily a foam specimen in the test chamber. A pivoted head is used to ensure parallel compression and minimize in-plane stresses. The foam specimens have the same dimensions and are cut from the same foam plate as in the hydrostatic tests for comparability of the results.

The compression speed is set to 2 mm min^{-1} and the maximum compression displacement is set to 4 mm. The force is measured by a measuring box with a maximum force of 12 kN. The evaluation of the results is based on the measured force-displacement relationship.

Analyzing the PET foam material at three densities and four different temperatures lead to twelve test sets in total. In the hydrostatic setup, each set is repeated three times. The test parameters are summarized in Table 5.7.

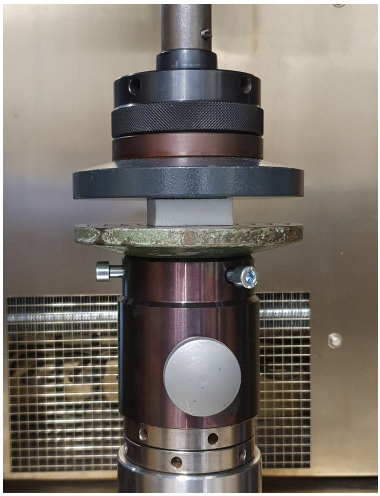

Figure 5.19: Test specimen inside the uniaxial test setup; The setup is built inside an oven to realize the experiments at elevated temperatures

Uniaxial test results

The results of the uniaxial tests are summarized in Fig. 5.20. The force-displacement values are combined with the specimen geometry to calculate the surface pressure (eq. to normal engineering stress) and the normal linear strain. Equal to the hydrostatic experiments, the strong influence of the foam density and the foam temperature on the stiffness and strength is evident from the measurements. However, the pressure level is much higher, when the elastic-plastic plateau is reached. This point can again be used to define the maximum thickness compaction stress that the foam can withstand without plastic deformation. It ranges from 24 bar for a foam core density of $130\,\mathrm{g\,L^{-1}}$ at 20 °C to approximately 3 bar for $80\,\mathrm{g\,L^{-1}}$ at 100 °C. Between 75 °C and 100 °C a strong decrease in the compressive strength is visible for all foam densities. This is again explained by exceeding the glass transition temperature of PET between these temperatures.

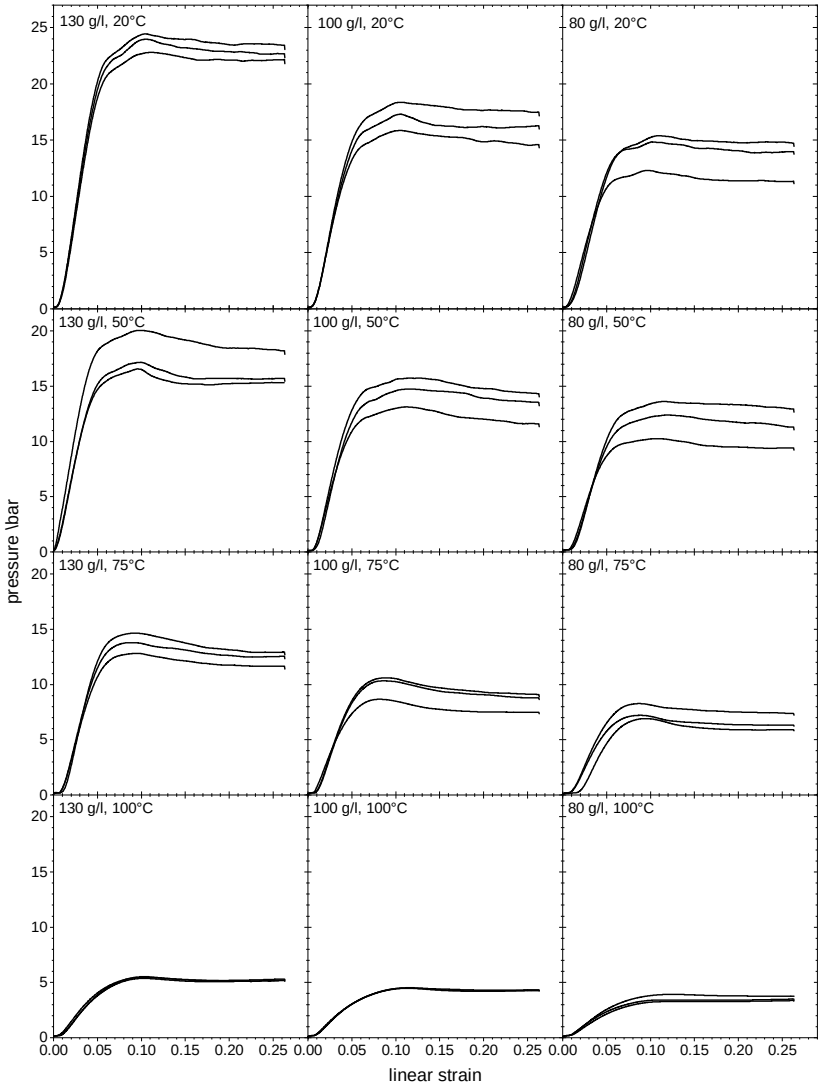

Figure 5.20: Uniaxial test data of pressure over linear strain for all tested specimen; the foam densities are 80 g L^{-1}, 100 g L^{-1} and 130 g L^{-1} with temperatures of 20 °C, 50 °C, 75 °C and 100 °C

Table 5.8: Young's moduli $E_{||}$ of the PET foams at three densities and four temperatures; measured with uniaxial tests

	20 °C	50 °C	75 °C	100 °C
80 g L^{-1}	32.0 MPa	28.7 MPa	19.5 MPa	5.9 MPa
100 g L^{-1}	40.0 MPa	34.3 MPa	25.1 MPa	7.4 MPa
130 g L^{-1}	52.0 MPa	44.0 MPa	34.2 MPa	9.1 MPa

5.6.3 Foam core material model

To model the compressive behavior of the foam core, transverse isotropic linear-elastic material models are parameterized. The models are valid in the linear-elastic part until the elastic-plastic plateau is reached. This is also the range, that the pressure load during mold-filling in RTM should not exceed, as plastic deformation has to be avoided.

Based on the results of the uniaxial tests, Young's moduli $E_{||}$ in the thickness direction can be calculated. The calculation is done according to DIN EN ISO 844 [167]. The main step is to find the steepest inclination in a range between 25% and 75% of the maximum pressure in the linear-elastic part. The resulting moduli are summarized in Table 5.8.

The equivalent volumetric moduli E_V are calculated with the hydrostatic test results using the same norm as used for $E_{||}$ but using the pressure and volumetric strain:

$$E_V = \frac{p_{\text{hydrostatic}}}{\varepsilon_V} . \tag{5.7}$$

The resulting values are summarized in Tab. 5.9. Subsequently, the Young's moduli in transverse direction are calculated by combining the uniaxial results with the volumetric test results. Assuming an linear-elastic transversal-isotropic

Table 5.9: Effective volumetric Young's moduli E_V of the PET foams at three densities and three temperatures; measured with hydrostatic tests

	50 °C	75 °C	100 °C
80 g L^{-1}	4.45 MPa	1.99 MPa	1.07 MPa
100 g L^{-1}	7.64 MPa	5.00 MPa	1.72 MPa
130 g L^{-1}	13.92 MPa	9.10 MPa	1.87 MPa

material with $E_1 = E_{||}$ and $E_2 = E_3 = E_\perp$, the principal strain coefficients are given as:

$$\begin{aligned}
\varepsilon_1 &= \frac{1}{E_{||}} \cdot \sigma_1 - \frac{\nu_{12}}{E_{||}} \cdot \sigma_2 - \frac{\nu_{12}}{E_{||}} \cdot \sigma_3 \\
\varepsilon_2 &= -\frac{\nu_{12}}{E_{||}} \cdot \sigma_1 + \frac{1}{E_\perp} \cdot \sigma_2 - \frac{\nu_{23}}{E_\perp} \cdot \sigma_3 \\
\varepsilon_3 &= -\frac{\nu_{12}}{E_{||}} \cdot \sigma_1 - \frac{\nu_{23}}{E_\perp} \cdot \sigma_2 + \frac{1}{E_\perp} \cdot \sigma_3
\end{aligned} \tag{5.8}$$

with the principal engineering stresses σ_1, σ_1 and σ_3 as well as the Poisson's ratios ν_{12} and ν_{23}.
It was shown experimentally that the Poisson's ratio decreases with compressive strain to a value close to zero in the elastic-plastic range [168]. In the linear-elastic range, the Poisson's ratio is assumed to be $\nu_{12} = \nu_{13} = \nu = 1/3$.
With the linearized volumetric strain in combination with the hydrostatic load

$$\varepsilon_V = \varepsilon_1 + \varepsilon_2 + \varepsilon_3 \,, \tag{5.9}$$

$$p_{\text{hydrostatic}} = -\sigma_1 = -\sigma_2 = -\sigma_3 \,, \tag{5.10}$$

the transverse Young's moduli $E_\perp$ can be calculated. The resulting values are summarized in Tab. 5.10.

Table 5.10: Youngs moduli $E_\perp$ of the PET foams at three densities and three temperatures; calculated

	50 °C	75 °C	100 °C
80 g L^{-1}	5.68 MPa	2.57 MPa	1.35 MPa
100 g L^{-1}	9.48 MPa	6.25 MPa	2.13 MPa
130 g L^{-1}	16.79 MPa	11.14 MPa	2.33 MPa

Furthermore, the definition of two shear moduli, $G_\perp$ and $G_{||}$, is necessary to complete the transverse-isotropic material model. During the mold-filling, the foam core material is only affected by normal loads of the compacted fabric and hydrostatic loads of the resin. The resulting stress is therefore expected to be dominated by normal stresses and, thus, the shear moduli do not strongly affect the solution. Based on the Young's moduli and the Poisson's ratios, the shear moduli $G_\perp$ and $G_{||}$ are calculated with:

$$G_\perp = \frac{E_\perp}{2(1+\nu)}, \tag{5.11}$$

$$G_{||} = \frac{G_{||}}{2(1+\nu)}. \tag{5.12}$$

With this simplified calculation, the shear moduli are assured to be positive definite. The resulting values are summarized in Tab. 5.11 and Tab. 5.12.
To verify the material model, the hydrostatic pressure over the volumetric strain is calculated using the transverse-isotropic material and Equations (5.8) to (5.10). Figure 5.21 shows the resulting linear functions for the fitted model compared to the average of the experimental trials in the hydrostatic test chamber. Until a volumetric strain of approximately 5%, the fitted curves show a good agreement. For higher strains, the curves diverge because of the strongly non-linear behavior of the foam core.

Table 5.11: Shear moduli $G_{||}$ of the PET foams at three densities and three temperatures; calculated

	50 °C	75 °C	100 °C
80 g L^{-1}	10.79 MPa	7.33 MPa	3.84 MPa
100 g L^{-1}	12.89 MPa	9.44 MPa	4.17 MPa
130 g L^{-1}	16.54 MPa	12.86 MPa	3.42 MPa

Table 5.12: Shear moduli $G_{\perp}$ of the PET foams at three densities and three temperatures; calculated

	50 °C	75 °C	100 °C
80 g L^{-1}	2.13 MPa	0.97 MPa	0.51 MPa
100 g L^{-1}	3.56 MPa	2.35 MPa	0.80 MPa
130 g L^{-1}	6.31 MPa	4.19 MPa	0.88 MPa

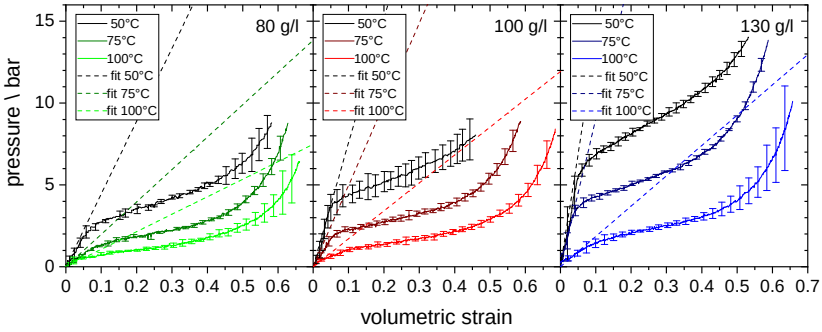

Figure 5.21: Comparison of the hydrostatic compaction pressure over volumetric strain of the experimental results and the fitted transverse-isotropic material for foam core densities of 80 g L^{-1}, 100 g L^{-1} and 130 g L^{-1} (from left to right) at 50 °C, 75 °C, and 100 °C

5.7 Discussion

In this work, the fabrics are characterized using state-of-the-art methods regarding permeability and compaction. The permeabilities of all measurements vary in a range between 1×10^{-8} m^2 and 1×10^{-12} m^2 for an FVF between 37 % and 66 %. The measurement method is limited to this range of FVF, which matches approximately the range of RTM manufacturing. The measurements show that the glass fiber layup has a higher permeability than the measured bidirectional carbon fiber layup. This results mainly from the non-symmetrical layup of the glass fiber fabric with two layers in 0° direction, which eases resin flow in measurement direction. Furthermore, glass fiber fabrics tend to have a higher micro-scale permeability because of the larger filament radius of glass fibers compared to carbon fibers. This influence of the fiber radius is also present in the model by Gebart (Eq. 3.18). However, the micro-scale permeability is also influenced by the heterogeneous distribution of the filaments inside the roving, which was shown recently by Seuffert et al. [101]. The UD carbon fiber layup shows a strong anisotropic permeability. The permeability along the main fiber direction is approximately one order of magnitude higher than in the transverse direction and even increasing for low FVF. The results emphasize the importance to consider anisotropic and FVF-depending permeability in each RTM mold-filling simulation. Remembering Darcy's law (Eq. 3.1), the permeability is linearly proportional to the pressure gradient. For a change of 10 % in FVF, the permeability and the pressure gradient change approximately one order of magnitude and thus heavily influence the mold-filling and cavity pressure. For processes involving non-constant cavities, the FVF can also change locally during the mold-filling, which results in non-uniform permeabilities and in the following leads to an inhomogeneous resin flow. As the permeability is significantly determining the mold-filling, high accuracy of the measured values is key to gaining realistic simulation results.

The compaction behavior of the three analyzed fabrics shows a strongly nonlinear increase in the compaction pressure towards high FVF. For low FVF, the

materials exhibit nearly no compaction pressure, whereas it rises up to values of 3 bar at 65% FVF (cf. Fig. 5.13). This compaction pressure influences the pressure-control in PC-RTM. However, the compaction pressure is still low compared to the fluid pressure in PC-RTM that ranges between 15 bar to 30 bar and, thus is not expected to strongly influence the mold-filling. The influence of the fabric compaction onto the PC-RTM mold-filling simulation is analyzed in Section 6.1 in the following chapter.
However, for processes that use lower injection pressures or have flexible molds like VARI or D-SCM, the compaction behavior directly influences the mold-filling behavior. The higher the compaction stiffness, the lower is the FVF, which in the following leads to higher permeabilities. The newly developed simulation method in this work allows simulating this coupled infiltration and fabric compaction, which is shown for the D-SCM process in Section 6.2 in the following chapter.
The anisotropic characterization of the PET foam core is carried out by a combination of two test setups. The results show that the chosen PET foam material stiffness in the thickness direction is approximately 3 to 6 times higher than in the transverse direction. The relative values of the moduli in transverse direction compared to thickness direction $E_{\perp}/E_{||}$ are visualized in Fig. 5.22. The values furthermore show a tendency of more anisotropic behavior for lower foam densities. To better understand this effect, it is necessary to investigate the manufacturing process of the foam and its influence on the pore sizes and geometries.
Additional to the anisotropy, the polymer foam mechanical properties have a strong dependency on the temperature. Figure 5.23 shows the relative decrease of the compressive modulus in the thickness direction for the measured temperature range. Compared to the data at room temperature, the values are significantly lower for higher temperatures and decrease to less than 20% of the value at room temperature. It is, therefore, important to know the foam core temperature during processing, as it affects the mechanical properties of the foam core.

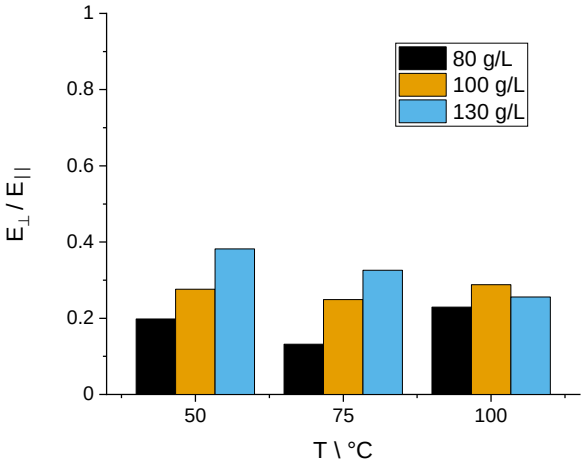

Figure 5.22: Relative values of the average compressive transverse Young's modulus $E_{\perp}$ from Tab. 5.10 to thickness direction $E_{||}$ from Tab. 5.8 for the PET foam at three densities

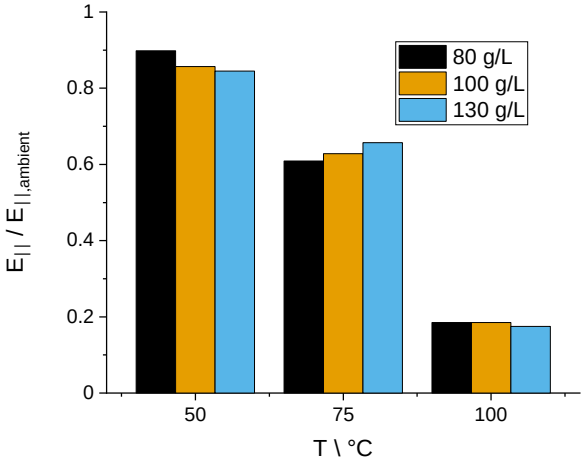

Figure 5.23: Relative values of the average compressive Young's modulus in thickness direction $E_{||}$ from Tab. 5.8 to data at ambient temperature $E_{||,\text{ambient}}$ for the PET foam at three densities

During the manufacturing of sandwich RTM parts, the presence of very light, soft polymer foam cores act comparable to a flexible mold wall and, thus, also limit the achievable FVF. During the closing of the mold, the FVF in the cavity rises and the fabric, as well as the foam core, are compressed. For temperatures higher than 75 °C, the compression moduli of the PET foam at all analyzed densities is in the same order of magnitude as the compaction modulus of the fabric, which indicates that they interact on a relevant scale during the closing of the mold and the mold-filling. As the permeability is very sensitive to small changes in the FVF, this coupled behavior has to be studied, which is the focus of Section 6.3 in the following chapter.

6 Application Examples and Validation

The developed method for mold-filling in RTM with a non-constant cavity is applied to three different manufacturing types. The three application examples are of increasing complexity regarding the method needed to describe the mold-filling. The first application with validation is done for a plate geometry that is infiltrated using the PC-RTM process (Section 6.1). Here, the fabric compaction influences the measured pressure at the integrated sensor, which is used for pressure control. Following, also the mold-filling and the final gap height are influenced.

To emphasize that the developed method is not only limited to RTM mold-filling, the second application example shows the infiltration simulation of D-SCM (Section 6.2). In this process, the foam expansion pressure is used to apply a compaction pressure onto a partly-infiltrated fabric, which results in simultaneous resin infiltration and fabric compaction. The D-SCM process is described in detail in Section 6.2.

The first and second examples use the internal coupling method for preform compaction and fluid flow, which was introduced and verified in Section 4.3.

The third application example is an RTM process of a hat geometry with an embedded foam core, which uses internal and external coupling to describe the interdependence of mold-filling with preform compaction and sandwich core deformation, which was introduced and verified in Section 4.4. A numerical

study analyzes the influence of an embedded foam core onto mold filling. Furthermore, a comparison of simulation results to experimental RTM infiltrations validates the FSI method and the simulation model (Section 6.3).

6.1 Mold-filling of PC-RTM with fabric compression [1]

The PC-RTM mold-filling simulation method was validated by Seuffert et al. [32]. In the publication, no poro-elasticity approach was used to describe the compaction of the cavity. Instead, a uniform deformation of the fabric over the mesh height was assumed, which was modeled by solving a Laplace equation with a uniform diffusivity coefficient for the movement of the mesh nodes. This method enables modeling of the changing FVF during the mold-filling but without calculating the compaction force of the fabric. In the validation experiments, an initial pressure was observed at the sensor in the mold before the injection was started. As the initial pressure is increasing with a decreasing initial mold gap height, it is assumed that the initial pressure results from the preform compaction. To validate this, the simulations are extended with an internal coupling of the preform compaction by using the method developed in Section 4.3.

6.1.1 PC-RTM mold-filling simulation model

Experiments were carried out using a rectangular plate geometry with a linear injection gate which leads to a predominant one-dimensional resin flow. The tool contains an integrated fiber clamping to seal the cavity. The materials used are the glass fiber fabric with a layup of (0° | 90° |0°) and the epoxy resin system

[1] Parts of this section are based on [32]

Table 6.1: PC-RTM validation case process and geometry parameters

Parameter	Value	Description
$q_{\text{injection}}$	$1 \times 10^{-6}\,\text{m}^3\,\text{s}^{-1}$	injection flow rate
$t_{\text{injection}}$	6.6 s	injection duration
p_{outlet}	1 bar	outlet pressure
$h_{\text{cavity,final}}$	2.3 mm	final cavity height
h_{clamping}	1.6 mm	final height at fiber clamping
p_{control}	15 bar	pressure control value
g_{start}	0.1 / 0.3 / 0.7 mm	initial cavity gap height

R1. The description of the experimental setup is given in detail by Seuffert et al. [32].

Figure 6.1 shows the geometry of the rectangular plate together with the boundary conditions applied at the edges. The symmetry of the plate is used to model only half of the cavity. The mesh consists of uniform hexahedral elements with a grid size of 5 mm in both in-plane directions and four elements in the thickness direction.

The initial height of the cavity and the fabric is set to 3.5 mm in the simulation model. During the first dry compression step, the cavity is closed to the initial gap height. Three different starting conditions are analyzed, where the mold gap height at the beginning of the injection is set to 0.1 mm, 0.3 mm and 0.7 mm. After the compression, the injection is started with a constant flow rate. The control pressure is set to 15 bar. A fiber clamping at all edges of the plate is integrated into the tool to compress the fabric to very high FVF, which decreases the permeability strongly and, thus, seals the cavity. At high mold gap heights, this sealing allows a small amount of resin to flow out of the cavity, which is also the implemented in the simulation model. Further process and material parameters are summarized in Tab. 6.1.

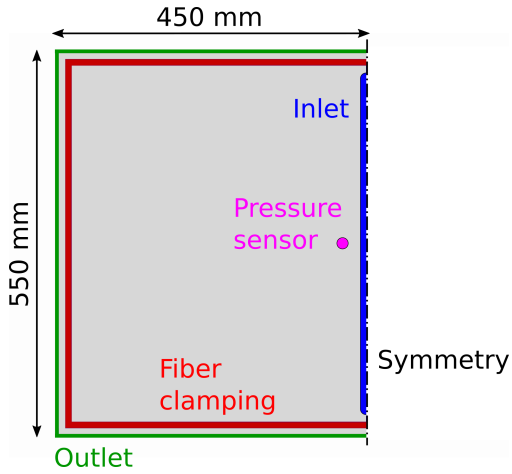

Figure 6.1: Geometry of the rectangular plate with boundary conditions and pressure sensor position used in PC-RTM [32]

The permeability of the glass fiber fabric is given in Section 5.4.2, Fig. 5.7, the compaction stiffness is given in Section 5.5.2, Fig. 5.14. Both material parameters are implemented as piecewise linear functions depending on the FVF into the simulation model. The viscosity model of the epoxy resin system R1 is implemented using the Grindling kinetic model and the Castro-Macosko rheological model with the parameters given in Section 5.3, Tab. 5.1.

6.1.2 PC-RTM mold-filling results

The results of the mold-filling simulations including the fabric compaction are compared to simulations, where the pressure control is done using only the fluid pressure and furthermore to RTM mold-filling experiments. At least three experiments are carried out for each configuration. For the comparison, the pressure at the sensor position and the mold gap height are evaluated during the injection and compression stage until the cavity is filled after 10 s.

Figure 6.2 shows the results with an initial mold gap height of 0.1 mm. The time scale is shifted so that the injection starts at 0 s. Before the injection starts, the mold is closed to the initial gap height. Comparing the simulation pressure graphs (green lines), it can be noticed that the pressure at the beginning of the injection is higher for the simulation including compaction, which shows the pressure force added by the compacted fabric onto the fluid pressure. During the injection stage, the pressure increases rapidly until the control value of 15 bar is reached. Afterward, the pressure stays constant at this value, only at the beginning of the compression stage, the influence of the PID-controller is visible in the oscillating pressure until it is stabilized again. The mold gap height for both simulations increases in the injection phase during the pressure-controlled stage nearly similarly. In the compression stage, the mold gap height of the simulation including compaction decreases slower than that simulated with the fluid pressure approach. Especially in the compression phase, the mold gap height of the simulations with compaction shows an excellent agreement to the experimentally measured value.

Comparable results are obtained for the simulations and experiments with an initial gap height of 0.3 mm, visualized in Fig. 6.3. Because of the lower FVF compared to the first set-up, the pressure increases slower until the pressure control value is reached. As expected, the mold gap height increases earlier and to a higher maximum value for the simulation containing the fabric compaction. Furthermore, the compression is slower than predicted by the simulations without fabric compaction. Again, especially the compression stage shows an excellent agreement between the experiments and the simulations using compaction.

Figure 6.4 shows the results of the third set-up investigated with an initial gap height of 0.7 mm. In this configuration, the pressure limit of 15.0 bar is not reached in the injection stage because of the low FVF and following high permeability at the initial gap height. In the compression stage, the pressure control is activated to set the compression speed. As expected, the compression in the simulation without compaction is faster than in the configuration with

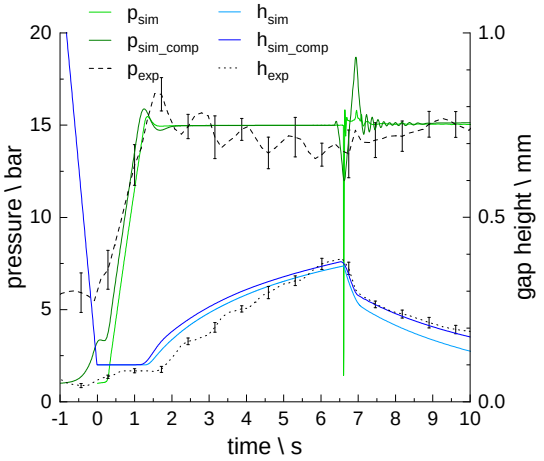

Figure 6.2: Comparison of PC-RTM gap height and pressure at the control sensor of the simulations and experiments for an initial gap height of 0.1 mm; in case of the experiments, the average values and standard deviations are shown

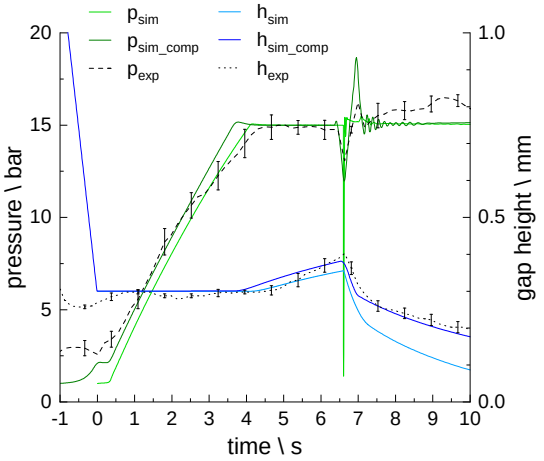

Figure 6.3: Comparison of PC-RTM gap height and pressure at the control sensor of the simulations and experiments for an initial gap height of 0.3 mm; in case of the experiments, the average values and standard deviations are shown

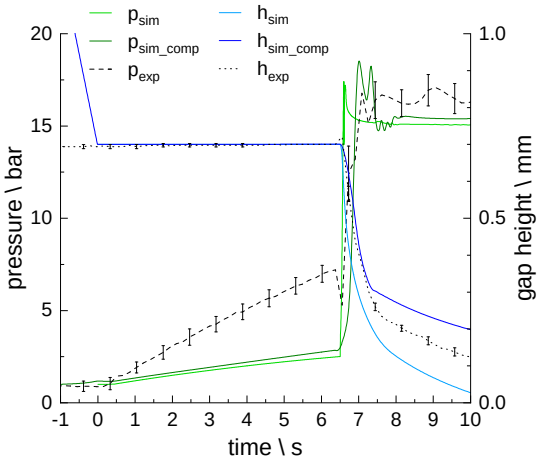

Figure 6.4: Comparison of PC-RTM gap height and pressure at the control sensor of the simulations and experiments for an initial gap height of 0.7 mm; in case of the experiments, the average values and standard deviations are shown

compaction force. The experimental result of the mold gap height lies between both simulation results. The difference in pressure increase during the injection can be explained by the permeability uncertainty of the glass fiber fabric for low fiber volume fractions (cf. Fig. 5.7). At a gap height of 0.7 mm, the FVF is 47.2%, where the measured permeability scatter is approximately 100%.

6.2 Infiltration in D-SCM

This application example of the Direct Sandwich Composite Molding (D-SCM) process is given to show the capability of the developed internal coupling method to be applied for different kinds of composite manufacturing processes that involve non-constant cavities during the mold filling. Here, the focus is on applying the method to a manufacturing process that involves a flexible cavity surface and a strong coupling between fabric compaction and resin infiltration at low pressures.
The D-SCM process was developed at Fraunhofer ICT with the aim to manufacture sandwich parts in one process step. The idea is to use the expansion pressure of a reactive polyurethane foam system to impregnate the top sheets of a sandwich part. Figure 6.5 shows the D-SCM process with its 7 manufacturing steps. First, the bottom sheet with resin and a thin polymer film is put inside the open cavity. The polymer film is necessary to seal the bottom and top sheets from the reactive polymer foam material that is subsequently placed on top of the bottom sheet. To get a symmetric sandwich, the procedure is repeated for the top sheet. When the heated mold is closed, the foam reaction starts, and the expansion pressure of the foam material leads to an infiltration of the sheets of the sandwich. After the polymer is cured, the sandwich part is demolded. More details about the process development are given by Behnisch et al. [18].

6.2.1 D-SCM Simulation model

The polymer film between the sheets and the reactive foam material acts as a barrier to prevent the foam from infiltrating the sheets. Thus, the expanding foam exhibits pressure on the sheet to compress it and at the same time distributes the resin inside the fabric. The simulation model, therefore, is based on the mold-filling inside a porous medium that is locally compressed by a time-varying pressure. This approach is related to the infiltration simulation

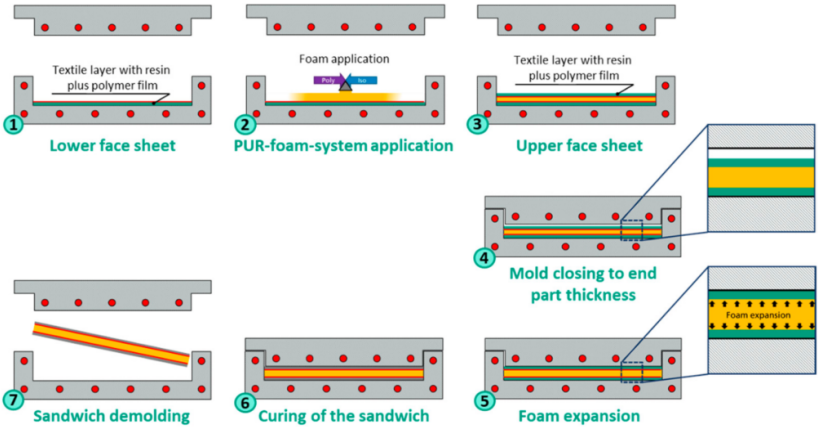

Figure 6.5: The D-SCM process with 7 manufacturing steps [18]; (1) Placement of the lower sheet inside the mold; (2) Application of the reactive polyurethane foam mixture; (3) Placement of the upper sheet inside the mold; (4) Mold closing; (5) Foam expansion and impregnation; (6) Curing; (7) Demolding [18]

in vacuum-assisted resin infusion (VARI), only that the pressure difference between the porous sheet and the exterior is defined by the expanding foam core. It is assumed that the flexural stiffness of the polymer film is very small and thus can be neglected in the simulation model. Furthermore, the resin is assumed to be placed in a circular shape in the center of the isotropic sheet and impregnates it in a radial direction. Consequently, the process can be simulated using a rotationally symmetric model of one of the two sheets. A schematic representation of the simulation model is shown in Fig. 6.6. The mesh consists of 100 elements in the radial direction and two elements in the thickness direction.
To model the process as close as possible to experiments, measured permeability and compaction values for the biaxial carbon fiber fabric are used. The permeability over FVF is shown in Section 5.4.2, Fig. 5.7, and the compaction modulus in Section 5.5.2, Fig. 5.12. Both material parameters are implemented as piecewise linear functions depending on the FVF into the simulation model.

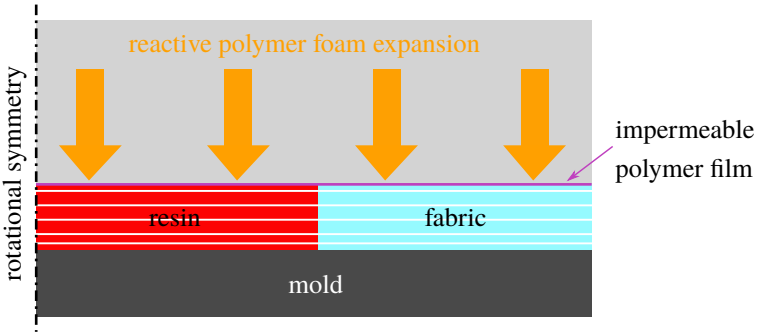

Figure 6.6: Scheme of the D-SCM simulation model using rotational symmetry; the foam expansion pressure acts directly onto the fabric surface that is sealed with a thin polymer film

A time-depending viscosity is implemented by using the isothermal data of the epoxy system R3, given in Section 5.3, Fig. 5.5 and Tab. 5.3.
Besides the compaction modulus, permeability and viscosity, the simulation model parameters are summarized in Table 6.2. A fixed amount of resin is set as the initial condition in the center of the model. The foam expansion pressure rises up to a maximum value of 6.4 bar during the infiltration and is implemented using a time-varying boundary condition in the simulation model. The expansion pressure over time was measured in an empty mold, explained in [18].

6.2.2 D-SCM infiltration results

Figure 6.7 shows the evolution of the resin flow front in a top view of the simulation model. The resin flows in a radial direction and already after 5 s, the flow front increased significantly. Between 20 s and 120 s, the resin infiltrates the remaining sheet. The resin does not fully infiltrate the sheet, as the resin volume was chosen to be a slight amount lower than the total sheet volume to prevent an outflow outside the sheet.

Table 6.2: Simulation model parameters for D-SCM

Parameter	Value	Description
V_{resin}	10.65 mL	resin volume
$r_{\text{resin},0}$	44 mm	initial resin flow front radius
$r_{\text{sheet},0}$	100 mm	plate redius
$h_{\text{sheet},0}$	1.75 mm	initial height
$\varphi_{\text{sheet},0}$	0.2	initial FVF
$p_{\text{foam,max}}$	6.4 bar	maximum foam expansion pressure

To further analyze the impregnation, Fig. 6.8 shows the foam expansion pressure and the simulated resin pressure as well as the filling degree over the simulated time. The graph shows a mold-filling that is very fast in the beginning and slows down until the final state is reached after approximately 120 s. The foam expansion pressure increases during the first 50 s to 6.4 bar, after that the pressure is constant until the end of the simulation. However, the fluid pressure rises only in the beginning parallel to the foam expansion pressure but does not exceed 1.7 bar. After 40 s, the fluid pressure begins to decrease to atmospheric pressure again.

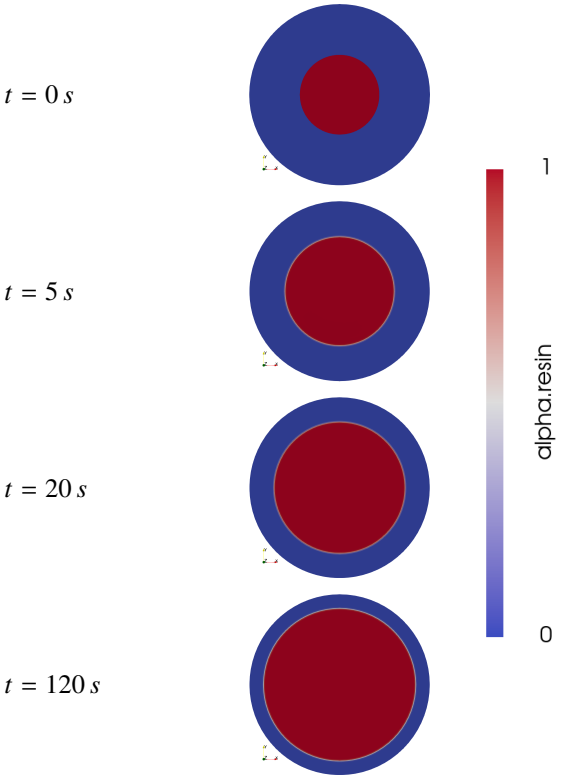

Figure 6.7: D-SCM resin flow front at four time-steps; top view

Figure 6.9 shows the side view of the resin flow front during the infiltration. Again, the four time-steps shown in Fig. 6.7 are visualized. In the initial condition, the fabric is in its initial state, whereas the preform compaction is clearly visible in the next time-steps. At 5 s, also the local deformation of the fabric in the infiltrated part is significant. During the first seconds, the preform gets compacted stronger in the dry part of the sheet than in the infiltrated part, where the fluid pressure builds up an additional resistance against the foam expansion pressure. Already at 20 s, only a slight local deformation in the

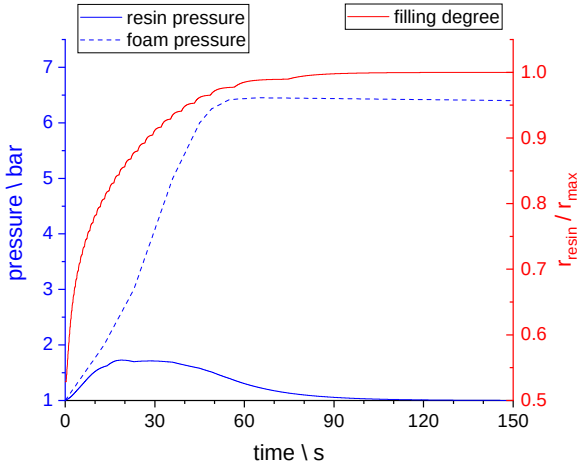

Figure 6.8: D-SCM foam expansion pressure, resin pressure and filling degree over time

impregnated area is visible, whereas the whole sheet is more compacted than before. In the last time-step shown, a stationary final state is reached that is defined by constant compaction throughout the sheet. The final FVF achieved is 0.475.

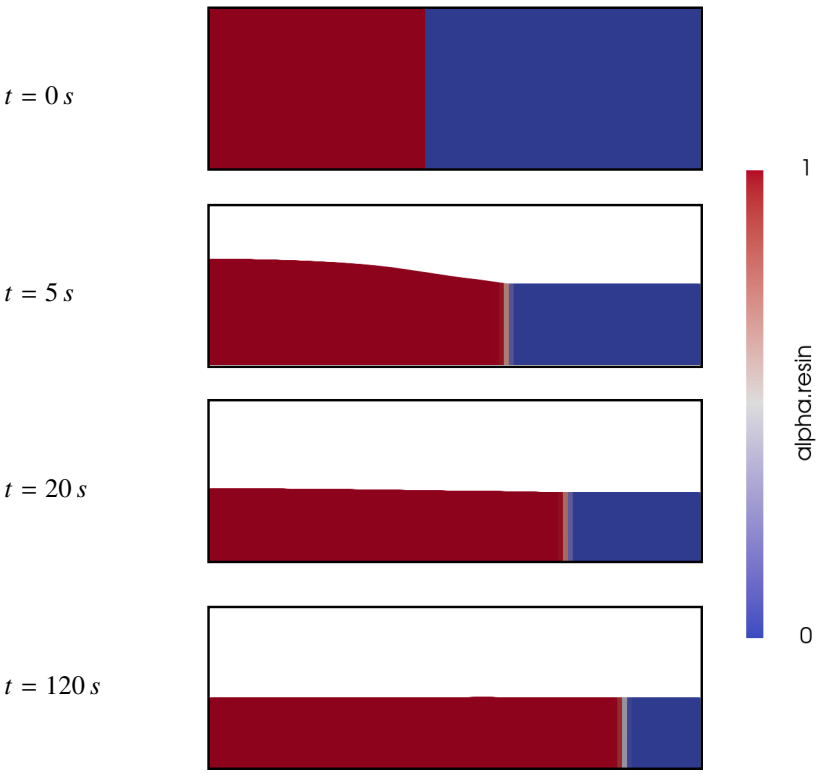

Figure 6.9: D-SCM resin flow front and fabric compaction at four time-steps; radial cross-section view; the radial axis is scaled with a factor of 0.1

6.3 Mold-filling of a sandwich part in RTM with FSI

When manufacturing sandwich parts in RTM, the deforming foam core embedded between the fabrics significantly changes the mold-filling behavior [17, 140, 146]. With the method developed in this work, this reciprocal influence can be modeled and analyzed. In the following sections, first, a sensitivity study is performed to show the influence of the foam core under varying material and process parameters. Subsequently, the model is validated by comparison to RTM manufacturing trials of a sandwich part.
Figure 6.10 shows the geometry of the analyzed sandwich component. The component consists of a trapezoidal sandwich part in the center and two monolithic composite parts at the sides of the component. The inlet and outlet are positioned at the front and back surfaces to distribute the resin homogeneously in the upper and lower layers. The geometric parameters are summarized in Tab. 6.3. The fluid mesh consists of 101 elements along the flow direction and 2 elements in the thickness direction for each sheet. The solid mesh for the foam core consists of linear hexahedrons with an average cell size of 2.5 mm and 100 cells along the flow direction. MntPW!=

6.3.1 Numerical study [2]

In the numerical study, the influence of an embedded foam core on the pressure inside the cavity and onto the flow front propagation is analyzed. The transverse isotropic foam core material properties characterized in Section 5.6.3 are used for this purpose. Using the three different foam core densities at three temperatures leads to nine FSI simulations in total. For comparison, additionally a simulation assuming a rigid core is conducted.

[2] Parts of this section are based on [140]

Table 6.3: Geometry parameters of the FSI sensitivity study and the validation case

Parameter	Value	
L_{cavity}	500 mm	part length
W_{cavity}	240 mm	part width
$H_{\text{cavity},0}$	5 mm	initial fabric height
$H_{\text{cavity,final}}$	2.8 mm	final fabric height
$H_{\text{foam},0}$	20 mm	initial foam core height
$W_{\text{foam,bot},0}$	140 mm	initial foam core width at bottom
α_{foam}	45°	angle at foam core side wall

Simulation model and parameters

As a boundary condition in the simulations, an inlet with a constant mass flow rate is used. Furthermore, symmetry boundary conditions are used along the central plane of the part for the mold-filling as well as for the foam core.

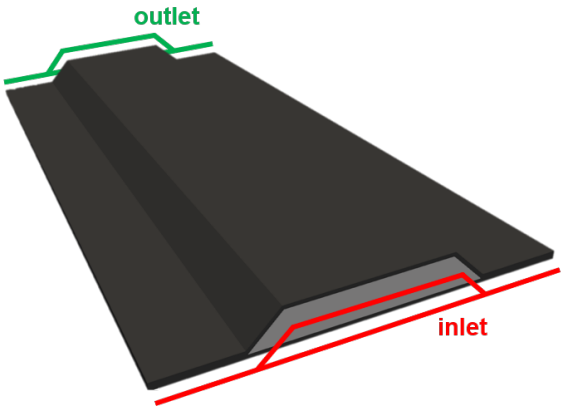

Figure 6.10: Geometry, inlet, and outlet position of the sensitivity study and validation case; fluid part in dark and solid part in light grey

Table 6.4: FSI sensitivity study process parameters

Parameter	Value	Description
$\dot{m}_{\text{inlet}}$	$2\,\text{g}\,\text{s}^{-1}$	inlet mass flow rate
p_{outlet}	1 bar	outlet pressure
μ_{resin}	0.02 Pas	dynamic resin viscosity
φ_{final}	0.5	final FVF
t_{comp}	5 s	mold compression duration

The resin viscosity is set to a constant value and the FVF is designed to be 50% in the final part. Before the injection starts, the part including the foam core is compressed to its final height. The process parameters are summarized in Tab. 6.4.
The permeability and compression modulus of the biaxial carbon fiber fabric is used in the model. The permeability is shown in Fig. 5.7 and the compression modulus in Fig. 5.12.
An implicit coupling scheme with IQN-ILS acceleration is used as also done in the verification case (cf. Section 4.4.2). The parameters are summarized in Tab. 4.4.

Results

Figure 6.11 shows the flow front of the case assuming a rigid core after 25 s simulated time, which is approximately at a cavity fill grade of 50%. In the visualized top view, the upper part shows the monolithic part, whereas the center coincides with the foam sidewall and the lower part shows the top sheet above the foam core. Because the permeability is constant in the whole domain and the resin is distributed at the inlet over the whole width, the flow front has a linear shape.

Table 6.5: FSI sensitivity study coupling methods and parameters; details of the methods are given in [144]

Parameter	Method / Value
time-step	0.01 s
mapping method	RBF thin plate splines
coupling scheme	parallel implicit
maximum iterations	50
implicit acceleration scheme	IQN-ILS
initial relaxation	0.1
preconditioner	residual-sum
filter	QR1, 1×10^{-7}
maximum IQN-ILS iterations	50
time-steps reused	25
convergence measure $\Delta\mathbf{d}$	1×10^{-7} m (abs.)
convergence measure F	1×10^{-4} N (abs.)

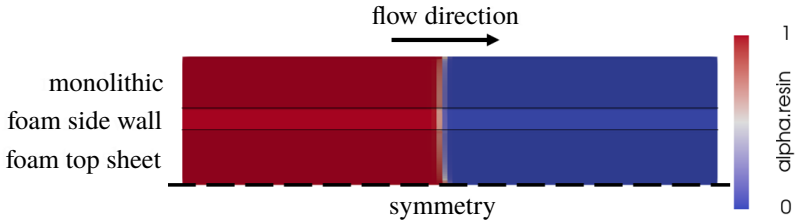

Figure 6.11: Flow front after 25 s of the rigid sandwich case

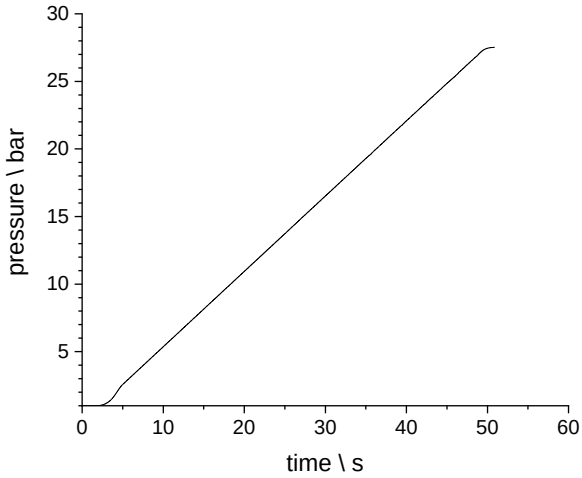

Figure 6.12: Injection pressure over time assuming a rigid foam core

In Fig. 6.12, the pressure at the inlet is plotted over the simulated time. After the compression stage until 5 s, the pressure increases linearly until the maximum value of 27.5 bar is reached and the cavity is completely filled after 50 s. The pressure increase is explained by the Darcy-like flow behavior with a constant velocity, which leads to a constant pressure gradient and consequently to a linear pressure increase.

For the simulations containing compressible foam cores, also the flow front shapes and the pressures at the inlet are analyzed. Figures 6.13, 6.14 and 6.15 show the flow fronts after 25 s for the cases with foam core densities of 80 g L^{-1}, 100 g L^{-1} and 130 g L^{-1}, respectively. When comparing the flow front shapes of Fig. 6.13, it is obvious that the foam core influences the mold filling behavior. A higher temperature signifies a softer core material and leads to a more inhomogeneous flow front. The inhomogeneity results from a higher flow velocity at the inclined foam core sidewalls. A higher temperature leads to a softer foam core and following to a higher foam core deformation, especially in the transverse isotropic plane. This directly results in higher permeabilities

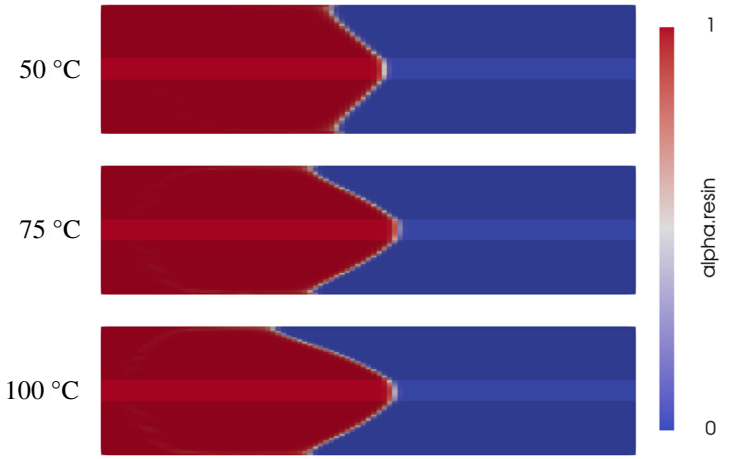

Figure 6.13: Flow front after 25 s for three temperatures with a foam core density of 80 g L^{-1}

Figure 6.14: Flow front after 25 s for three temperatures with a foam core density of 100 g L^{-1}

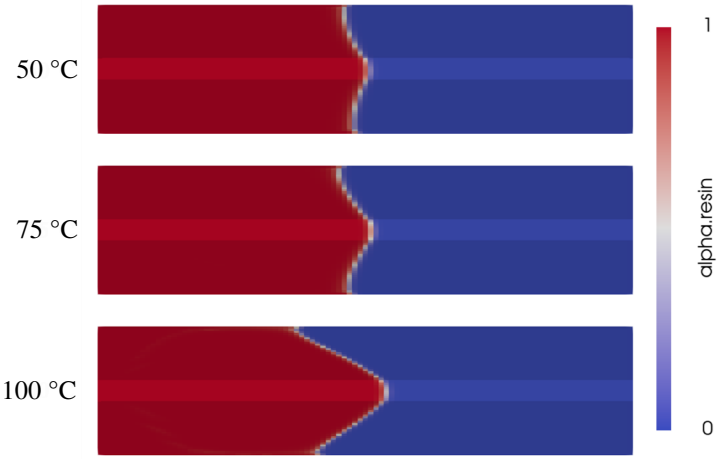

Figure 6.15: Flow front after 25 s for three temperatures with a foam core density of 130 g L^{-1}

at the sidewalls and leads finally to the faster resin flow here. For the foam densities of 100 g L^{-1} and 130 g L^{-1}, the same effect is visible, though it is less strongly developed. The flow front for a foam core with 130 g L^{-1} (Fig. 6.15) has only slight inhomogeneities for temperatures of 50 °C and 75 °C, whereas for 100 °C, also a strong acceleration of the resin flow at the foam sidewalls exist. This is a result of the decreasing foam core compression modulus in the transverse isotropic plane from 75 °C to 100 °C (cf. Tab. 5.10).

To further analyze this, the deformation of the cavity is visualized at three different cut planes of the simulation model. The first cut is positioned at the inlet position, the second cut is in the center of the component and the third cut is located at the outlet. The cut positions are visualized in Fig. 6.16.

Figure 6.17 shows the outlines of the cavity during the mold-filling for the case with a foam core density of 80 g L^{-1} at 100 °C, which is the case having the highest deformations. The colors of the outlines are the same as given in Fig. 6.16, the grey color indicates the non-deformed cavity. Six time-steps are

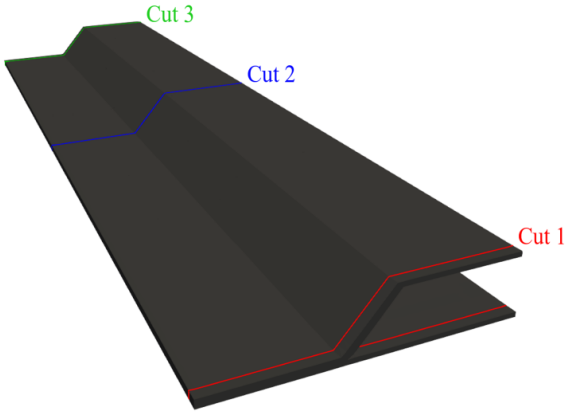

Figure 6.16: Position of three cut planes for visualization of the local foam core and cavity deformations

analyzed for increasing times from top left to bottom right. After 5 s, only a deformation at the first cut near the inlet (red) exists, while at the two other cuts, only a small deformation is visible. This is also the case for 15 s and 25 s, while the deformation at the first cut is still increasing. After 35 s, suddenly the second cut (blue) also shows a large deformation, which indicates that the part of the mold is now filled with resin and the fluid pressure rises also in the center of the mold. This is furthermore shown in Fig. 6.18, where the pressure field after 25 s and 35 s is visualized. At the central cut (blue), the pressure is still low after 25 s and just increases in the sidewall region. After 35 s, the pressure in the sidewall at the central cut did already increase to approximately 1.6 bar. Additionally to the flow front behavior and the deformation characteristics, also the injection pressures are compared. Figure 6.19 shows the inlet pressures for all 9 analyzed cases. The pressure increases at the inlet during injection, though the pressure level reached is significantly lower for all FSI cases compared to the case assuming a rigid core (cf. Fig. 6.12), where the pressure rises up to 27.5 bar. Even for the stiffest foam core (130 g L^{-1}, 50 °C), the pressure stays

below 7 bar during mold-filling. For the softest core material investigated in this numerical sensitivity study (80 g L^{-1}, 100 °C), the pressure just reaches 2 bar. The graph shows that for all cases, the inlet pressure decreases with increasing temperature and decreasing foam core density.

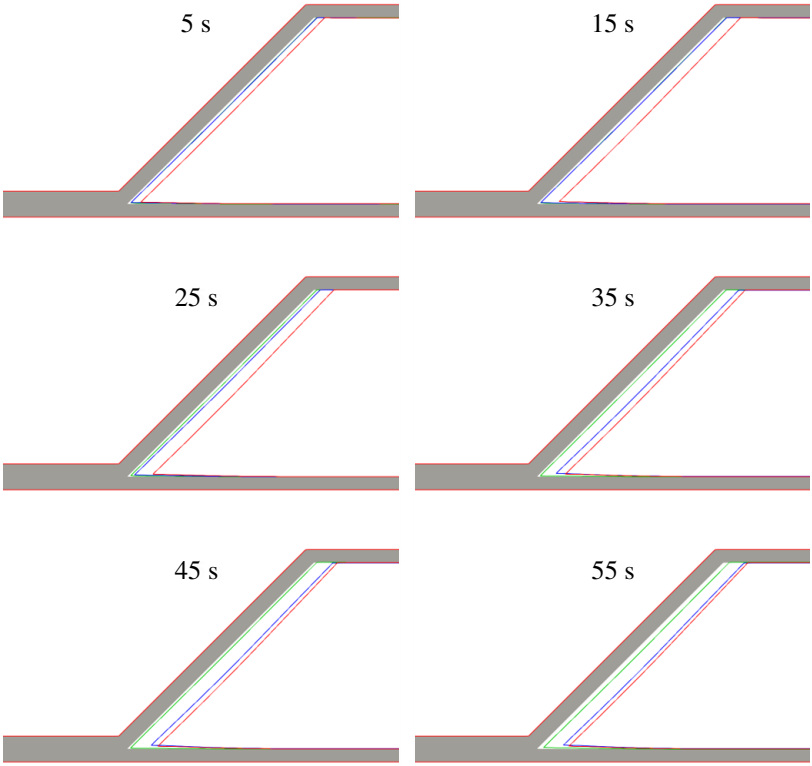

Figure 6.17: Outlines of the cavity at the three cuts from Fig. 6.16 for six time-steps of the case with a foam core density 80 g L^{-1} at 100 °C

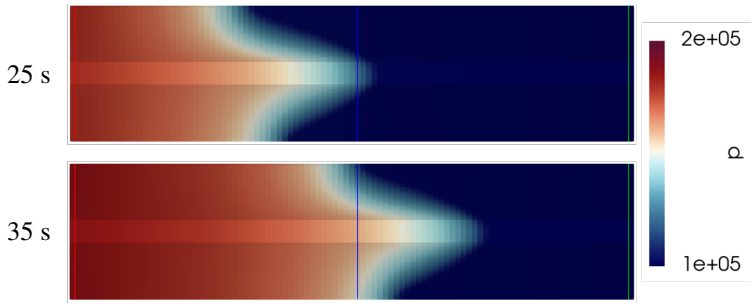

Figure 6.18: Pressure field at two time-steps of the case with a foam core density 80 g L^{-1} at 100 °C

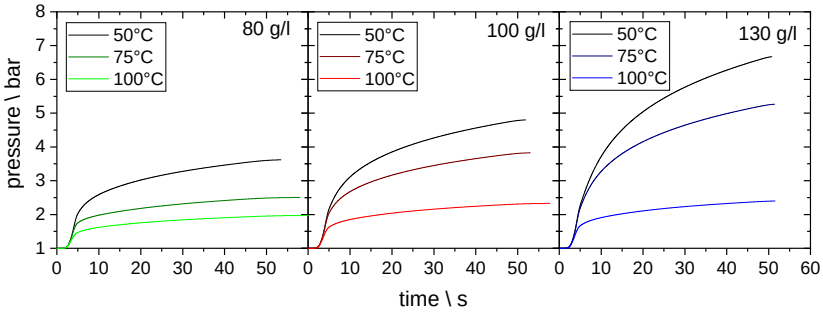

Figure 6.19: Injection pressure for three temperatures of the foam core with 80 g L^{-1} (left), 100 g L^{-1} (middle) and 130 g L^{-1} (right)

6.3.2 Experimental validation

The experimental validation is carried out by comparing mold-filling simulations to RTM trials of the sandwich geometry shown in the previous section in Fig. 6.10. Details about the RTM tool, the integrated sensors, as well as the materials and the simulation model, are given in the next sections.

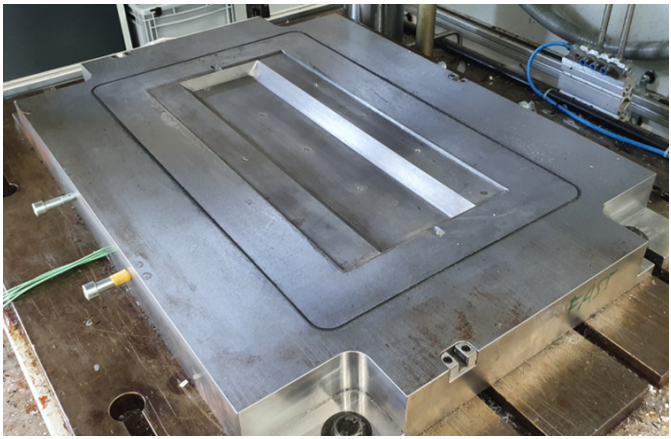

Figure 6.20: RTM tool for sandwich manufacturing; the sandwich geometry is milled out of the lower mold

RTM tool and experimental setup

An RTM tool made of steel is designed for the RTM trials. It consists of an upper and a lower part, whereas the upper part contains only the inlet and outlet connections. The cavity is embedded into the lower part, to ease demolding and to guarantee that inlet and outlet are located at the highest points of the cavity. Figure 6.20 shows the lower part of the tool. In the middle of the tool, the trapezoidal geometry of the sandwich is visible that is embedded upside down into the tool. The tool is mounted in a hydraulic press (Maschinenfabrik Lauffer GmbH & Co.KG, max. 4000 kN).

To measure the cavity pressure during mold-filling, several pressure sensors (Kistler Instrumente GmbH, type 6161AA) are included in the RTM tool. The sensors are embedded with a slight offset to the mold surface to measure only the fluid pressure and not the compaction force of the fabric. The locations of the pressure sensors are visualized in Fig. 6.21. Five sensors p_1 to p_5 are embedded into the lower mold, whereas sensor p_6 is implemented in the upper mold. The sensors p_2 and p_3 are located at a distance of 125 mm to the inlet

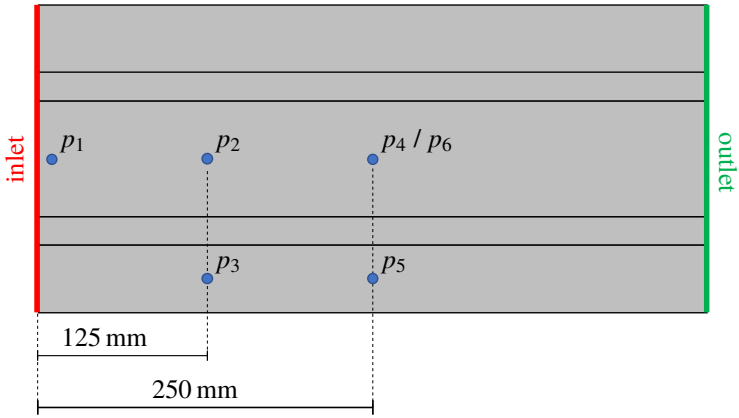

Figure 6.21: Pressure sensor positions in the RTM tool; all sensors except for p_6 are located in the lower mold part

and the sensors p_4 to p_6 have a distance of 250 mm. The sensor p_1 is located close to the inlet and is used to measure the injection pressure directly in the mold. The sensors p_3 and p_5 are located in the monolithic part besides the foam core. All other sensors are in the sandwich part of the component. The data acquisition is done using a data amplifier and DASYLab® software by National Instruments.

A mixing head by Tartler GmbH is used to inject the resin system (Sika® Biresin® CR170/CH150-3, "R2") at a constant mass flow rate or mixing head pressure. The injection is stopped manually when the first resin is visible at the outlet.

The process parameters for the validation experiments are summarized in Tab. 6.6. The cases use a constant mass flow rate at the inlet. For the case with a foam density of 130 g L^{-1}, for safety reasons a pressure limit of 5 bar is set in the mixing head to prevent the formation of very high pressures in the polymer hoses between the mixing head and the RTM tool. The experiments are repeated at least three times for each configuration.

Table 6.6: FSI validation case parameters; p_{inlet} is only used with 130 g L^{-1} foam cores

Parameter	Value	Description
T_{resin}	60 °C	resin mixing temperature
T_{mold}	75 °C	mold temperature
q_{inlet}	140 g min^{-1}	inlet mass flow rate
p_{inlet}	5 bar	inlet pressure
p_{outlet}	1 bar	outlet pressure

Simulation model

The viscosity of the epoxy resin system R2 is modeled with the Grindling kinetic model and the Castro-Macosko rheology model. The data is given in Section 5.3, Tab. 5.2. The permeability of the UD carbon fiber non-crimp fabric is given in Section 5.4, Fig. 5.8. A symmetric layup (0° | 90° | 90° |0°) is chosen for the bottom and top sheets. In the model, the permeability measurements for flow parallel and transverse to the roving orientation are volume averaged, which results in an isotropic permeability of the layup. Furthermore, the characterized compaction data of the UD carbon fiber fabric is used, as given in Section 5.5, Fig. 5.11. The compaction characterization is carried out using the same layup as in the RTM experiments.
Besides the different material and process parameters, the same simulation model as described in the previous Section 6.3.1 is used.

Experimental results

Figure 6.22 shows one manufactured sandwich part. The part is cut in a vertical direction to visualize the foam core deformations. The carbon fabrics are visible as black top and bottom layers. Between them, the polymer foam core is visible in bright color. The cut part is completely infiltrated without visible dry areas.

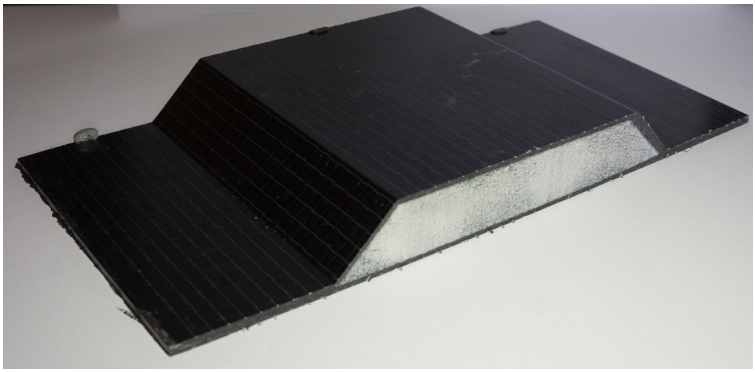

Figure 6.22: RTM sandwich part manufactured in the validation experiments. The part is cut for visualization of the foam core deformation

In Fig. 6.23, two details of the cut cross-section are shown. Figure 6.23 a) shows the left sidewall with the infiltrated carbon fabrics in black and the foam core in light gray color. The foam core shows no large deformation, which is indicated by the nearly constant top and bottom layers. On the contrary, Fig. 6.23 b) shows the right sidewall of the part where deformation of the foam core is visible. The thickness of the top layer at the sidewall is larger than in Fig. 6.23 a), which indicates a compression of the foam core mostly in the horizontal direction.

As can be seen, the horizontal compression is not equally at the left and right sidewalls. This effect is supposed to result from a non-symmetric mold-filling, which originates from a race-tracking at one side of the mold. A faster mold-filling at one side of the part leads to increased pressure at that side. Subsequently, the foam core is compressed stronger to the opposite sidewall, which leads to the observed asymmetric compression. Hence, the foam core is in the beginning in a symmetric position in the center of the fabrics, which changes to an unstable state when mold-filling starts. However, further experiments are necessary to better understand and verify this observed behavior.

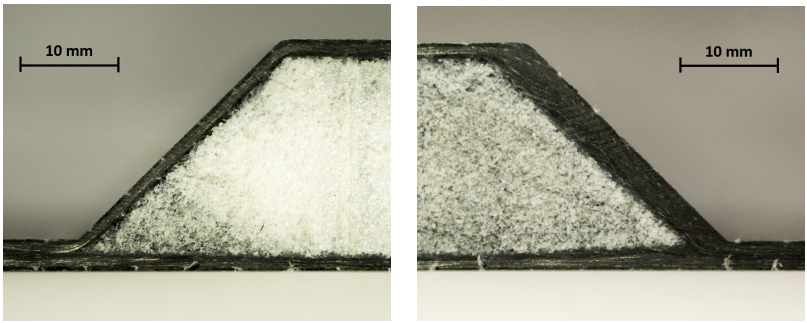

a) b)

Figure 6.23: Detailed view of a cut through a manufactured sandwich part; a) left side; b) right side

Figures 6.24 to 6.26 show the pressure data of the integrated sensors for three parts containing a foam core with a density of 80 g L^{-1}, 100 g L^{-1} and 130 g L^{-1}, respectively. It should be noticed that the pressure data of the sensors shows the relative pressure above ambient pressure. The pressure data is synchronized using the first increase of sensor p_1 to indicate the start of the injection. The point in time when the pressure at a sensor starts to increase implies that the flow front reaches the sensor position at that time.

In all experiments, the same trend is visible. After the pressures increase at sensor p_1, the pressures at the sensors p_2 and p_3 start to rise. Finally follow the sensors p_4, p_5, and p_6. This matches the distance of the sensors to the injection gate (cf. Fig. 6.21) and, thus, confirms an overall infiltration direction along with the foam core. In a rigid mold without race-tracking, sensors p_2 and p_3 should rise at the same time, as well as p_4, p_5, and p_6. The end of the injection is indicated at the time when the pressure of all sensors starts to decrease.

In Fig. 6.24 (foam core density 80 g L^{-1}), the pressure of sensor p_1 increases nearly linearly to a value of 2.5 bar and then stays closely to this value until the end of the injection. Between 45 s and 60 s the sensors p_2 and p_3 start to

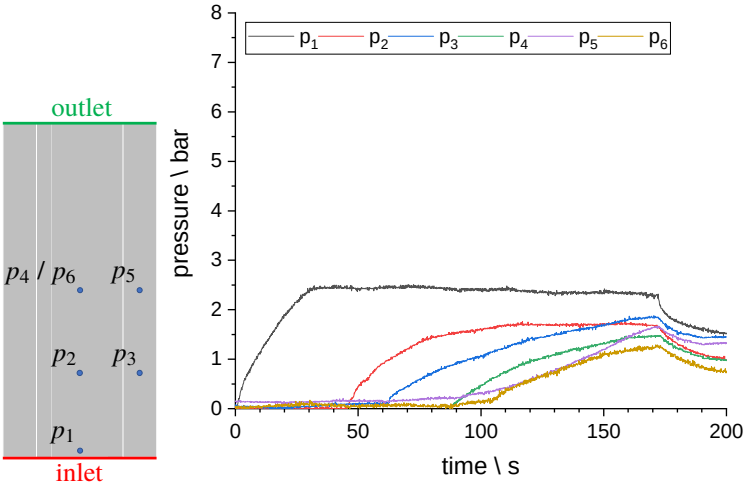

Figure 6.24: Raw pressure data of one experiment with a foam core density of 80 g L^{-1}

increase. After approximately 90 s to 105 s, the sensors p_4, p_5, and p_6 show an increasing pressure. After 170 s the injection is stopped.

Figure 6.25 shows the pressure data results for one experiment with a foam core density of 100 g L^{-1}. Again, the pressure of sensor p_1 increases nearly linearly but to a higher value compared to Fig. 6.24. Sensor p_1 rises to a value between 4 bar and 5 bar and then stays in this range until the end of the injection. Between 30 s and 40 s the sensors p_2 and p_3 start to increase. After that, the sensors p_4, p_5, and p_6 increase between approximately 70 s and 90 s. Again, after approximately 170 s the injection is stopped.

In Fig. 6.26, the pressure data results for one experiment with a foam core density of 130 g L^{-1} are shown. Equal to the graphs shown before, the pressure of sensor p_1 increases nearly linearly to a value of approximately 3 bar and then stays in this range until the end of the injection. Between 30 s and 50 s the sensors p_2 and p_3 start to increase. After that, the sensors p_4 and p_6 increase at approximately 60 s. The sensor p_5 increases only after 130 s. After approximately 150 s the injection is stopped.

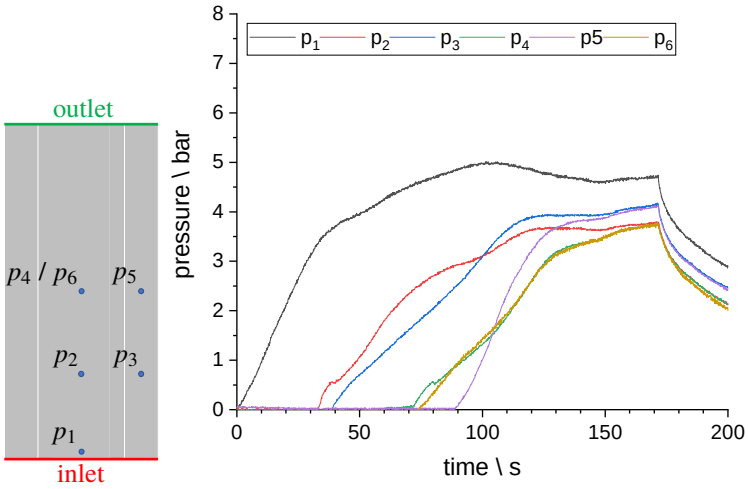

Figure 6.25: Raw pressure data of one experiment with a foam core density of 100 g L^{-1}

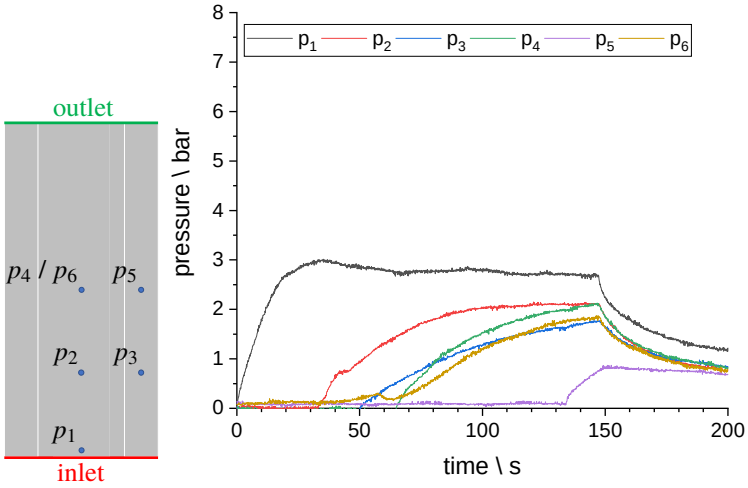

Figure 6.26: Raw pressure data of one experiment with a foam core density of 130 g L^{-1}

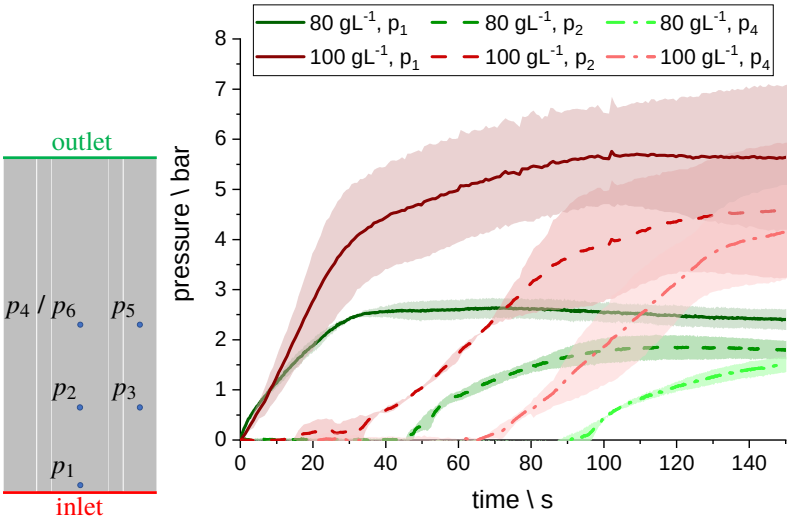

Figure 6.27: Average pressure data of the experiments with a foam core density of 80 g L^{-1} and 100 g L^{-1} for the sensors p_1, p_2, and p_4

As it is difficult to analyze the raw pressure data, Fig. 6.27 shows the average pressure of the three sensors located at the center-line (p_1, p_2, and p_4) for the cases of 80 g L^{-1} and 100 g L^{-1} foam core density that both use a constant injection mass flow rate. Here, the influence of the embedded foam core on the pressure evolution is clearly visible. The pressure level for all three sensors is significantly lower for the case with a foam core density of 80 g L^{-1} where it reaches only approximately 2.5 bar. For the experiments with a foam core density of 10 g L^{-1}, the pressures are nearly doubled to more than 5 bar at the inlet. Moreover, the standard deviation of the pressures is lower for the case of 80 g L^{-1} foam core density.

To further compare the influence of the foam core onto mold-filling, the moments when the flow front reaches the sensors are compared. Figure 6.28 shows the averaged times and their standard deviations when the resin flow front reaches the sensors p_2 to p_6 for the three analyzed foam core densities.

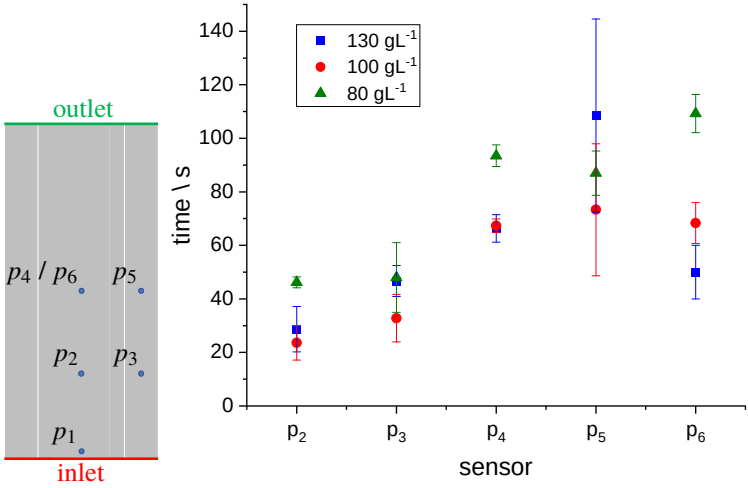

Figure 6.28: Average time for reaching the sensors p_2 to p_6; sensor p_1 is used for time synchronization

Sensor p_2 and p_3 have the lowest filling times, whereas sensors p_4 to p_6 have higher filling times. For all sensors except p_5, the mold-filling with a foam core of $80\,\mathrm{g\,L^{-1}}$ have the highest average filling times. Furthermore, this case has the lowest standard deviations. Compared to sensor p_2, sensor p_3 shows higher standard deviations for all cases. Besides that, also sensor p_5 has a higher standard deviation than sensors p_4 and p_6 in the same case. The higher standard deviation of the sensors at the monolithic sides of the part indicates a race-tracking at the edges of the part, which occurs not in each experiment and, thus, leads to the high scattering observed in filling times.

In addition to the pressure and time data, also the weight of three manufactured parts is analyzed. Therefore, the parts are cut into 4 sections that are visualized in Fig. 6.29. Each of the cut parts is weighted and the density is calculated with the designed volume of the part assuming a completely closed mold. The parts cut are the same that are used to visualize the raw pressure data in Fig. 6.24 to 6.26.

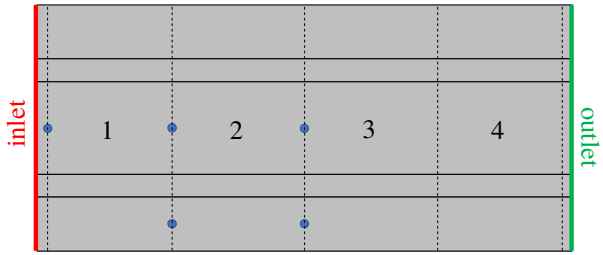

Figure 6.29: Sizes of four cut sections of the sandwich part used for part density analysis

The results of the calculated densities are visualized in Fig. 6.30 as points. In addition, the nominal weight of the parts is indicated by the colored lines for the three foam core densities. Not the part with a foam core density of 130 g L^{-1} but the part with a foam core density of 100 g L^{-1} exhibits the highest average density of 540 g L^{-1}. The average densities of the two other parts are nearly equal at around 475 g L^{-1}. This behavior can be explained with the lower injection pressure of the part with 130 g L^{-1} foam core density (limited to 5 bar) that led to a lower compression of the foam core in that case.

Simulation results and comparison to experiments

To compare the results of the experiments with the simulations, first, the pressure evolution at sensor p_1 that is located close to the inlet is analyzed for the first 60 s. Therefore, Fig. 6.31 shows the results of the simulations and the average experimental data with a foam core density of 80 g L^{-1} and 100 g L^{-1} (cf. Fig. 6.27). The time axes are synchronized using the first increase of the pressure at sensor p_1. The figure shows the simulated pressure for two temperatures: 50 °C and 75 °C. Both simulations and experiments show that the pressure level is lower for the lighter foam core material, which was also the result of the numerical study in Section 6.3.1. The experimental pressure increases slower in the first 30 s compared to the simulations, but then slows down and stays in between the simulated pressures for the two temperatures. The results show a

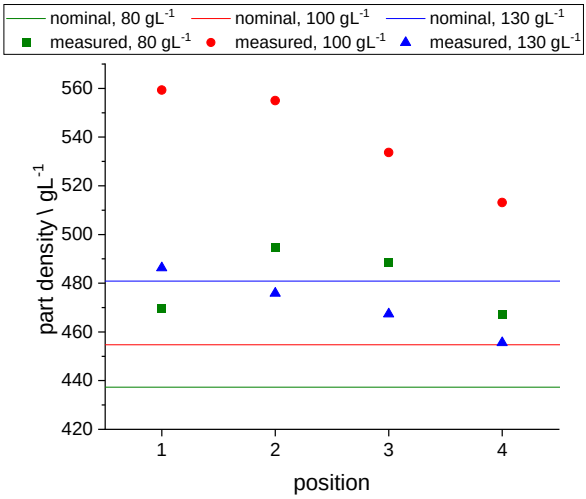

Figure 6.30: Densities of four cut sections of three parts with different foam core densities; parts conform to the raw pressure data of Figures 6.24 to 6.26

comparable pressure increase for the experiments and the simulations, though especially in the first 20 s, a difference is evident. The difference of the pressure increase can be explained by a race tracking along the edges, which leads to a slower mold-filling inside the fabric. By comparing the time points, when the flow front reaches the sensors, this is further analyzed.

Figure 6.32 shows the simulated and experimentally measured time points when the flow front reaches the sensors p_2 to p_6. In the case with a foam core density of 80 g L^{-1}, the flow front reaches the sensors p_2 and p_3 after 30 s to 50 s and the sensors p_4 to p_6 between 55 s and 110 s. In the experiments, the flow front is slower than predicted in the simulations, especially when comparing the sensors p_4 to p_6. The simulation results with a foam core density of 100 g L^{-1} show a faster mold filling compared to the results with 80 g L^{-1} and are close to the measured values for all sensors. The simulated time points for the case with 130 g L^{-1} show a very good agreement for the sensors p_2 and p_3, whereas the results for the sensors p_4 to p_6 show a high difference of the simulations

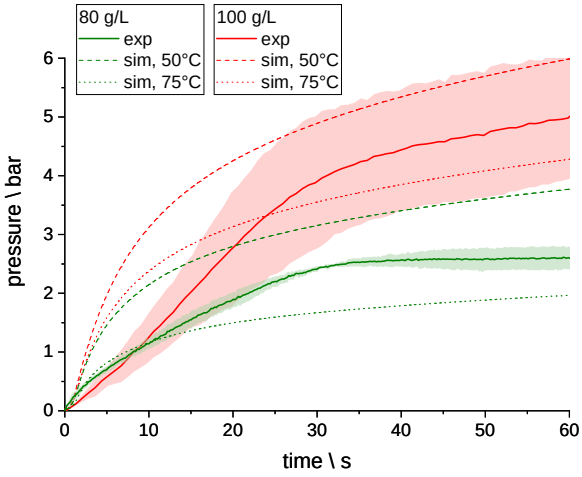

Figure 6.31: Comparison of the pressure at sensor p_1 for the simulations and the experiments with a foam core density of $80\,\mathrm{g\,L^{-1}}$ and $100\,\mathrm{g\,L^{-1}}$

and the experiments. Different from the other two cases, the predicted times are higher than the experimentally measured times.

The injection in the first two cases ($80\,\mathrm{g\,L^{-1}}$ and $100\,\mathrm{g\,L^{-1}}$) uses a constant resin flow rate to infiltrate the fabric. Therefore, differences in the simulated and measured times for reaching the sensors depend only on differences in the cavity volume or in a non-homogeneous filling of the mold but not on the permeability of the fabric. In the third case ($130\,\mathrm{g\,L^{-1}}$), the injection uses a constant pressure and, thus, the infiltration times depend furthermore on the permeability of the fabric, which is very sensitive to changes in FVF.

Figure 6.33 shows the simulated and measured pressures at the end of the injection for the three sensors p_1, p_2 and p_4 that are located at the center-line of the cavity and, thus, are less influenced by race-tracking at the edges. For all three cases, the pressure of the simulations using a foam core temperature of 75 °C are in very good agreement with the experiments. Only for sensor p_4 at $130\,\mathrm{g\,L^{-1}}$, the simulated pressure is slightly lower than the measured pressure.

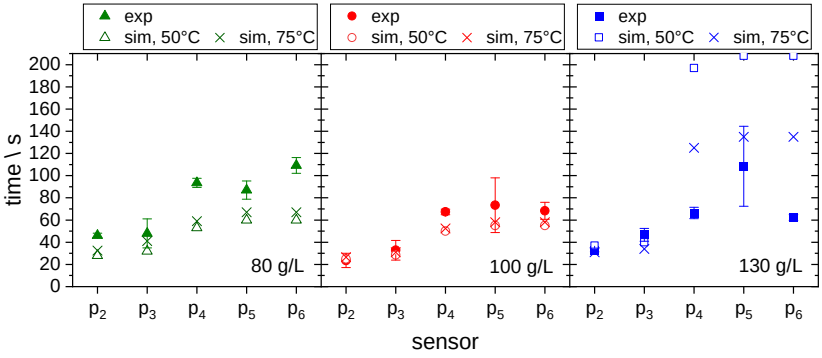

Figure 6.32: Comparison of the points in time when the flow front reaches the pressure sensors for the simulations and the experiments with a foam core density of 80 g L^{-1}, 100 g L^{-1} and 130 g L^{-1}

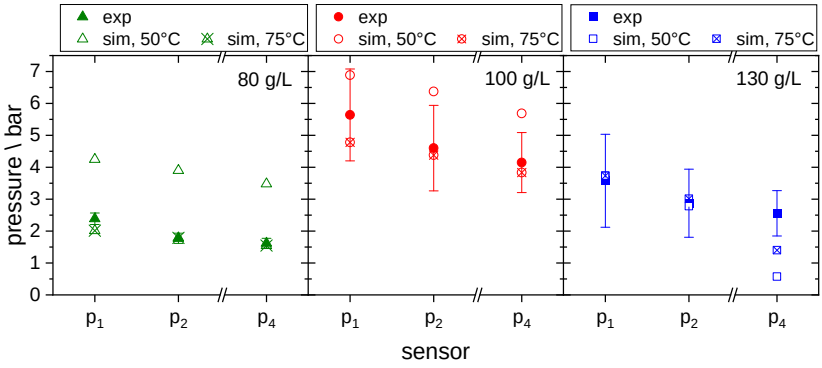

Figure 6.33: Comparison of the pressure at p_1, p_2 and p_4 at the end of the injection for simulations and experiments with a foam core density of 80 g L^{-1}, 100 g L^{-1} and 130 g L^{-1}

The simulated pressure assuming a foam core temperature of 50 °C is higher compared to the experiments in the first two cases (80 g L^{-1} and 100 g L^{-1}). This indicates that the foam core temperature at the end of the injection reached the mold temperature of 75 °C and, thus, leads to a good agreement to the simulations assuming that constant temperature.

6.4 Discussion

Three application examples show possible applications of the developed methods. The first example shows mold-filling simulations of PC-RTM with included preform compaction by using the RTM mold-filling simulation method in combination with the poro-elasticity solid mechanics method for the fabric compression. Instead of just using the fluid pressure as the control value, now the total stress in the vertical direction is used, which is the sum of the compaction stress of the fabric and the fluid pressure. When comparing the simulation results to prior simulations that use only the fluid pressure without the compaction force of the fabric [32], the predicted maximum mold gap height is higher and the mold closing speed is lower (cf. Fig. 6.2 to 6.4), which is a direct result from the fabric compaction. Furthermore, the results of the simulations are validated by comparison to experimental PC-RTM trials. Therefore, the mold gap height and the pressure at the injection gate are measured during RTM experiments of a rectangular plate. The comparison of the simulations and the experiments show an excellent agreement for the predicted mold gap height, especially for initial mold gaps of 0.1 mm and 0.3 mm. Hence, the newly developed method enables a more precise prediction of the final part height and mold-filling times of PC-RTM. The results with a large initial mold gap of 0.7 mm show a difference between simulations and experiments in the pressure increase at low FVF. This emphasizes the need for more accurate permeability data at low FVF, which is difficult to obtain using the state-of-the-art methods. The application example of D-SCM is given to show the applicability of the developed method to infiltration processes that have at least one flexible part surface during infiltration. This is not only the case in D-SCM, but also in VARI process types where one side of the fabric is covered by a thin polymer film. In addition to VARI, D-SCM possesses a time-varying compaction pressure that is resulting from an expanding foam core. The D-SCM process simulation reveals the principal characteristics of the D-SCM process. Most of the infiltration takes place in the first seconds when the foam expansion pressure builds up.

Already after 30 s, more than 90% filling is achieved, whereas the remaining 10% need up to 120 s (cf. Fig. 6.8). This is a result of two important properties. The first is the increased viscosity due to the beginning curing reaction of the polymer matrix that leads to decreasing flow velocities during the infiltration. The second and even more important property is the permeability that depends strongly on the FVF and, thus, on the compaction state of the fabric. During the infiltration, the permeability decreases by more than one order of magnitude, which leads to a significantly higher drag force onto the resin. A combination of low viscosity, high permeability, fast-rising foam expansion pressure, and high fabric bulk modulus leads to the fastest infiltration and facilitates a complete infiltration of the part.

To show the capabilities of the FSI method for mold-filling in RTM with embedded foam cores, first, a numerical sensitivity study is carried out. The study is carried out to reveal the influence of an embedded foam core on mold-filling for a full-size RTM part. The geometry is the same that is also used in the validation experiments. The simulations show that the cavity pressure is heavily influenced by the embedded foam core. Even for the stiffest foam core, the pressure decreases from 27.5 bar to under 7 bar at the end of the mold-filling. A rigid mold leads to a linear pressure increase throughout the mold-filling, whereas the foam core leads to a slower, non-linear increase. The foam properties in turn are strongly dependent on its density and temperature. For softer core materials, the pressure reaches a nearly constant level at very low pressures of approximately 2.5 bar, which is less than 10% of the pressure assuming a rigid mold.

Due to the anisotropy of the foam core a softer mechanical behavior transverse to the thickness direction, the foam core compression is especially high in the horizontal plane, whereas in the thickness direction, nearly no deformation is present (cf. Fig. 6.17). Compression of the foam core leads directly to decompression of the fabric and thus decreases the FVF. As the deformation is depending on the foam core geometry and, furthermore, has an anisotropic behavior, this leads to a more inhomogeneous flow front. In regions with

high foam core compression, the flow front is accelerated. In summary, the numerical sensitivity study of the RTM mold-filling with an embedded foam core and a constant mass flow rate inlet leads to the following relationships:

- The softer the foam core, the slower the mold-filling.
- The softer the foam core, the lower the cavity pressure.
- The softer the foam core, the higher the part weight.
- The higher the pressure, the higher the part weight.

For an infiltration with constant injection pressure, the same relationships are valid, except for the mold filling time. Hence, for a constant injection pressure applies:

- The softer the foam core, the faster the mold-filling.
- The softer the foam core, the lower the cavity pressure.
- The softer the foam core, the higher the part weight.
- The higher the pressure, the higher the part weight.

This can be explained by the fact that a soft foam core leads to lower FVF and, thus, to less porous drag, which results in a faster injection when the pressure is constant.

RTM infiltration experiments with the foam core material at three different densities confirm the results of the sensitivity study. Embedding the softest foam core material with a density of $80\,\mathrm{g\,L^{-1}}$ increases the mold filling time when a constant resin mass flow rate is used. Furthermore, the pressure level and the standard deviation are significantly lower for the experiments with a foam core density of $80\,\mathrm{g\,L^{-1}}$ compared to $100\,\mathrm{g\,L^{-1}}$ (cf. Fig. 6.33). The higher standard deviations for higher foam core densities are also visible in points in time when the flow front reaches the sensors p_3 and p_5 (cf. Fig. 6.28. As the scatter in mold-filling times indicates race-tracking along one side of the mold, this leads to the presumption that higher foam core densities facilitate the formation of race-tracking. This is fortified by the observations made in a mold-filling study, where the injection is stopped at the moment when the flow front reaches sensor p_5. Figure 6.34 shows the result of a mold-filling study of

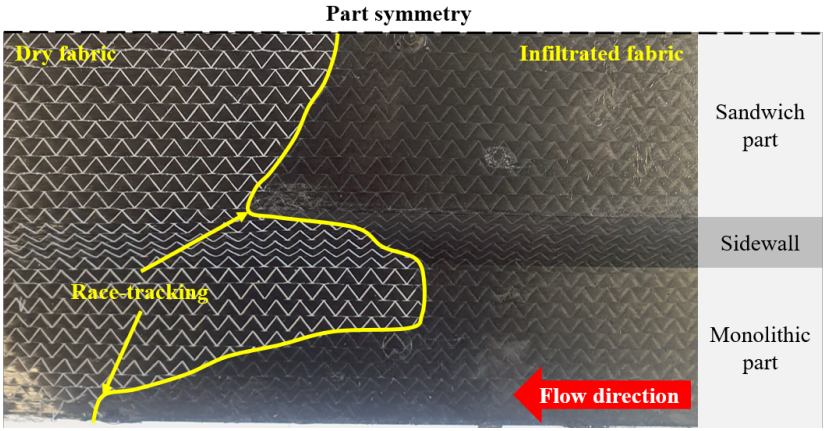

Figure 6.34: Flow front in a half-filled cavity of an experiment with a foam core density of 130 g L^{-1}

a sandwich part with a foam core density of 130 g L^{-1}. At the lower part edge, a significant race-tracking is present, which is represented by the advanced flow front. Moreover, a smaller race-tracking effect is present at the edge of the inclined sidewall towards the sandwich part.

The race-tracking can happen at only one side of the cavity, which leads to losing the symmetry plane at the center-line of the part. The high standard deviations of the time when sensor p_3 and especially sensor p_5 is reached (cf. Fig. 6.28 also result from occurring race-tracking at one side of the part. Moreover, the foam core is compressed towards one sidewall, which leads to a further increase of the asymmetric flow that results in different sidewall thicknesses like shown in Fig. 6.23. This effect of unstable symmetry has to be further analyzed in future work by experiments and by numerical simulations with the method developed in this work.

The densities of the manufactured parts do not show the theoretical trend of higher weights for larger foam core densities (cf. Fig. 6.30). Instead, the weight is not constant along the foam core but shows a decreasing trend along the flow

path. This is explained by the influence of the fluid pressure on the foam core compression, which leads to an increased sheet thickness and consequently to a larger amount of resin in those areas. Furthermore, it is evident that the part densities are also affected by processing conditions. The part with a foam core density of 130 g L^{-1} has a lower weight than the part with a foam core density of 100 g L^{-1}, which is explained by the lower cavity pressure during mold-filling (cf. Figs. 6.25 and 6.26).

The simulation results show the same trends that are observed in the experiments: The pressure is lower and the mold-filling times higher for softer core material and a constant injection flow rate. Furthermore, the pressure level at the end of the injection shows a very good agreement between the simulations assuming a temperature of 75 °C and the experiments (cf. Fig. 6.33) that are conducted with a mold temperature of 75 °C. The experiments, therefore, validate the simulation methods and the simulation model for these two statements. However, the exact pressure evolution during mold-filling is difficult to predict. The characterization uncertainties decrease the accuracy of the simulations, especially because several non-linear material parameters (permeability, foam core modulus, resin viscosity) interact with each other.

Furthermore, the resin viscosity and the foam core modulus depend on the temperature, which is assumed to be constant in the simulations but shown to have a significant impact on the mold-filling (cf. Fig. 6.19). Consequently, the unknown foam core density additionally influences the accuracy of mold-filling simulations.

Additionally, edge-effects like race-tracking lead to a less homogeneous flow-front in the experiments. To better predict these effects, not only at the outer edge but also at the edges of the foam core sidewalls, a combination of draping simulations that include the fabric compression and mapping of the resulting fabric thickness to the mold-filling simulation model can improve the accuracy of the mold-filling simulations.

7 Conclusions

The aim of this thesis is to develop and validate a numerical method to simulate mold-filling in Resin Transfer Molding (RTM) with fluid-structure interaction (FSI). Therefore, several methods are developed and combined to capture the FSI during mold-filling. The foundation of the simulation method is a volume of fluid (VoF) two-phase flow simulation based on finite-volume (FV) discretization (cf. Section 3.2). The drag force of the fabric on the resin flow is captured by adding a Darcy drag term to the momentum equations in a moving simulation domain. Furthermore, a method to simulate the porous solid mechanics of the fabric during the mold-filling is developed based on Terzaghi's effective stress theory (cf. Section 4.2). These two methods are coupled to simulate the interdepending resin flow and fabric deformation (cf. Section 4.3). Subsequently, the poro-elasticity and mold-filling methods are coupled in a partitioned FSI to model the interaction of mold-filling, porous fabric deformation, and an embedded foam core (cf. Section 4.4). Because of the compression of the foam material during mold-filling, the infiltration behavior and the cavity pressure change. All individual parts of the developed FSI method are verified by comparison to simplified cases. Furthermore, the method is verified by an analytical solution of a one-dimensional RTM mold-filling with a compressible foam core. The verifications of the coupled method show a very good agreement with the analytical solution of the simplified cases.

The developed FSI method is not only suited to simulate RTM mold-filling with embedded foam core but, by combining parts of the simulation method, the mold-filling of various continuous fiber reinforced plastics (CoFRP) manufacturing processes can be simulated. This makes the developed method a

flexible tool for predicting the resin flow and infiltration for numerous advanced manufacturing processes for CoFRP. To demonstrate this, several application examples are presented in this thesis.

The first application is made for pressure-controlled RTM (PC-RTM), which is a newly developed process using an active pressure control by changing the cavity height during mold-filling. The comparison to an analytical solution using Darcy's law shows an excellent agreement to the implemented method (Section 3.5 and the comparison to part-scale mold-filling experiments also shows a very good agreement (published in [32] and Section 6.1) for the prediction of the mold-filling time and gap height during the mold-filling.

The second application example shows the infiltration in Direct Sandwich Composite Molding (D-SCM), which is a process that uses the pressure of expanding foam material to infiltrate the face sheets of a sandwich (cf. Section 6.2). During the infiltration, the thickness of the part varies locally depending on the foaming pressure, the preform compaction pressure, and the fluid pressure. By simulating the infiltration with the coupled method of resin flow and fabric deformation, the processing time and the final part thickness can be predicted. Besides this application example, a recent publication by Nieschlag et al. also showed the successful application of the simulation method to the infiltration in a rotational molding process [112].

The third application example is used to analyze the influence of an embedded foam core on the mold-filling in RTM (cf. Section 6.3.1) and to validate the method on a part-scale (cf. Section 6.3.2). Therefore, the involved materials are first characterized (cf. Chapter 5). In this study, the focus is on the characterization of the fabric regarding permeability and on the compression modulus of the fabric and the polymer foam core. The characterization of the anisotropic polymer foam core is carried out by a combination of uniaxial and hydrostatic tests, which allows fitting the behavior to a transversely isotropic material model. The compression modulus in the thickness direction is significantly higher than in transverse directions. Furthermore, the PET foam core compression behavior is found to have a strong dependency on temperature and

density. The modulus is significantly reduced with increased temperature and decreased foam density (cf. Section 5.6).
The numerical study on a part-scale shows that the compression stiffness of the foam core material strongly influences the pressure level and the homogeneity of the flow front. A soft foam core leads to low cavity pressures because of two main reasons. First, the compression of the foam core leads to a slower resin velocity when a constant mass flow rate is set at the inlet. Second, and even more important, the compression of the foam core decreases the fiber volume fraction (FVF) in the top and bottom sheets, which results in a higher permeability and, thus, in lower pressure. The permeability is very sensitive to FVF, which is shown by the experimental characterization of the fabric (cf. Fig. 5.7) and is, therefore, the main reason for the strongly decreasing pressure when soft foam cores are embedded between the fabrics. Because of the anisotropic material behavior of the foam core, the compression during mold-filling leads to an inhomogeneous distribution of FVF, which results in an inhomogeneous resin flow velocity and flow front.
Additionally to the numerical study, validation experiments are carried out. Therefore, an RTM tool to manufacture sandwich components is developed. The tool contains several pressure sensors to track the flow front and the pressure level during mold-filling. The experiments also reveal a strong influence of the embedded foam core material on the mold-filling time and pressure. Like in the simulations, the pressure is lower and the mold-filling time higher for softer foam cores. The experimental results are then compared to the simulations and show the validity of the developed FSI method. The dependency of the pressure and mold-filling time on the embedded foam core is present in simulation and experiment and shows the same trends. The inaccuracies of the simulations are explained by the strong dependency of the foam core material behavior on its temperature, which is non-constant and unknown during the mold-filling since the non-isothermal behavior is not yet included in the simulation method. Furthermore, small gaps at the cavity and foam edges lead to race-tracking, which influences the mold-filling pattern and pressure evolution. Furthermore,

a one-sided race tracking leads to an asymmetric resin flow and, thus, to asymmetric deformation behavior of the foam core. As the permeability is very sensitive to small changes in FVF, this can lead to large differences in simulations and experiments. Not only an accurate mold-filling simulation method but also precise characterization methods and an exact description of the fabric and cavity geometry are necessary to obtain accurate simulation results.

8 Outlook

The developed poro-elasticity method allows not only to predict the fabric compression but also to capture in-plane deformations, which allows to predict and analyze fiber shifting during mold-filling, which can occur at high infiltration velocities. To simulate fiber shifting, additionally, a friction boundary condition has to be developed and the model has to be characterized for friction between fabric and mold wall as well as fabric and foam core.

For a better understanding of the mold-filling process, it is important to also focus research on the temperature in the cavity as it is non-constant in time and space throughout mold-filling. In the general assumption of flow in a porous medium, the temperatures of fibers and resin are equal, and only homogenized material parameters are used for heat capacity and conduction. This assumption is also made in this work, as the focus here is on non-constant cavities during mold-filling. To overcome this simplification, a two-equation model that solves two separate coupled temperature equations of the fabric and resin can be a possible solution. Additionally, non-isothermal modeling of the foam core to model the heat-up during the mold-filling can lead to more accurate results. A research focus here should be set on the heat transfer from the mold, the fabric, and the resin to the foam core. Furthermore, the curing reaction is highly exothermal, which needs to be embedded into the (resin) temperature equation, especially when modeling thick parts or components containing large pure resin areas.

Sandwich materials normally do not tend to show high distortions due to their very high geometrical stiffness. But to predict residual stresses and the final part weight, it is important to predict the foam deformation state after demolding.

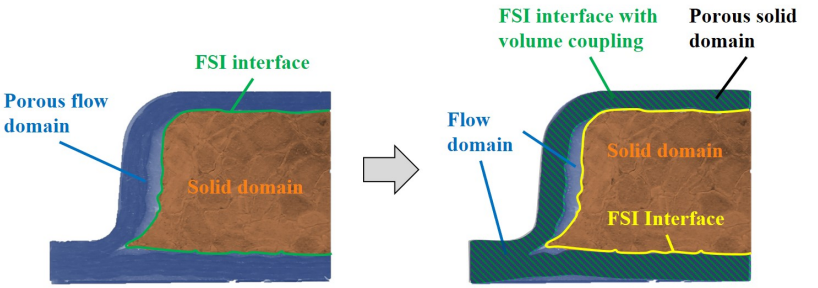

Figure 8.1: Schematic cut through an RTM sandwich part with a deformed foam core; left: Current FSI implementation, right: three-way FSI concept; adjusted from [146]

Therefore, a curing simulation using the internal stresses and strains in the foam and the fabric after mold-filling as initial conditions is necessary. To correctly predict the residual stresses and the foam core deformation after demolding, the visco-elasticity and visco-plasticity of the foam material have to be considered in the constitutive model. This also enables a prediction of the final part weight, which is an important optimization criterion for high-performance CoFRP. The part weight was shown to be influenced by processing conditions during mold-filling, though also an influence of the cavity pressure during the curing stage should be considered.

A further improvement to model the FSI during mold-filling can be achieved by using a three-way coupling of the fabric, the resin flow, and the foam core. With the current implementation, the poro-elasticity of the fabric is internally coupled to the mold-filling and uses the same simulation domain. Using the fabric as a third coupling partner and coupling it in a partitioned approach to the resin flow and the foam core deformation allows simulating the free flow in gaps that exist at edges or even enables to predict gap opening during mold-filling. The resin flow part of the developed method is already capable of simulating the free flow in the open gaps because of the VoF approach that is based on solving the Navier-Stokes equations. However, this kind of coupling needs a volumetric interface, where the fluid pressure and the deformation state of the

fabric are exchanged. Figure 8.1 shows the schematic concept of this coupling strategy. As a volumetric coupling increases the number of interface points strongly, also the numerical effort should be analyzed. A three-way coupling furthermore bridges the gap to accurately simulate the mold-filling in processes that involve a surface flow above the fabric like Wet Compression Molding (WCM).

A Analytical solution of PC-RTM

To verify the numerical simulations, Eq. (3.1) is solved analytically for the mold-filling process of PC-RTM. The filling of a plate using a linear injection gate leads to a one-dimensional flow, where the pressure $p(x,t)$ is a function of place and time, assuming a filling in the x-direction. The inlet gate as well as the pressure control is located at $X = 0$. The cavity height h is not known except for Stage 1 but can be calculated with an analytic solution assuming a constant pressure control value and a constant resin flow rate at the inlet in Stages 1 and 2.
For an analytical solution, combining Eq. (3.1) with the continuity equation of a compressible porous medium [11] gives

$$\frac{\partial h}{\partial t} = \nabla \left(h \cdot \tilde{\mathbf{u}}\right) = \nabla \left(-h \cdot \frac{\mathbf{K}}{\mu} \cdot \nabla p\right) \tag{A.1}$$

assuming an incompressible one-dimensional Darcy flow in x with compression in z, the compression velocity $u_\mathrm{c} = -\frac{\delta h}{\delta t}$ and the permeability in flow direction K_x follows

$$-u_\mathrm{c} = -h \cdot \frac{K_\mathrm{x}}{\mu} \cdot \frac{\partial^2 p}{\partial x^2}\,. \tag{A.2}$$

As only the fluid pressure p is a function of x, integrating Eq. (A.2) twice gives

$$\frac{\partial p}{\partial x} = \frac{u_\mathrm{c}}{h}\frac{\mu}{K_\mathrm{x}} \cdot x + C_1\,, \tag{A.3}$$

$$p(x,t) = \frac{1}{2}\frac{u_\mathrm{c}}{h}\frac{\mu}{K_\mathrm{x}} \cdot x^2 + C_1 \cdot x + C_2\,. \tag{A.4}$$

In Stage 1, the boundaries are the same as in conventional RTM with a rigid mold that means the compression velocity is $u_\mathrm{c} = 0$. Therefore the pressure gradient is constant and is given by

$$\frac{\partial p}{\partial x} = C_1^\mathrm{I} = -\frac{u_\mathrm{in}^\mathrm{I} \cdot \mu}{K_\mathrm{x}^0} \tag{A.5}$$

with the constant inlet velocity u_in^I and the initial permeability K_x^0. The flow front position is

$$x_\mathrm{f}^\mathrm{I} = \frac{u_\mathrm{in}^\mathrm{I}}{1-\varphi_0} \cdot t \tag{A.6}$$

with the initial fiber volume fraction φ_0. The pressure at the flow front is equal to the outlet pressure $p_1\left(x_\mathrm{f}^1\right) = p_\mathrm{out}$. With this boundary condition follows

$$C_2^\mathrm{I} = \frac{u_\mathrm{in}^\mathrm{I} \cdot \mu}{K_\mathrm{x}^0} \cdot x_\mathrm{f}^\mathrm{I} \tag{A.7}$$

and following the pressure in Stage 1 is given by

$$p^\mathrm{I}(x,t) = \frac{u_\mathrm{in}^\mathrm{I} \cdot \mu}{K_\mathrm{x}^0} \cdot \left(x_\mathrm{f}^\mathrm{I} - x\right) + p_\mathrm{out}\,. \tag{A.8}$$

The derivation of this equation or equivalent forms and its analytic solution for RTM or CRTM can be read in several publications, e.g. by Pham or Cai [70, 169].

Stage 2 is a combination of injection and (negative) compression. This leads to a different calculation of the flow front position, which depends on the injection

velocity $u_{\text{in}}^{\text{II}} = \frac{q}{h \cdot b}$, with the constant resin flow rate q and the constant width of the cavity b, and on the already injected resin in Stage 1. With t_1 as the time when Stage 2 starts follows

$$x_{\text{f}}^{\text{II}} = \frac{u_{\text{in}}^{\text{II}}}{1-\varphi} \cdot (t - t_1) + x_{\text{f}}^{\text{I}}(t_1) \cdot \frac{(1-\varphi_0) \cdot h_0}{(1-\varphi) \cdot h} \tag{A.9}$$

with the fiber volume fraction φ and the initial cavity height h_0. The first term in Eq. (A.9) describes the flow front advancement because of the resin injection and the second term is the change in the flow front position based on the continuity of the already injected resin in Stage 1.
At the inlet gate, the pressure gradient only depends on the injection velocity

$$\frac{\partial p}{\partial x}(x = 0) = C_1^{\text{II}} = -\frac{u_{\text{in}}^{\text{II}} \cdot \mu}{K_{\text{x}}} \,. \tag{A.10}$$

Additionally, the boundary condition at the flow front $p\left(x_{\text{f}}^{\text{II}}\right) = p_{\text{out}}$ is used. The integration constant C_2^{II} therefore is

$$C_2^{\text{II}} = p_{\text{out}} + \frac{1}{2}\frac{u_{\text{c}}}{h}\frac{\mu}{K_{\text{x}}} \cdot x_{\text{f}}^{\text{II}^2} + \frac{u_{\text{in}}^{\text{II}} \cdot \mu}{K_{\text{x}}} \cdot x_{\text{f}}^{\text{II}} \,. \tag{A.11}$$

The pressure at the inlet is constant in this stage. In summary, the pressure is again a combination of the pressure due to injection and the pressure due to compression

$$p_2(x = 0, t) = p_{\text{control}} = C_2^{\text{II}} \,. \tag{A.12}$$

In Stage 3, the injection velocity is $u_{\text{in}}^{\text{III}} = 0$ and therefore, the flow front position is only the result of the continuity of the already injected resin

$$x_{\text{f}}^{\text{III}} = x_{\text{f}}^{\text{II}}(t_2) \cdot \frac{(1-\varphi_2) \cdot h_2}{(1-\varphi) \cdot h} \tag{A.13}$$

with t_2 as the time, when Stage 3 starts and φ_2 and h_2 as the final fiber volume fraction and cavity height after Stage 2. The pressure gradient at the inlet wall is zero

$$\frac{\partial p}{\partial x}(x = 0, t) = C_1^{\mathrm{III}} = 0 \tag{A.14}$$

and with Eq. (A.4) follows the second integration constant like in Stage 2

$$C_2^{\mathrm{III}} = p_{\mathrm{out}} + \frac{1}{2}\frac{u_{\mathrm{c}}}{h}\frac{\mu}{K_{\mathrm{x}}} \cdot x_{\mathrm{f}}^{\mathrm{II}2} \,. \tag{A.15}$$

Finally, the pressure at the inlet position can be determined, which is again constant because of the pressure control

$$p_3(x = 0, t) = p_{\mathrm{control}} = C_2^{\mathrm{III}} \,. \tag{A.16}$$

Equations (A.12) and (A.16) can now be used to calculate the flow front position and the time-dependent cavity height h for Stage 2 and Stage 3.

B Analytical solution of RTM with embedded foam core

To verify the numerical simulations, Eq. (3.1) is solved analytically for the stationary pressure with induced deformations together wit a linear spring model for the foam core material and a non-linear spring model for the porous fabric. A one-dimensional stationary flow leads to

$$u_\mathrm{x} = -\frac{K_\mathrm{x}}{\mu} \cdot \frac{\partial p}{\partial x}\,, \tag{B.1}$$

where additionally the velocity u_x, the height h and the permeability K_x are a function of x. The height is calculated based on the equilibrium of forces or stresses of the core with the porous fabric and resin pressure. It is assumed here, that only normal forces in the vertical direction apply at the foam-fabric interface. The two solids can then be interpreted as two springs in series. With this assumption follows

$$\begin{aligned} \sigma_\mathrm{c} &= \sigma_\mathrm{f} + p\,, \\ k_\mathrm{c}\Delta h_\mathrm{c} &= k_\mathrm{f}\Delta h_\mathrm{f} + p\,, \end{aligned} \tag{B.2}$$

with the normal stresses of the foam core σ_c and the fabric σ_f and their spring constants k_c and k_f, respectively. In this case, a spring constant is used to

describe the foam core and a linear spring function depending on the fiber volume fraction is used to describe the fabric material

$$\begin{aligned} k_\mathrm{c} &= \frac{E_\mathrm{c}}{H_0}\,, \\ k_\mathrm{f} &= \frac{c_1 \cdot \varphi + c_2}{/h_0}\,, \end{aligned} \tag{B.3}$$

with two Young's moduli to describe the linear relationship to the fiber volume fraction

$$\begin{aligned} c_1 &= \frac{E_{\mathrm{fabric},\varphi_2} - E_{\mathrm{fabric},\varphi_1}}{\varphi_2 - \varphi_1} \\ c_2 &= -c_1 \cdot \varphi_1 + E_{\mathrm{fabric},\varphi_1}\,. \end{aligned} \tag{B.4}$$

Using the displacement condition $\Delta h_\mathrm{c} = -\Delta h_\mathrm{f}$ leads to a function for the height of the cavity depending on the pressure.
The permeability is calculated with a material model as a function of the fiber volume fraction, which is directly related to the height

$$K_\mathrm{x} = A \cdot \frac{1-\varphi^3}{\varphi^2}\,, \tag{B.5}$$

$$\varphi = \frac{h_0}{h} \cdot \varphi_0\,, \tag{B.6}$$

with the initial states indicated with subscript 0.
The same applies to the flow velocity, that depends on the fiber volume fraction and the cavity height

$$u_\mathrm{x} = u_\mathrm{inj} \cdot \frac{1-\varphi_\mathrm{inj}}{1-\varphi} \cdot \frac{1-h_\mathrm{inj}}{1-h}\,, \tag{B.7}$$

with the resin injection velocity u_inj.

Inserting this into Eq. (B.1) and integrating gives

$$p(x) = \mu \cdot \int_0^L \frac{u_\mathrm{x}}{K_\mathrm{x}} dx \,. \tag{B.8}$$

A constant pressure is set at the outlet $p(x = L) = p_\mathrm{out}$ as boundary condition. The analytical integration of Eq. (B.8) is done using the software Maple 2021.0, because of the strong complex dependencies of u_x and K_x on the pressure itself, which leads to a function for $p(x)$, where integration is not trivial.

List of Figures

List of Tables

Bibliography

[1] IEA, “Verteilung der energiebedingten CO2-Emissionen weltweit nach Sektor im Jahr 2018,” https://de.statista.com/statistik/daten/studie/167957/umfrage/verteilung-der-co-emissionen-weltweit-nach-bereich/, 2020, accessed: 2022-02-20.

[2] F. Henning and E. Moeller, Eds., *Handbuch Leichtbau: Methoden, Werkstoffe, Fertigung*. München: Hanser, 2011.

[3] The Boeing Company, “787 By Design,” https://www.boeing.com/commercial/787/by-design/#/advanced-composite-use, 2021, accessed: 2022-02-20.

[4] T. von Reden and D. Schüppel, “Entwicklungen hin zu kostengünstigem CFK,” *Lightweight Design*, vol. 12, no. 1, pp. 60–63, 2019.

[5] P. Rosenberg, B. Thoma, and F. Henning, “Investigation of a new cavity pressure controlled HP-RTM process variant (PC-RTM),” *Conference Paper 16th annual SPE Automotive Composites Conference & Exhibition*, 2016, Novi, MI, US.

[6] F. Henning, L. Kärger, D. Dörr, F. J. Schirmaier, J. Seuffert, and A. Bernath, “Fast processing and continuous simulation of automotive structural composite components,” *Composites Science and Technology*, vol. 171, pp. 261–279, 2019.

[7] L. Kärger, A. Bernath, F. Fritz, S. Galkin, D. Magagnato, A. Oeckerath, A. Schön, and F. Henning, "Development and validation of a CAE chain for unidirectional fibre reinforced composite components," *Composite Structures*, vol. 132, pp. 350–358, 2015.

[8] P. Simacek and S. G. Advani, "A numerical model to predict fiber tow saturation during liquid composite molding," *Composites Science and Technology*, vol. 63, no. 12, pp. 1725–1736, 2003.

[9] D. Magagnato, J. Seuffert, A. Bernath, L. Kärger, and F. Henning, "Experimental and numerical study of the influence of integrated load transmission elements on filling behavior in resin transfer molding," *Composite Structures*, vol. 198, pp. 135–143, 2018.

[10] W. B. Young, L. H. Fong, K. Han, and L. J. Lee, "Flow simulation in molds with preplaced fiber mats," *Polymer Composites*, vol. 12, no. 6, pp. 391–403, 1991.

[11] F. Trochu, E. Ruiz, V. Achim, and S. Soukane, "Advanced numerical simulation of liquid composite molding for process analysis and optimization," *Composites Part A: Applied Science and Manufacturing*, vol. 37, no. 6, pp. 890–902, 2006.

[12] T. Okabe, Y. Oya, G. Yamamoto, J. Sato, T. Matsumiya, R. Matsuzaki, S. Yashiro, and S. Obayashi, "Multi-objective optimization for resin transfer molding process," *Composites Part A: Applied Science and Manufacturing*, vol. 92, pp. 1–9, 2017.

[13] M. Deléglise, P. Le Grognec, C. Binetruy, P. Krawczak, and B. Claude, "Modeling of high speed RTM injection with highly reactive resin with on-line mixing," *Composites Part A: Applied Science and Manufacturing*, vol. 42, no. 10, pp. 1390–1397, 2011.

[14] A. Saad, A. Echchelh, M. Hattabi, and M. El Ganaoui, "Optimization of the cycle time in resin transfer molding process by numerical

simulation," *Journal of Reinforced Plastics and Composites*, vol. 31, no. 20, pp. 1388–1399, 2012.

[15] A. Al-Hamdan, M. Al-Ajloni, M. Alhusein, C. D. Rudd, and A. C. Long, "Behaviour of core materials during resin transfer moulding of sandwich structures," *Materials Science and Technology*, vol. 16, no. 7-8, pp. 929–934, 2000.

[16] C. Binetruy and S. G. Advani, "Foam Core Deformation During Liquid Molding of Sandwich Structures: Modeling and Experimental Analysis," *Journal of Sandwich Structures and Materials*, vol. 5, no. 4, pp. 351–375, 2003.

[17] J. Gerstenkorn, "Entwicklung einer Methodik zur Analyse und Vorhersage des mechanischen Verhaltens polymerer Hartschäume im RTM-Prozess," Dissertation, Karlsruhe Institute of Technology (KIT), Karlsruhe, Germany, 2020.

[18] F. Behnisch, V. Lichtner, F. Henning, and P. Rosenberg, "Development of a Reactive Polyurethane Foam System for the Direct Sandwich Composite Molding (D-SCM) Process," *Journal of Composites Science*, vol. 5, no. 4, p. 104, 2021.

[19] T. G. P. Gutowski, Ed., *Advanced composites manufacturing*, ser. A Wiley interscience publication. New York, NY: Wiley, 1997.

[20] D. V. Rosato and D. V. Rosato, *Reinforced Plastics Handbook*. Oxford, UK: Elsevier Ltd., 2005.

[21] L. Nicolais, Ed., *Wiley Encyclopedia of Composites*. Hoboken, NJ, USA: John Wiley & Sons, Inc, 2011.

[22] M. Neitzel, P. Mitschang, and U. Breuer, *Handbuch Verbundwerkstoffe: Werkstoffe, Verarbeitung, Anwendung*, 2nd ed. Munich, Germany: Carl Hanser Verlag, 2014.

[23] R. S. Parnas, *Liquid Composite Molding*, 1st ed. Munich, Germany: Carl Hanser Verlag, 2000.

[24] K. van Rijswijk and H. Bersee, "Reactive processing of textile fiber-reinforced thermoplastic composites – An overview," *Composites Part A: Applied Science and Manufacturing*, vol. 38, no. 3, pp. 666–681, 2007.

[25] T. Ageyeva, I. Sibikin, and J. G. Kovács, "A Review of Thermoplastic Resin Transfer Molding: Process Modeling and Simulation," *Polymers*, vol. 11, no. 10, p. 1555, 2019.

[26] W.-B. Young and C.-W. Tseng, "Study on the Pre-Heated Temperatures and Injection Pressures of the RTM Process," *Journal of Reinforced Plastics and Composites*, vol. 13, pp. 467–482, 1994.

[27] P. Rosenberg, R. Chaudhari, M. Karcher, F. Henning, and P. Elsner, "Investigating cavity pressure behavior in high-pressure RTM process variants," in *Proceedings of PPS-29*, ser. AIP Conference Proceedings, American Institute of Physics, Ed. American Institute of Physics, 2014, pp. 463–466.

[28] W.-B. Young and C.-W. Chiu, "Study on Compression Transfer Molding," *Journal of Composite Materials*, vol. 29, no. 16, pp. 2180–2191, 1995.

[29] P. Bhat, J. Merotte, P. Simacek, and S. G. Advani, "Process analysis of compression resin transfer molding," *Composites Part A: Applied Science and Manufacturing*, vol. 40, no. 4, pp. 431–441, 2009.

[30] G. Deinzer, M. Kothmann, D. Roquette, and F. Diebold, "AUDI Ultra-RTM: A technology for high performance and cost effective CFRP parts for high volume production," *Conference Paper ECCM17-European Conference on Composite Materials*, 2016, Munich, Germany.

[31] P. Rosenberg, “Entwicklung einer RTM Prozessvariante zur kavitätsdruckgeregelten Herstellung von Faserverbundstrukturbauteilen,” Dissertation, Karlsruhe Institute of Technology (KIT), Karlsruhe, Germany, 2018.

[32] J. Seuffert, P. Rosenberg, L. Kärger, F. Henning, M. H. Kothmann, and G. Deinzer, “Experimental and numerical investigations of pressure-controlled resin transfer molding (PC-RTM),” *Advanced Manufacturing: Polymer & Composites Science*, vol. 6, no. 3, pp. 154–163, 2020.

[33] N. C. Correia, F. Robitaille, A. C. Long, C. D. Rudd, P. Šimáček, and S. G. Advani, “Analysis of the vacuum infusion moulding process: I. Analytical formulation,” *Composites Part A: Applied Science and Manufacturing*, vol. 36, no. 12, pp. 1645–1656, 2005.

[34] J. Summerscales and T. J. Searle, “Low-pressure (vacuum infusion) techniques for moulding large composite structures,” *Proceedings of the Institution of Mechanical Engineers, Part L: Journal of Materials: Design and Applications*, vol. 219, no. 1, pp. 45–58, 2005.

[35] A. Hindersmann, “Confusion about infusion: An overview of infusion processes,” *Composites Part A: Applied Science and Manufacturing*, vol. 126, no. 6, p. 105583, 2019.

[36] J. Bergmann, H. Dörmann, and R. Lange, “Interpreting process data of wet pressing process. Part 2: Verification with real values,” *Journal of Composite Materials*, vol. 50, no. 17, pp. 2409–2419, 2016.

[37] C. Poppe, D. Dörr, F. Henning, and L. Kärger, “A 2D modeling approach for fluid propagation during FE-forming simulation of continuously reinforced composites in wet compression moulding,” in *Proceedings of the 21st International ESAFORM Conference on*

Material Forming, AIP Conference Proceedings, 2018, vol. 1960, p. 020022.

[38] C. T. Poppe, C. Krauß, F. Albrecht, and L. Kärger, "A 3D process simulation model for wet compression moulding," *Composites Part A: Applied Science and Manufacturing*, vol. 145, no. 17, p. 106379, 2021.

[39] C. D. Rudd, *Liquid moulding technologies: Resin transfer moulding, structural reaction injection moulding, and related processing techniques*. Warrendale, PA and Cambridge, England: SAE International, 1997.

[40] Hexcel Corporation, "HexFlow RTM6 - Product Data sheet," https://www.hexcel.com/user_area/content_media/raw/RTM6_DataSheetPDF.pdf, 2021, accessed: 2021-07-18.

[41] P. Malnati and J. Sloan, "Fast and Faster: Rapid-cure resins drive down cycle times," https://www.compositesworld.com/articles/fast-and-faster-rapid-cure-epoxies-drive-down-cycle-times, 2018, accessed: 2022-02-20.

[42] A. Bernath, L. Kärger, and F. Henning, "Accurate Cure Modeling for Isothermal Processing of Fast Curing Epoxy Resins," *Polymers*, vol. 8, no. 11, p. 390, 2016.

[43] A. Bernath, "Numerical prediction of curing and process-induced distortion of composite structures," Dissertation, Karlsruhe Institute of Technology (KIT), Karlsruhe, Germany, 2020.

[44] S. J. Stanglmaier, "Empirische Charakterisierung und Modellierung des Imprägnierprozesses lokal verstärkter Kohlenstofffaserhalbzeuge im RTM- und Nasspress-Verfahren für die Großserie," Dissertation, Karlsruhe Institute of Technology (KIT), Karlsruhe, Germany, 2017.

[45] V. Mittal, R. Saini, and S. Sinha, "Natural fiber-mediated epoxy composites – A review," *Composites Part B: Engineering*, vol. 99, no. 7, pp. 425–435, 2016.

[46] O. Faruk, A. K. Bledzki, H.-P. Fink, and M. Sain, "Biocomposites reinforced with natural fibers: 2000–2010," *Progress in Polymer Science*, vol. 37, no. 11, pp. 1552–1596, 2012.

[47] J. P. Torres, L.-J. Vandi, M. Veidt, and M. T. Heitzmann, "The mechanical properties of natural fibre composite laminates: A statistical study," *Composites Part A: Applied Science and Manufacturing*, vol. 98, no. 8, pp. 99–104, 2017.

[48] H.-M. Hsiao and I. M. Daniel, "Effect of fiber waviness on stiffness and strength reduction of unidirectional composites under compressive loading," *Composites Science and Technology*, vol. 56, no. 5, pp. 581–596, 1996.

[49] K. F. Karlsson and T. Aström, "Manufacturing and applications of structural sandwich components," *Composites Part A: Applied Science and Manufacturing*, no. 28, pp. 97–111, 1996.

[50] H. Hertel, *Leichtbau: Bauelemente, Bemessungen und Konstruktionen von Flugzeugen und anderen Leichtbauwerken*. Berlin and Heidelberg, Germany: Springer, 1960.

[51] T. Bitzer, *Honeycomb Technology: Materials, Design, Manufacturing, Applications and Testing*. Dordrecht, Netherlands: Springer, 1997.

[52] J. R. Vinson, "Sandwich Structures," *Applied Mechanics Reviews*, vol. 54, no. 3, pp. 201–214, 2001.

[53] H. Seibert, "Applications for PMI foams in aerospace sandwich structures," https://www.materialstoday.com/composite-applications/f

eatures/applications-for-pmi-foams-in-aerospace-sandwich/, 2006, accessed: 2022-02-20.

[54] Evonik Resource Efficiency GmbH, “Rohacell IG-F: Data sheet,” https://www.rohacell.com/product/peek-industrial/downloads/rohacell%20ig-f_2020_january.pdf, 2021, accessed: 2021-10-19.

[55] 3A Composites Core Materials, “AIREX C70 - Universal Structural Foam: Data sheet,” https://www.3accorematerials.com/uploads/documents/TDS-AIREX-C70-E-04.2020.pdf, 2020, accessed: 2021-07-18.

[56] J. Gerstenkorn, G. Deinzer, M. Kothmann, F. Diebold, L. Kärger, and F. Henning, “Experimental Analysis of the influence of foam density and surface treatment on the failure behavior of polyurethane foam during the RTM process,” *Conference Paper ICAutoC – International Conference on Automotive Composites*, 2016, Lisbon, Portugal.

[57] M. H. Kothmann, A. Hillebrand, and G. Deinzer, “Multimaterialkarosserien für batterieelektrische Fahrzeuge,” *Lightweight Design*, vol. 11, no. 2, pp. 10–17, 2018.

[58] 3A Composites Core Materials, “AIREX T92 - Easy Processing Structural Foam: Data sheet,” https://www.3accorematerials.com/uploads/documents/TDS-AIREX-T92-E-01.2020.pdf, 2020, accessed: 2021-07-18.

[59] S. Laurenzi, A. Grilli, M. Pinna, F. de Nicola, G. Cattaneo, and M. Marchetti, “Process simulation for a large composite aeronautic beam by resin transfer molding,” *Composites Part B: Engineering*, vol. 57, pp. 47–55, 2014.

[60] E. Poodts, G. Minak, L. Mazzocchetti, and L. Giorgini, “Fabrication, process simulation and testing of a thick CFRP component using the

RTM process," *Composites Part B: Engineering*, vol. 56, pp. 673–680, 2014.

[61] D. Magagnato and F. Henning, "Simulation of mold filling in resin transfer molding considering the local fiber architecture after the preforming process," *Proceedings of the 20th Conference on Composite Materials (ICCM 2015)*, pp. 4209–4, 2015, Copenhagen, Denmark.

[62] J. Wang, P. Simacek, and S. G. Advani, "Use of medial axis to find optimal channel designs to reduce mold filling time in resin transfer molding," *Composites Part A: Applied Science and Manufacturing*, vol. 95, pp. 161–172, 2017.

[63] S. G. Advani, Ed., *Flow and rheology in polymer composites manufacturing*, ser. Composite materials. Amsterdam: Elsevier, 1994, vol. 10.

[64] N. D. Ngo and K. K. Tamma, "Computational developments for simulation based design: Multi-scale physics and flow/thermal/cure/stress modeling, analysis, and validation for advanced manufacturing of composites with complex microstructures," *Archives of Computational Methods in Engineering*, vol. 10, no. 1-2, pp. 3–206, 2003.

[65] H. Darcy, *Les Fontaines publiques de la ville de Dijon*. Paris: Dalmont, 1856.

[66] S. Whitaker, "Flow in porous media I: A theoretical derivation of Darcy's law," *Transport in Porous Media*, vol. 1, pp. 3–25, 1986.

[67] C. A. Fracchia, J. Castro, and C. L. Tucker III, "A finite element/control volume simulation of resin transfer mold filling," *Proceedings of the American Society for Composites 4th Technical Conference*, pp. 157–166, 1989, Blacksburg, VA, US.

[68] M. V. Bruschke and S. G. Advani, “A finite element/control volume approach to mold filling in anisotropic porous media,” *Polymer Composites*, vol. 11, no. 6, pp. 398–405, 1990.

[69] F. Trochu, R. Gauvin, and D.-M. Gao, “Numerical analysis of the resin transfer molding process by the finite element method,” *Advances in Polymer Technology*, vol. 12, no. 4, pp. 329–342, 1993.

[70] X.-T. Pham, F. Trochu, and R. Gauvin, “Simulation of Compression Resin Transfer Molding with Displacement Control,” *Journal of Reinforced Plastics and Composites*, vol. 17, no. 17, pp. 1525–1556, 1998.

[71] X.-T. Pham and F. Trochu, “Simulation of compression resin transfer molding to manufacture thin composite shells,” *Polymer Composites*, vol. 20, no. 3, pp. 436–459, 1999.

[72] A. Shojaei, “Numerical simulation of three-dimensional flow and analysis of filling process in compression resin transfer moulding,” *Composites Part A: Applied Science and Manufacturing*, vol. 37, no. 9, pp. 1434–1450, 2006.

[73] P. Simacek, S. G. Advani, and S. A. Iobst, “Modeling Flow in Compression Resin Transfer Molding for Manufacturing of Complex Lightweight High-Performance Automotive Parts,” *Journal of Composite Materials*, vol. 42, no. 23, pp. 2523–2545, 2008.

[74] W. D. Hirt and B. D. Nichols, “Volume of Fluid (VOF) Method for the Dynamics of Free Boundaries,” *Journal of Computational Physics*, vol. 39, pp. 201–225, 1981.

[75] D. Magagnato, M. Frey, A. Bernath, P. Steibler, and F. Henning, “Experimentelle und numerische Untersuchung der Infiltration bei der RTM-Fertigung,” in *Verbundwerkstoffe und Werkstoffverbunde*, A. Wanner and K. Weidenmann, Eds., 2013, pp. 511–517.

[76] D. Magagnato and F. Henning, “RTM molding simulation for unidirectional fiber reinforced composite components considering local fiber orientation and fiber volume fraction,” *Journal of Plastics Technology*, vol. 12, no. 3, pp. 136–156, 2016.

[77] J. Seuffert, L. Kärger, and F. Henning, “Simulating Mold Filling in Compression Resin Transfer Molding (CRTM) Using a Three-Dimensional Finite-Volume Formulation,” *Journal of Composites Science*, vol. 2, no. 2, p. 23, 2018.

[78] J. Seuffert, P. Rosenberg, L. Kärger, F. Henning, M. Kothmann, and G. Deinzer, “Mold filling simulation of a pressure controlled resin transfer molding (PC-RTM) process - method and application,” *International Conference on Flow Processes in Composite Materials (FPCM)*, 2018, Lulea, Sweden.

[79] S. S. Deshpande, L. Anumolu, and M. F. Trujillo, “Evaluating the performance of the two-phase flow solver interFoam,” *Computational Science & Discovery*, vol. 5, no. 014016, 2012.

[80] J. Roenby, H. Bredmose, and H. Jasak, “A computational method for sharp interface advection,” *Royal Society open science*, vol. 3, no. 11, p. 160405, 2016.

[81] H. Jasak, “Error Analysis and Estimation for the Finite Volume Method with Applications to Fluid Flows,” PhD Thesis, University of London, London, 1996.

[82] I. Demirdžić and M. Perić, “Space conservation law in finite volume calculations of fluid flow,” *International Journal for Numerical Methods in Fluids*, vol. 8, pp. 1037–1050, 1988.

[83] I. Demirdžić and A. Ivanković, “Numerical simulation of thermal deformation in welded workpiece,” *Zavarivanje*, vol. 31, no. 5-6, 1988.

[84] J. H. Ferziger and M. Perić, *Computational Methods for Fluid Dynamics*, 3rd ed. Berlin and Heidelberg, Germany: Springer, 2002.

[85] H. Jasak, "Dynamic Mesh Handling in OpenFOAM," *47th AIAA Aerospace Sciences Meeting Including The New Horizons Forum and Aerospace Exposition*, p. 341, 2009, Orlando, FL, US.

[86] R. I. Issa, "Solution of the Implicitly Discretised Fluid Flow Equations by Operator-Splitting," *Journal of Computational Physics*, no. 62, pp. 40–65, 1985.

[87] I. Demirdžić, Z. Lilek, and M. Perić, "A collocated finite volume method for predicting flows at all speeds," *International Journal for Numerical Methods in Fluids*, vol. 16, pp. 1029–1050, 1993.

[88] J. H. Jiang, Z. X. Wang, and N. L. Chen, "Measurement of Transverse Permeability of Fabric Preforms Using Ultrasound Monitoring Technique in LCM Processes," *Advanced Materials Research*, vol. 311-313, pp. 214–217, 2011.

[89] R. Arbter, J. M. Beraud, C. Binetruy, L. Bizet, J. Bréard, S. Comas-Cardona, C. Demaria, A. Endruweit, P. Ermanni, F. Gommer, S. Hasanovic, P. Henrat, F. Klunker, B. Laine, S. Lavanchy, S. V. Lomov, A. Long, V. Michaud, G. Morren, E. Ruiz, H. Sol, F. Trochu, B. Verleye, M. Wietgrefe, W. Wu, and G. Ziegmann, "Experimental determination of the permeability of textiles: A benchmark exercise," *Composites Part A: Applied Science and Manufacturing*, vol. 42, no. 9, pp. 1157–1168, 2011.

[90] N. Vernet, E. Ruiz, S. Advani, J. B. Alms, M. Aubert, M. Barburski, B. Barari, J. M. Beraud, D. C. Berg, N. Correia, M. Danzi, T. Delavière, M. Dickert, C. Di Fratta, A. Endruweit, P. Ermanni, G. Francucci, J. A. Garcia, A. George, C. Hahn, F. Klunker, S. V. Lomov, A. Long, B. Louis, J. Maldonado, R. Meier, V. Michaud, H. Perrin, K. Pillai,

E. Rodriguez, F. Trochu, S. Verheyden, M. Wietgrefe, W. Xiong, S. Zaremba, and G. Ziegmann, "Experimental determination of the permeability of engineering textiles: Benchmark II," *Composites Part A: Applied Science and Manufacturing*, vol. 61, pp. 172–184, 2014.

[91] D. May, A. Aktas, S. G. Advani, D. C. Berg, A. Endruweit, E. Fauster, S. V. Lomov, A. Long, P. Mitschang, S. Abaimov, D. Abliz, I. Akhatov, M. A. Ali, T. D. Allen, S. Bickerton, M. Bodaghi, B. Caglar, H. Caglar, A. Chiminelli, N. Correia, B. Cosson, M. Danzi, J. Dittmann, P. Ermanni, G. Francucci, A. George, V. Grishaev, M. Hancioglu, M. A. Kabachi, K. Kind, M. Deléglise-Lagardère, M. Laspalas, O. V. Lebedev, M. Lizaranzu, P.-J. Liotier, P. Middendorf, J. Morán, C.-H. Park, R. B. Pipes, M. F. Pucci, J. Raynal, E. S. Rodriguez, R. Schledjewski, R. Schubnel, N. Sharp, G. Sims, E. M. Sozer, P. Sousa, J. Thomas, R. Umer, W. Wijaya, B. Willenbacher, A. Yong, S. Zaremba, and G. Ziegmann, "In-plane permeability characterization of engineering textiles based on radial flow experiments: A benchmark exercise," *Composites Part A: Applied Science and Manufacturing*, vol. 121, pp. 100–114, 2019.

[92] D. Magagnato and F. Henning, "Process-Oriented Determination of Preform Permeability and Matrix Viscosity during Mold Filling in Resin Transfer Molding," *Materials Science Forum*, vol. 825-826, pp. 822–829, 2015.

[93] W. B. Young and C.-L. Lai, "Analysis of the edge effect in resin transfer molding," *Composites Part A: Applied Science and Manufacturing*, no. 28A, pp. 817–822, 1997.

[94] A. Hammami, R. Gauvin, and F. Trochu, "Modeling the edge effect in liquid composites molding," *Composites Part A: Applied Science and Manufacturing*, vol. 29A, pp. 603–609, 1998.

[95] H. C. Brinkman, “A calculation of the viscous force exerted by a flowing fluid on a dense swarm of particles,” *Flow, Turbulence and Combustion*, vol. 1, no. 1, pp. 27–34, 1949.

[96] B. R. Gebart, “Permeability of Unidirectional Reinforcements for RTM,” *Journal of Composite Materials*, no. 26, pp. 1100–1133, 1992.

[97] J. Kozeny, “Über kapillare Leitung des Wassers im Boden,” Vienna, Austria, pp. 271–306, 1927.

[98] P. C. Carman, “Fluid flow through granular beds,” *Trans. INSTN Chemical Engineers*, vol. 15, 1937.

[99] M. K. Um and W. I. Lee, “A Study on Permeability of unidirectional Fiber Beds,” *Journal of Reinforced Plastics and Composites*, vol. 16, no. 17, pp. 1575–1590, 1997.

[100] G. Bechtold and L. Ye, “Influence of fibre distribution on the transverse flow permeability in fibre bundles,” *Composites Science and Technology*, vol. 63, no. 14, pp. 2069–2079, 2003.

[101] J. Seuffert, L. Bittrich, L. Cardoso de Oliveira, A. Spickenheuer, and L. Kärger, “Micro-scale permeability characterization of carbon fiber composites using micrograph volume elements (MVE),” *Frontiers in Materials*, no. 8:745084, 2021.

[102] C. Binétruy, B. Hilaire, and J. Pabiot, “The interactions between flows occurring inside and outside fabric tows during rtm,” *Composites Science and Technology*, vol. 57, no. 5, pp. 587–596, 1997.

[103] A. Endruweit and A. C. Long, “Influence of stochastic variations in the fibre spacing on the permeability of bi-directional textile fabrics,” *Composites Part A: Applied Science and Manufacturing*, vol. 37, no. 5, pp. 679–694, 2006.

[104] A. Endruweit, X. Zeng, M. Matveev, and A. C. Long, "Effect of yarn cross-sectional shape on resin flow through inter-yarn gaps in textile reinforcements," *Composites Part A: Applied Science and Manufacturing*, vol. 104, pp. 139–150, 2018.

[105] M. R. Kamal, S. Sourour, and M. Ryan, "Integrated thermo-rheological analysis of the cure of thermosets," *SPE Technical Paper*, vol. 19, pp. 187–191, 1973.

[106] J. Grindling, "Simulation zur Verarbeitung von reaktiven Non-Post-Cure-Epoxidharz-Systemen im Druckgelieren und konventionellen Vergiessen," Dissertation, Universität Paderborn, 2006.

[107] J. M. Castro and C. W. Macosko, "Studies of mold filling and curing in the reaction injection molding process," *AIChE Journal*, vol. 28, no. 2, pp. 250–260, 1982.

[108] A. Bernath, L. Grulich, L. Kärger, and F. Henning, "Enhanced viscosity characterization for fast curing epoxy resins at process relevant temperatures," *International Conference on Flow Processes in Composite Materials (FPCM)*, 2018, Lulea, Sweden.

[109] P. J. Halley and G. A. George, *Chemorheology of Polymers: From fundamental principles to reactive processing*. Cambridge University Press, UK, 2009.

[110] U. Eberhard, H. J. Seybold, M. Floriancic, P. Bertsch, J. Jiménez-Martínez, J. S. Andrade, and M. Holzner, "Determination of the effective viscosity of non-newtonian fluids flowing through porous media," *Frontiers in Physics*, vol. 7, p. 71, 2019.

[111] T. Sochi, "Non-newtonian flow in porous media," *Polymer*, vol. 51, no. 22, pp. 5007–5023, 2010.

[112] J. Nieschlag, J. Seuffert, D. Strack, L. Friedmann, Marco; Kärger, F. Henning, and J. Fleischer, "Experimental and numerical analysis of mold filling in rotational molding (accepted)," *Journal of Composites Science*, vol. 5, no. 11, p. 289, 2021.

[113] J. Seuffert, L. Kärger, and F. Henning, "Simulation of the Influence of Embedded Inserts on the RTM Filling Behavior Considering Local Fiber Structure," *Key Engineering Materials*, vol. 742, pp. 681–688, 2017.

[114] M. Muth, J. Schwennen, A. Bernath, J. Seuffert, K. A. Weidenmann, J. Fleischer, and F. Henning, "Numerical and experimental investigation of manufacturing and performance of metal inserts embedded in CFRP," *Production Engineering*, vol. 24, no. 12, p. 1246, 2018.

[115] K. Terzaghi, *Erdbaumechanik auf bodenphysikalischer Grundlage*. Leipzig: Franz Deuticke, 1925.

[116] V. I. Osipov, "The Terzaghi Theory of Effective Stress," in *Physicochemical Theory of Effective Stress in Soils*, ser. SpringerBriefs in Earth Sciences, V. Osipov, Ed. Cham: Springer International Publishing, 2015, pp. 35–37.

[117] M. Deleglise, C. Binetruy, and P. Krawczak, "Simulation of LCM processes involving induced or forced deformations," *Composites Part A: Applied Science and Manufacturing*, vol. 37, no. 6, pp. 874–880, 2006.

[118] D. Ambrosi and L. Preziosi, "Modelling matrix injection through elastic porous preforms," *Composites Part A: Applied Science and Manufacturing*, vol. 29A, pp. 5–18, 1998.

[119] C. H. Park and A. Saouab, "Analytical Modeling of Composite Molding by Resin Infusion with Flexible Tooling: VARI and RFI processes," *Journal of Composite Materials*, vol. 43, no. 18, pp. 1877–1900, 2009.

[120] P. Celle, S. Drapier, and J.-M. Bergheau, "Numerical aspects of fluid infusion inside a compressible porous medium undergoing large strains," *Revue européenne de mécanique numérique*, vol. 17, no. 5-6-7, pp. 819–827, 2008.

[121] P. Simacek and S. G. Advani, "Resin flow modeling in compliant porous media: An efficient approach for liquid composite molding," *International Journal of Material Forming*, vol. 11, no. 4, pp. 503–515, 2018.

[122] D. Wu and R. Larsson, "A shell model for resin flow and preform deformation in thin-walled composite manufacturing processes," *International Journal of Material Forming*, vol. 31, no. 15, p. 1149, 2019.

[123] A. Dereims, S. Drapier, J.-M. Bergheau, and P. de Luca, "3D robust iterative coupling of Stokes, Darcy and solid mechanics for low permeability media undergoing finite strains," *Finite Elements in Analysis and Design*, vol. 94, pp. 1–15, 2014.

[124] C. Poppe, D. Dörr, F. Henning, and L. Kärger, "Experimental and numerical investigation of the shear behaviour of infiltrated woven fabrics," *Composites Part A: Applied Science and Manufacturing*, vol. 114, pp. 327–337, 2018.

[125] C. Poppe, T. Rosenkranz, D. Dörr, and L. Kärger, "Comparative experimental and numerical analysis of bending behaviour of dry and low viscous infiltrated woven fabrics," *Composites Part A: Applied Science and Manufacturing*, vol. 124, no. 105466, 2019.

[126] A. Al-Hamdan, C. D. Rudd, and A. C. Long, "Dynamic core movements during liquid moulding of sandwich structures," *Composites Part A: Applied Science and Manufacturing*, vol. 29, no. 3, pp. 273–282, 1998.

[127] G. Hou, J. Wang, and A. Layton, "Numerical Methods for Fluid-Structure Interaction — A Review," *Communications in Computational Physics*, vol. 12, no. 2, pp. 337–377, 2012.

[128] H. Jasak and H. G. Weller, "Application of the finite volume method and unstructured meshes to linear elasticity," *International Journal for Numerical Methods in Engineering*, vol. 48, pp. 267–287, 2000.

[129] M. Schäfer, I. Teschauer, L. Kadinski, and M. Selder, "A numerical approach for the solution of coupled fluid–solid and thermal stress problems in crystal growth processes," *Computational Materials Science*, vol. 24, pp. 409–419, 2002.

[130] I. Bijelonja, I. Demirdžić, and S. Muzaferija, "A finite volume method for large strain analysis of incompressible hyperelastic materials," *International Journal for Numerical Methods in Engineering*, vol. 64, no. 12, pp. 1594–1609, 2005.

[131] D. Carolan, Ž. Tuković, N. Murphy, and A. Ivanković, "Arbitrary crack propagation in multi-phase materials using the finite volume method," *Computational Materials Science*, vol. 69, no. 3, pp. 153–159, 2013.

[132] P. Cardiff and I. Demirdžić, "Thirty Years of the Finite Volume Method for Solid Mechanics," *Archives of Computational Methods in Engineering*, vol. 28, pp. 3721—-3780, 2021.

[133] P. Cardiff, "Development of the Finite Volume Method for Hip Joint Stress Analysis," PhD Thesis, National University of Ireland, 2012.

[134] P. Cardiff and Ž. Tuković, "solids4foam," https://bitbucket.org/philip_cardiff/solids4foam-release/src/master/, 2021, accessed: 2021-07-26.

[135] P. Cardiff, A. Karač, and A. Ivanković, "Development of a finite volume contact solver based on the penalty method," *Computational Materials Science*, vol. 64, pp. 283–284, 2012.

[136] P. Cardiff, A. Karač, and A. Ivanković, "A large strain finite volume method for orthotropic bodies with general material orientations," *Computer Methods in Applied Mechanics and Engineering*, vol. 268, pp. 318–335, 2014.

[137] P. Cardiff, Ž. Tuković, P. D. Jaeger, M. Clancy, and A. Ivanković, "A Lagrangian cell-centred finite volume method for metal forming simulation," *International Journal for Numerical Methods in Engineering*, vol. 109, no. 13, pp. 1777–1803, 2017.

[138] T. Tang, O. Hededal, and P. Cardiff, "On finite volume method implementation of poro-elasto-plasticity soil model," *International Journal for Numerical and Analytical Methods in Geomechanics*, vol. 39, no. 13, pp. 1410–1430, 2015.

[139] K. Maneeratana, "Development of the finite volume method for non-linear structural applications," PhD Thesis, University of London, 2000.

[140] J. Seuffert, L. Kärger, and F. Henning, "Resin Transfer Molding (RTM) of fiber-reinforced polymer sandwich parts: mold filling simulations with fluid structure interaction," *ECCOMAS Coupled Problems*, 2021, online Conference.

[141] L. Trevino, K. Rupel, W. B. Young, M. J. Liou, and L. J. Lee, "Analysis of resin injection molding in molds with preplaced fiber mats. i: Permeability and compressibility measurements," *Polymer Composites*, vol. 12, no. 1, pp. 20–29, 1991.

[142] F. Robitaille and R. Gauvin, “Compaction of textile reinforcements for composites manufacturing. I: Review of experimental results,” *Polymer Composites*, vol. 19, no. 2, pp. 198–216, 1998.

[143] C. W. MacMinn, E. R. Dufresne, and J. S. Wettlaufer, “Large deformations of a soft porous material,” *Physical Review Applied*, vol. 5, no. 044020, 2016.

[144] H.-J. Bungartz, F. Lindner, B. Gatzhammer, M. Mehl, K. Scheufele, A. Shukaev, and B. Uekermann, “preCICE – A fully parallel library for multi-physics surface coupling,” *Computers & Fluids*, vol. 141, pp. 250–258, 2016.

[145] “preCICE schematic overview,” https://github.com/precice/precice.github.io/tree/master/material, 2021, accessed: 2021-10-26.

[146] J. Seuffert, L. Kärger, M. Chourdakis, B. Uekermann, and F. Henning, “Fluid structure interaction during the Resin Transfer Molding (RTM) manufacturing process for continuous fiber reinforced composites,” *International Conference on Computational Methods for Coupled Problems in Science and Engineering*, 2019, Sitges, Spain.

[147] G. Dhondt and K. Wittig, “CalculiX: A Free Software Three-Dimensional Structural Finite Element Program,” http://www.dhondt.de/index.html, 2021, accessed: 2021-07-01.

[148] “preCICE-CalculiX adapter,” https://precice.org/adapter-calculix-overview.html, 2021, accessed: 2021-10-25.

[149] J. Degroote, K.-J. Bathe, and J. Vierendeels, “Performance of a new partitioned procedure versus a monolithic procedure in fluid–structure interaction,” *Computers & Structures*, no. 87, pp. 793–801, 2009.

[150] U. Küttler and W. A. Wall, "Fixed-point fluid–structure interaction solvers with dynamic relaxation," *Computational Mechanics*, vol. 43, no. 1, pp. 61–72, 2008.

[151] C. Michler, H. van Brummelen, and R. de Borst, "An investigation of Interface-GMRES(R) for fluid–structure interaction problems with flutter and divergence," *Computational Mechanics*, vol. 47, no. 1, pp. 17–29, 2011.

[152] J. Degroote, R. Haelterman, S. Annerel, P. Bruggeman, and J. Vierendeels, "Performance of partitioned procedures in fluid–structure interaction," *Computers & Structures*, vol. 88, no. 7-8, pp. 446–457, 2010.

[153] D. Magagnato, B. Thoma, and F. Henning, "Experimental characterization to determine the influence of different binder systems on the preform permeability during RTM manufacturing," *Journal of Plastics Technology*, vol. 11, no. 4, pp. 256–270, 2015.

[154] R. Graupner and K. Drechsler, "Quantitative transversal permeability testing - challenges and enhancements," *International Conference on Flow Processes in Composite Materials (FPCM)*, 2018, Lulea, Sweden.

[155] A. Hammami and B. R. Gebart, "Analysis of the vacuum infusion molding process," *Polymer Composites*, vol. 21, no. 1, pp. 28–40, 2000.

[156] A. Dereims, "Industrial simulation of composite part manufacturing processes by resin infusion : interaction between fluid and low permeability porous solid undergoing large deformations," PhD Thesis, Ecole Nationale Superieure des Mines, Saint-Etienne, 2013.

[157] F. Robitaille and R. Gauvin, "Compaction of textile reinforcements for composites manufacturing. II: Compaction and relaxation of dry and H2O-saturated woven reinforcements," *Polymer Composites*, vol. 19, no. 5, pp. 543–557, 1998.

[158] S. Bickerton, M. J. Buntain, and A. A. Somashekar, "The viscoelastic compression behavior of liquid composite molding preforms," *Composites Part A: Applied Science and Manufacturing*, vol. 34, no. 5, pp. 431–444, 2003.

[159] S. Comas-Cardona, P. Le Grognec, C. Binetruy, and P. Krawczak, "Unidirectional compression of fibre reinforcements. Part 1: A non-linear elastic-plastic behaviour," *Composites Science and Technology*, vol. 67, no. 3-4, pp. 507–514, 2007.

[160] P. A. Kelly, "A viscoelastic model for the compaction of fibrous materials," *Journal of the Textile Institute*, vol. 102, no. 8, pp. 689–699, 2011.

[161] L. J. Gibson and M. F. Ashby, *Cellular Solids*. Cambridge, UK: Cambridge University Press, 2014.

[162] M. Mooney, "A Theory of Large Elastic Deformation," *Journal of Applied Physics*, vol. 11, no. 9, pp. 582–592, 1940.

[163] R. S. Rivlin, "Large Elastic Deformations of Isotropic Materials. I. Fundamental Concepts," *Philosophical Transactions of the Royal Society A: Mathematical, Physical and Engineering Sciences*, vol. 240, no. 822, pp. 459–490, 1948.

[164] R. W. Ogden, "Large Deformation Isotropic Elasticity - On the Correlation of Theory and Experiment for Incompressible Rubberlike Solids," *Proceedings of the Royal Society A: Mathematical, Physical and Engineering Sciences*, vol. 326, no. 1567, pp. 565–584, 1972.

[165] Zoltek, "ZOLTEK™ PX35 Uni-Directional Fabrics: Technical Datasheet," https://zoltek.com/wp-content/uploads/2017/09/TDS_PX35_Uni-Directional_Fabrics.pdf, 2021, accessed: 2021-07-18.

[166] J. Gerstenkorn, M. Kothmann, G. Deinzer, L. Kärger, and F. Henning, "Characterization of the multi-axial material behavior of polymer foams during the RTM process," *Proceedings of ECCM17- European Conference on Composite Materials*, 2016, Munich, Germany.

[167] Deutsches Institut für Normung, DIN EN ISO 844:2021, "Rigid cellular plastics – Determination of compression propertiesn," 2021.

[168] J. A. Rinde, "Poisson's ratio for rigid plastic foams," *Journal of Applied Polymer Science*, vol. 14, pp. 1913–1926, 1970.

[169] Z. Cai, "Analysis of Mold Filling in RTM Process," *Journal of Composite Materials*, vol. 26, no. 9, pp. 1310–1338, 1992.

Publications

Journal publications

- Magagnato, D.; Seuffert, J.; Bernath, A.; Kärger, L.; Henning, F. (2017): Experimental and numerical study of the influence of integrated load transmission elements on filling behavior in resin transfer molding, Composite Structures, 198, 135–143
- Seuffert, J.; Kärger, L.; Henning, F. (2018): Simulating Mold Filling in Compression Resin Transfer Molding (CRTM) Using a Three-Dimensional Finite-Volume Formulation, Journal of Composites Science, 2(2), 23
- Muth, M.; Schwennen, J.; Bernath, A.; Seuffert, J.; Weidenmann, K. .; Fleischer, J.; Henning, F. (2018): Numerical and experimental investigation of manufacturing and performance of metal inserts embedded in CFRP, Production engineering, 12 (2), 141–152
- Henning, F.; Kärger, L.; Dörr, D.; Schirmaier, F. J.; Seuffert, J.; Bernath, A. (2019): Fast processing and continuous simulation of automotive structural composite components, Composites-Science and Technology, 171, 261–279
- Seuffert, J.; Rosenberg, P.; Kärger, L.; Henning, F.; Kothmann, M. H. and Deinzer, G. (2020): Experimental and numerical investigations of pressure-controlled resin transfer molding (PCRTM), Advanced Manufacturing: Polymer and Composites Science, 6:3, 154-163
- Seuffert, J.; Bittrich, L.; Cardoso de Oliveira, L.; Spickenheuer, A.; Kärger, L. (2021): Micro-Scale Permeability Characterization of Carbon Fiber Composites Using Micrograph Volume Elements. Frontiers in Materials 8:745084

- Nieschlag, J.; Seuffert, J.; Strack, D.; Friedmann, M.; Kärger, L.; Henning, F.; Fleischer, J. (2021): Experimental and numerical analysis of mold filling in rotational molding, Journal of Composites Science, 5(11), 289

Conference contributions with proceedings

- Seuffert, J.; Kärger, L.; Henning, F. (2017): Simulation of the influence of embedded inserts on the RTM filling behavior considering local fiber structure, 21st Symposium on Composites, Key Engineering Materials, Vol. 742, 681-688
- Zimmerling, C.; Schindler, P.; Seuffert, J.; Kärger, L. (2021): Deep Neural Networks as Surrogate Models for Time-efficient Manufacturing Process Optimisation, Proceedings 24th International Conference on Material Forming (ESAFORM), Liège, Belgium

Conference contributions without proceedings

- Seuffert, J.; Rosenberg, P.; Kärger, L.; Henning, F.; Kothmann, M. H.; Deinzer, G. (2018): Mold Filling Simulation of a Pressure Controlled Resin Transfer Molding (PC-RTM) Process –Method and Application, The 14th international Conference on Flow Processing in Composite Materials (FPCM14), Lulea, Sweden
- Kärger, L.; Dörr, D.; Poppe, C.; Seuffert, J.; Bernath, A.; Galkin, S.; Zimmerling, C.; Henning, F. (2018): Continuous Process Simulation for Continuous Fiber Reinforced Composites, International VDI Conference, Amsterdam

- Seuffert, J.; Wittemann, F.; Henning, F. (2019): Prozesssimulationen mit OpenFOAM® – Großserienherstellung von faserverstärkten Kunststoffbauteilen, Kunststoffe+Simulation, München, Germany
- Seuffert, J.; Kärger, L.; Chourdakis, G.; Uekermann, B.; Henning, F. (2019): Fluid structure interaction during the Resin Transfer Molding (RTM) manufacturing process for continuous fiber reinforced composites, International Conference on Computational Methods for Coupled Problems in Science and Engineering, Sitges, Spain
- Krauss Constantin; Dörr, D.; Seuffert, J.; Bernath, A.; Galkin, S.; Kärger, L. (2019): Interface Challenges and Solution Approaches with Regard to the New VMAP Standard in a Continuous CAE-Chain for the Holistic Manufacturing Simulation of High Performance Composites, NAFEMS World Congress 2019, Quebec City, Canada
- Kärger, L.; Dörr, D.; Seuffert, J.; Bernath, A.; Krauss, C.; Henning, F. (2019): Continuous process simulation of automotive structural composite components, EUROMECH Colloquium 602 – Composite manufacturing processes. Analyses, modelling and simulations, Lyon, France
- Seuffert, J.; Kärger, L.; Henning, F. (2021): Resin Transfer Molding (RTM) of fiber-reinforced polymer sandwich parts: mold filling simulations with fluid structure interaction, International Conference on Computational Methods for Coupled Problems in Science and Engineering, online